Analysis of a Microwave Patch Antenna Array for Reflection Measurements

Febin Paul Nottath

A thesis submitted to
Auckland University of Technology
in fulfilment of the requirements for the degree of

Master of Engineering (ME)

November 2014

School of Engineering

Attestation of Authorship

"I hereby declare that this submission is my own work and that, to the best of my knowledge and belief, it contains no material previously published or written by another person (except where explicitly defined in the acknowledgements), nor material which to a substantial extent has been submitted for the award of any other degree or diploma of a university or other institution of higher learning."

Febin Paul Nottath

November 2014

Acknowledgement

I owe gratitude to all those people who helped me to complete this research. There were many people who came in and out during my research journey.

My deepest gratitude is to my primary supervisor Dr. John Collins for his guidance, knowledge and his precious time that he shared with me. Every time when I knock on his door, even without appointments, he always waved his hand "come on in" with a sincere smile on his face. His patience and support I cannot forget which helped me to overcome many crisis situations in completing this research.

I also want to thank my secondary supervisor Dr. Mark Beckerleg for his support and also Prof. Ahmed Al-Jumaily, Prof. Zhan Chen and Dr. Shane Pinder for their support.

I want to thank Thomas Benke of Leap Australia for his technical support for HFSS and the technicians at AUT, School of Engineering for assistance with my research experiments.

My friends helped me to stay calm throughout these years, their care and support has been tremendous.

My parents and my family, without their unconditional love, support, prayers and infinite patience this thesis would not have reached a completion. I thank God almighty for giving me courage, hope and guiding me through this amazing journey.

Abstract

Microstrip antennas and arrays are widely used antenna technology in the frequency range of 1 GHz to 100 GHz. Microstrip antennas are simple and compact, and with current printed circuit technologies they are easy to manufacture. They are used in various applications such as; satellite communications, biomedical, mobile phone technology, radar, wireless local area networks and many other applications. This research focuses on developing a microstrip antenna to be used in an array that operates in a dual-band frequency range. The long term aim of this research is to develop an antenna array which can be used for the application of breast cancer detection.

Two dual-band antenna elements are developed for this research and the antenna elements are arranged in a 2×2 array. Each antenna array has been designed and manufactured on a Rogers 4003 substrate. The design of the antenna elements were such that it operated in the frequency range of 5 GHz to 7 GHz creating an effect of wideband frequency operation. Four resonant frequencies were used in the range 5-7 GHz.

The antenna elements were designed and simulated using the ANSYS HFSS software platform. Five antenna arrays were tested experimentally. The initial work is to study the reflections from an object and the phase information of the reflection is analysed. A simulation model of the reflection analysis is conducted and a metal object is used for this purpose to get better understanding of the behaviour of antenna elements in an array and how effectively the phase information can be extracted to find the reflecting body's nature. The antenna elements built and tested match the simulation results well.

The phase of transmitted signals has been measured experimentally and the results obtained were similar to the simulations and theory. The electric field information from the simulation has also been studied. This analysis provides a better understanding of

how the reflected signals are received at the receiver antenna and it is expected that in future this method of analysis can be implemented for complex object identification.

Table of Contents

List of Figures

List of Tables

List of Abbreviations

Abbreviations	Meaning
BCD	Breast Cancer Detection
BW	Band-Width
CAD	Computer-aided Design
CMI	Confocal Microwave Imaging
CP	Circular Polarisation
dB	Decibel
E-field	Electric Field
FDTD	Finite-Difference-Time-Domain
FEM	Finite Element Modelling
F-SMA	Female SubMiniature Version A
GHz	Giga Hertz
GPS	Global Positioning System
GSM	Global System for Mobile
HFSS	High Frequency Structural Simulator
ISM	Industrial, Scientific and Medical
LSM	Least Square Method
MHz	Mega Hertz
MI	Microwave Imaging
NA	Network Analyser
OUI	Object Under Investigation
PCB	Printed Circuit Board

PML	Perfectly Matched Layer
Q-factor	Quality Factor
RF	Radio Frequency
RFID	Radio-Frequency Identification
RL	Return Loss
RLC	Resistor, Inductor, Capacitor
SLOT	Short, Load, Open, Through
S-parameter	Scattering Parameter
SWR	Standing Wave Ratio
TM	Transverse Magnetic
UWB	Ultra-Wide Band
VSWR	Voltage Standing Wave Ratio
WLAN	Wireless Local Area Network

Chapter 1 Introduction

Antennas in various forms have found application in biomedical imaging [1-3] and with research developments in alternative imaging techniques for breast cancer detection there has been a focus on developing new antenna elements for the purpose [4-6]. Microwave imaging has been suggested as an alternative imaging tool. One of the major components at the front end is the antenna elements which are used to transmit and receive the signals. The frequency range used for microwave imaging for imaging the human breast is in between 0.5 GHz and 10 GHz. For this research microstrip patch antennas have been chosen because they are easy to manufacture with printed circuit board technology, inexpensive and can be easily made to operate in arrays.

At present the widely used tool for breast cancer screening is X-ray mammography. The major drawback with X-ray is the radiation and therefore researchers have been examining for alternative techniques. Microwave imaging is based on the dielectric properties of the body tissues, particularly conductivity and permittivity. This research examines an alternative technique for breast cancer detection based on a two-dimensional antenna array which can be used as sensors for wide-band microwave holography.

Microwave holography techniques are widely used for surveillance systems, antenna measurements, and have been recently introduced for medical imaging [7-11]. Unlike holography methods involving a single transmitter and receiver configuration this research focuses on developing numerous transmitters and receivers in an array to scan the entire object. The reflected signals are analysed to locate the tumor. Antenna elements used for transmitting and receiving signals maybe operated at a single frequency or some may use a wideband frequency range.

The proposed antenna array design uses a low power continuous microwave signal and it can cover a wide-band frequency range (5-7 GHz) by resonating at four resonant frequencies. Two dual-band antenna elements are used. This research work is based on 2×2 antenna array, covering four frequencies using two pairs of dual-band antennas. In this research the main focus is to develop a new antenna suitable for a large array. One of the advantages of using this design is that it operates in dual frequencies and it covers four resonance frequencies in the frequency bandwidth of 5-7 GHz. Also the antenna element and array design process is simple and easy to implement compared to design methods followed in [6, 12, 13].

The analysis is based on the phase of the signal rather than the amplitude. The amplitude of the signal fades easily whereas phase embedded in the signal remains consistent with the distance travelled. From the reflected signal the phase angle is extracted and analysed. Using a simulation tool the antenna elements and array have been designed and the reflection analysis is simulated using simulation software. Experimental validation is conducted on a small antenna array, as well as the reflection measurements to find out how effectively the phase information can be extracted. This is done by using a metal plate as an object at various distances. The aim is to find how effectively signals from the dual-band antenna array are capable of maintaining the phase relation in the measurements. This research helps to identify and improve the design and gives greater insight on phase analysis for reflection measurements.

The thesis is organised as follows, Chapter 2 covers the background theory on microstrip patch antennas. It covers the model used to analysis a rectangular microstrip antenna. CAD formulas for rectangular patch antennas are discussed along with important characteristics of a microstrip antenna.

In Chapter 3 literature review on various microwave imaging techniques used for breast cancer detection is covered. Chapter 4 deals with the design of the antenna and antenna array using a simulation tool. Chapter 5 covers the experimental validation of the major design parameters of the microstrip antenna.

In Chapter 6 the simulated reflection results are described. The analysis of magnitude and phase is covered in this chapter. The simulation results are shown in this. Chapter 7 describes the setup for experimental reflection measurements and the magnitude and phase results of these experiments.

Chapter 8 covers the theory developed based on the experimental data and LSM is used to find the fit for the data. This chapter also covers the how results from the experiment are used to find the received E-fields at the receiver. In Chapter 9 the conclusion and future works are summarised. Requirement for increased antenna array and increased data points at the receiving antenna edge and a robust measurement setup to conduct the experiment were suggested.

Chapter 2 Background

2.1 Microstrip Antennas

Microstrip antennas are low profile antennas which have been used for many applications in the frequency range of 1 GHz up to 100 GHz. The first of its kind was introduced in 1972 by Howell [14] and Munson [15]. Microstrip antenna (also known as patch antennas) are attractive because they are lightweight, inexpensive, mechanically robust, and easy to manufacture using printed circuit board (PCB) technology. They can be easily integrated to electronic circuits, can be used to form arrays and desired antenna characteristics can be achieved with the existing technology.

Microstrip antennas find wide use in commercial applications such as mobile phones, GPS receivers, aircraft, biomedical devices, wireless networks and radio frequency identification. They are also used in satellite, spacecraft, radar and military applications, where cost, size and ease of manufacturing are constraints.

There are some disadvantages with microstrip antennas. One of the problems associated with these antennas is their low bandwidth. However this drawback can be overcome with the development of new technologies. There are various methods available now to increase the bandwidth. Bandwidth enhancement using tuning stubs [16], inserting parasitic metallic strips [17] and using slots [18] are some of the techniques.

Microstrip antennas are usually rectangular, circular, triangular, square or dipole in shape. Rectangular and circular patch antennas are the most common. This research focuses on the design and development of a near square patch element suitable for a microstrip antenna array. The purpose of this antenna array is for breast cancer detection. This design will be able to transmit and receive signals in the same antenna array. Ultimately this array aims to find out the characteristics of the object from which the transmitted signals are reflected.

2.2 Radiation Mechanism of Microstrip Antenna

A microstrip antenna can be considered as a dielectric-loaded cavity. The electric fields inside the antenna substrate can be found by modelling top and bottom regions of the patch as a cavity bounded by electric walls and magnetic walls along the perimeter of the patch. The cavity model analysis has been well established by Y. T. Lo et al. [19] and has been advanced by [20]-[21]. The following description for cavity model analysis is based on [19] [22, 23].
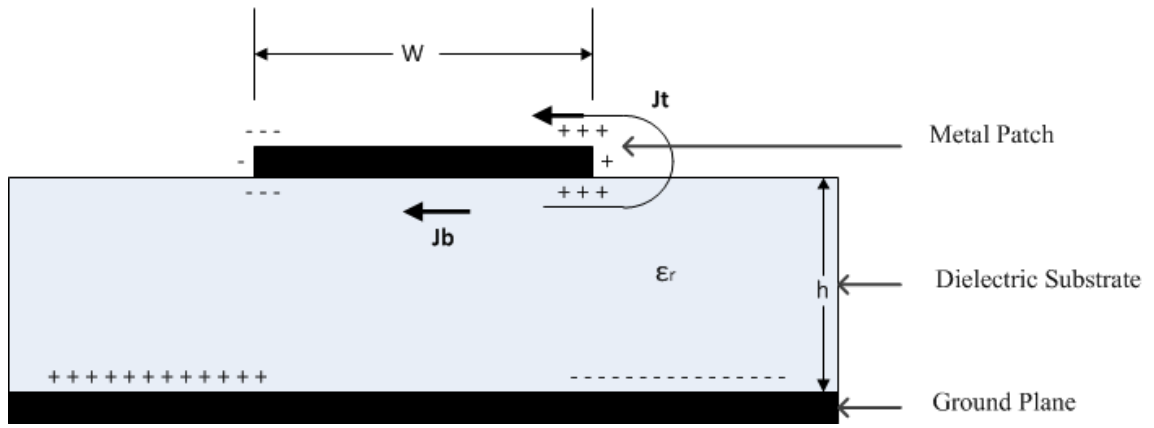
Figure 2-1 Charge distribution and current density on a microstrip antenna [23]

Consider a patch antenna as shown in Figure 2.1. When the microstrip patch antenna is fed with a microwave source, a charge distribution occurs on the upper and lower surface of the patch as well as the ground plane at the bottom. The charges on the ground plane and bottom surface of the patch are opposite polarity and attract, causing a charge concentration on the bottom of the patch element. Meanwhile repulsive forces exist between like charges on the bottom surface of the patch, which force some charges from the bottom of the patch around its edge onto the top of the patch. This causes a movement of charge which produces current densities $\overrightarrow{J_b}$ and $\overrightarrow{J_t}$, the subscript b denotes for the bottom and t for the top of the patch. For most microstrip patch antennas, the height-width ratio is very small so the attractive force between the charges on the patch and the substrate dominates and most of the charge concentration and current flow

5

remains underneath the patch. There is a flow of current around the edges of the patch to the top surface but it is small and it decreases as height-weight ratio decreases. This causes a weak magnetic field component tangential to the edges. Because of this an approximation is made to simplify the analysis of the cavity. The tangential magnetic field is considered zero and these are assumed to be perfect magnetic walls around the periphery of the patch. Usually the substrate used for microstrip antenna design is very thin compared to the signal wavelength in the dielectric. Therefore the electric and magnetic field inside the substrate can be taken as constant along the height of the substrate and the electric field is assumed to be normal to the patch surface. So a microstrip patch antenna can be modelled as a cavity with electric walls at the top and bottom of the patch and four magnetic walls along the edge of the patch antenna. The only mode that is possible in this cavity is the *TM* mode. *TM* corresponds to Transverse Magnetic (TM) for which the electric field $E_z \neq 0$ and magnetic field $H_z = 0$ [24].
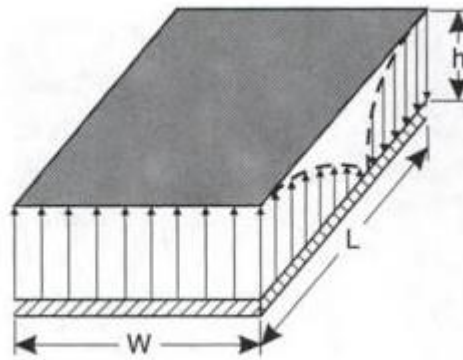
Figure 2-2 Electric field distribution for TM100 mode in the microstrip cavity [23]

For a rectangular patch as shown in Figure 2.2, the radiation takes place through the four sidewalls of the cavity. These sidewalls represent four slots and the equivalent electric and magnetic current densities in the slots are $\vec{J_s}$ and $\vec{M_s}$. The electric and magnetic fields $\vec{E_a}$ and $\vec{H_a}$ are shown in Figure 2.3(a).

$$\vec{J_b} = \hat{n} \times \vec{H_a} \qquad\qquad\qquad 2.1$$

$$\vec{M_s} = -\hat{n} \times \vec{E_a} \qquad\qquad\qquad 2.2$$
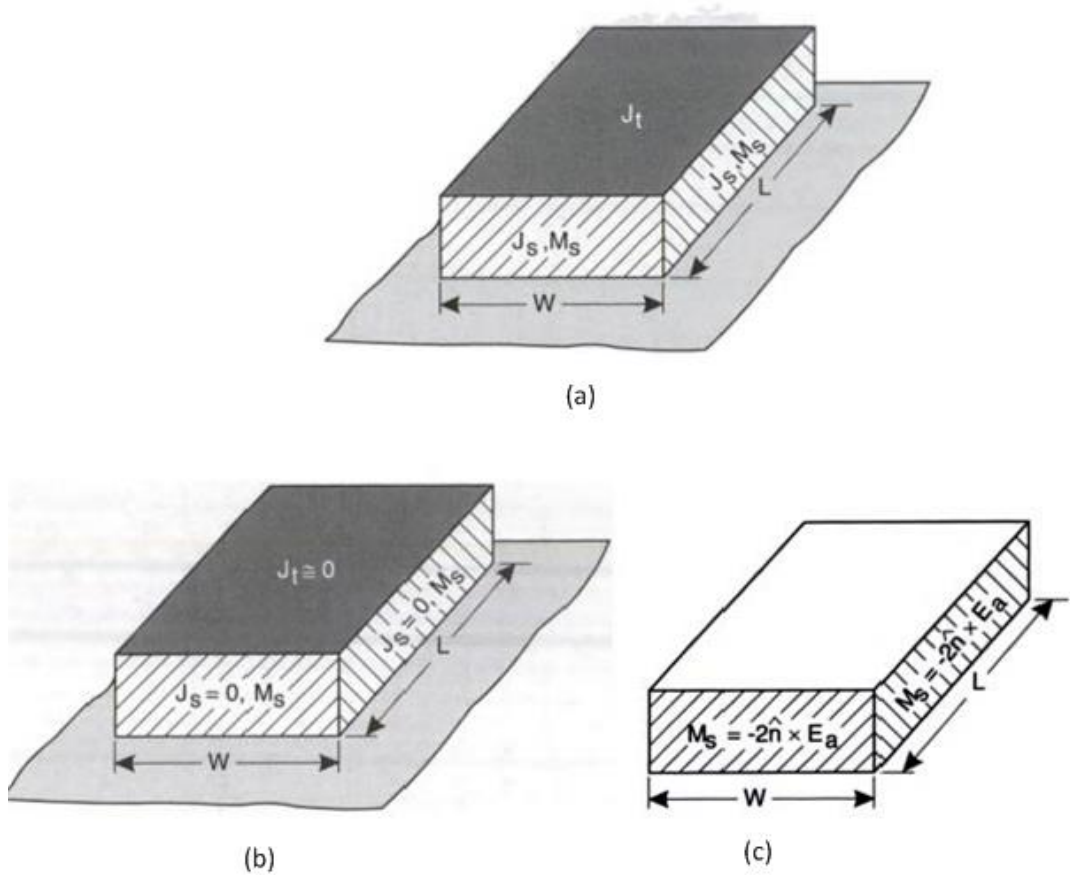
Figure 2-3 Equivalent current densities on a rectangular microstrip patch. (a) Js and Ms with ground plane (b) Js = 0, Ms with ground plane, and (c) Ms with no ground plane [23]

The patch current density at the top $\vec{J_t}$ is very small compared to the current at the bottom $\vec{J_b}$ for thin dielectric substrate. Therefore $\vec{J_t}$ can be set to zero, and the tangential magnetic fields along the patch edges and the corresponding current density $\vec{J_s}$ are also set to zero. The only nonzero magnetic current density is along the periphery of the patch, $\vec{M_s}$, as shown in Figure 2.3(b). By taking into account the presence of the ground plane at the bottom, and based on image theory, the equivalent current density will be

doubled. Therefore four ribbons of magnetic current around the periphery can cause radiation from a patch. Free space radiation of the same is shown in Figure 2.3(c).

$$\overrightarrow{M_s} = -2\hat{n} \times \overrightarrow{E_a} \qquad\qquad 2.3$$

Therefore, for the dominant mode of length W and height h the slot electric field $\overrightarrow{E_a}$ is given by

$$\overrightarrow{E_a} = \hat{z} \times E_o \qquad\qquad 2.4$$

for the other two slots of length L and height h

$$\overrightarrow{E_a} = -\hat{z} \times E_o \sin(\pi x/L) \qquad\qquad 2.5$$

Based on the equivalent principle, each slot in the patch radiates the same field as a magnetic dipole with current density $\overrightarrow{M_s}$. Figure 2.4 shows the equivalent magnetic current densities in the slots. Along the x axis, the radiation produced by the current densities are equal and opposite and they tend to cancel out. But the current densities along the y axis are of the same magnitude and phase and are separated by the length L of the patch. Therefore, radiation for the rectangular patch occurs primarily through two vertical slots.

(a)

(b)
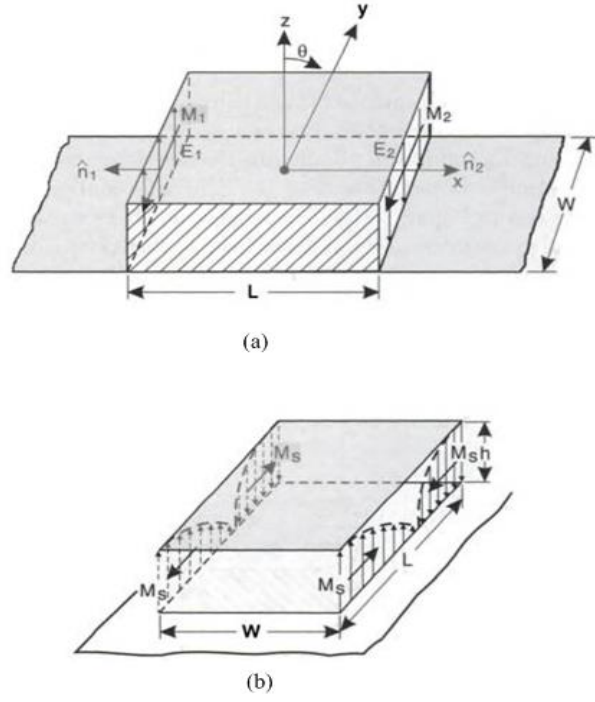
Figure 2-4 Rectangular microstrip patch with magnetic current density distribution for the TM10 mode on radiating slots. (a) Current distribution on radiating slots (b) Current distribution on non-radiating slots [23]
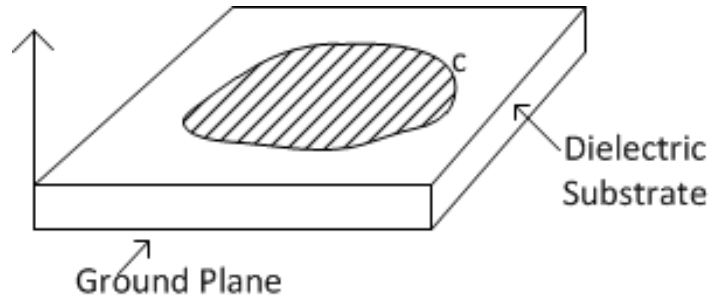
Figure 2-5 Microstrip antenna without feed point [19]

2.3 Cavity Model Analysis

The cavity model analysis presented below is based on Lo et al [19] and Garg. R et al [22]. The analysis is based on the solution of the wave equation, derived from Maxwell's equations [25]:

$$\nabla \times \mathcal{E} = \frac{-\partial \mathcal{B}}{\partial t} \qquad \nabla . \mathcal{B} = 0$$

$$\nabla \times \mathcal{H} = \frac{-\partial \mathcal{D}}{\partial t} + \mathcal{J} \qquad \nabla . \mathcal{D} = q_v$$

2.6

where,

$\mathcal{E}$, is the electric intensity, unit is volt/meter

$\mathcal{H}$, is the magnetic intensity, unit is amperes/meter

$\mathcal{D}$, is the electric flux density, unit is coulombs/square meter

$\mathcal{B}$, is the magnetic flux density, unit is webers/ square meter

$\mathcal{J}$, is the electric current density, unit is amperes / square meter

q_v, is the electric charge density, unit is coulombs/cubic meter

When the field exists in a medium, the characteristics of the medium are considered and $\mathcal{D}$, $\mathcal{B}$ and $\mathcal{J}$ can be expressed as:

$$\mathcal{D} = \varepsilon\mathcal{E}$$
$$\mathcal{B} = \mu\mathcal{H}$$
$$\mathcal{J} = \sigma\mathcal{E}$$

2.7

where, ε is called the relative permittivity of the medium, μ is called the relative permeability of the medium and σ is the conductivity of the medium.

Maxwell's equations for sine wave signals can be written in complex form as:

$$\nabla \times E = -j\omega B \qquad\qquad \nabla.B = 0$$
$$\nabla \times H = -j\omega D + J \qquad\qquad \nabla.D = Q_v$$

2.8

The wave equation can be obtained by solving the above equation. The wave equation is:

$$\nabla \times \nabla \times E - k^2 E = -j\omega\mu_0 J \qquad\qquad 2.9$$

where $k^2 = \omega^2 \mu_0 \varepsilon_0 \varepsilon_r$.

A microstrip antenna without feed point is shown in Figure 2.5. The assumptions for cavity model analysis for thin substrates $(h \ll \lambda)$ are:

1) Since the substrate is very thin, in the region bounded by the antenna element and the ground plane, the electric field E has only a z-component and the magnetic field H has only x y-components.

2) The fields inside the cavity are independent of z, so for all frequencies $\partial/\partial z \equiv 0$

3) The electric current on the microstrip patch does not have any component normal to the edge of patch metallization. Therefore there are negligible tangential magnetic components along the edge $\partial E_z/\partial n = 0$.

Consider the region of the antenna between the patch metallization and ground plane as in Figure 2.5. Since the height of the substrate $h \ll \lambda$ is thin, the electric field distribution can be described by *TM* to z modes with $\partial/\partial z \equiv 0$.

If an excitation current density J_z is fed to a rectangular microstrip patch, the wave equation for $\bar{E}$ in the cavity in the z direction is:

$$\nabla \times \nabla \times \bar{E} - k^2\bar{E} = -j\omega\mu_0\vec{J} \qquad 2.10$$

or

$$\frac{\partial^2 E_z}{\partial x^2} + \frac{\partial^2 E_z}{\partial y^2} + k^2 E_z = j\omega\mu_0 J \qquad 2.11$$

where k is the wave number, $k^2 = \omega^2\mu_0\varepsilon_0\epsilon_r$.

The electric field inside the patch cavity in terms of various modes can be expressed as:

$$E_z(x,y) = \sum_m \sum_n A_{mn}\psi_{mn}(x,y) \qquad 2.12$$

where A_{mn} is the amplitude coefficient corresponding to the electric field mode vectors or eigenfunctions ψ_{mn}. The eigenfunctions ψ_{mn} are solutions of the homogenous wave equation, (2.14) with boundary conditions (2.13), and normalization conditions (2.15). The electric field for a rectangular patch of length L and W is discussed below.

$$\left.\frac{\partial\psi_{mn}}{\partial x}\right|_{x=0} = 0 = \left.\frac{\partial\psi_{mn}}{\partial x}\right|_{x=L} \qquad 2.13$$

$$\left.\frac{\partial \psi_{mn}}{\partial y}\right|_{y=0} = 0 = \left.\frac{\partial \psi_{mn}}{\partial y}\right|_{y=W}$$

$$\left(\frac{\partial^2}{\partial x^2} + \frac{\partial^2}{\partial y^2} + k^2_{mn}\right)\psi_{mn} = 0 \qquad\qquad 2.14$$

$$\int_x\int_y \psi_{mn}\psi_{mn}{}^* \, dx \, dy = 1 \qquad\qquad 2.15$$

The solutions (2.13) to (2.15) are the orthonormalized eigenfunctions

$$\psi_{mn}(x,y) = \sqrt{\frac{\in_m\in_n}{LW}}\cos(k_m x)\cos(k_n y) \qquad\qquad 2.16$$

$$m, n = 0,1,2, p, \ldots..$$

with

$$\in_p = \begin{cases} 1 \ for \ p = 0 \\ 2 \ for \ p \neq 0 \end{cases}$$

$$k_m = m\pi/L \ , k_n = n\pi/W \ , k^2_{mn} = k^2_m + k^2_n \qquad\qquad 2.17$$

The coefficient A_{mn} can be determined by multiplying $\in_x$ by ψ^*_{mn} and integrating over the area of the patch element. The amplitude coefficient A_{mn} is given by,

$$A_{mn} = \frac{j\omega\mu_0}{k^2 - k^2_{mn}}\iint_{feed}\psi^*_{mn}J_z \, dx \, dy \qquad\qquad 2.18$$

Consider the excitation for the rectangular patch antenna with a coaxial feed. The current source has a cross-sectional area $D_x D_y$ equal to the cross-sectional area of the probe centered at $(x_0 y_0)$:

$$J_z = \begin{cases} I_0/D_x D_y \ for \ x_0 - D_x/2 \leq x \leq x_0 + D_x/2 \ and \ , \\ \qquad\quad y_0 - D_y/2 \leq y \leq y_0 + D_y/2 \\ 0 \qquad\qquad\qquad elsewhere \end{cases} \qquad 2.19$$

The coefficient A_{mn} can be found using (2.19) and (2.12)

$$A_{mn} = \frac{1}{D_x D_y} \frac{j\omega\mu_0}{k^2 - k_{mn}^2} \iint_{feed} I_0 \psi_{mn}^* \, dx$$

$$= \frac{j\omega\mu_0 I_0}{k^2 - k_{mn}^2} \sqrt{\frac{\epsilon_m \epsilon_n}{LW}} \cos(k_m x_0) \cos(k_n y_0) \, G_{mn}$$

2.20

where

$$G_{mn} = \sin c \, (n\pi D_x/(2L)) \sin c \, (m\pi D_y/(2W))$$

2.21

If the patch antenna is fed using a microstrip line along the edge of the patch then $D_x = 0$ and D_y equals to the effective width of the feed line. Then the electric field in the substrate of a rectangular patch can be found by substituting (2.15) in (2.7):

$$E_z(x,y) = \omega\mu_0 I_0 \sum_m^\infty \sum_n^\infty \frac{\psi_{mn}(x,y)\psi_{mn}(x_0,y_0)}{k^2 - k_{mn}^2} G_{mn}$$

2.22

The cavity model approach can be applied to various patch shapes [19, 20, 26-28] but the eigenfunctions depend on the patch shape and the size of the patch metallization.

2.4 Rectangular Microstrip Antennas

Microstrip antennas are also called patch antennas. The radiating patch element is made of conducting material such as copper on top of a dielectric substrate with a ground plane on the bottom side of the substrate. The power transmitted to the patch is either via coaxial cable or using a microstrip line. The cross section of a rectangular patch with a coaxial feed is shown in Figure 2.6. This research focuses on near square patch antennas, and further description of antenna design will be based on the rectangular patch antenna.
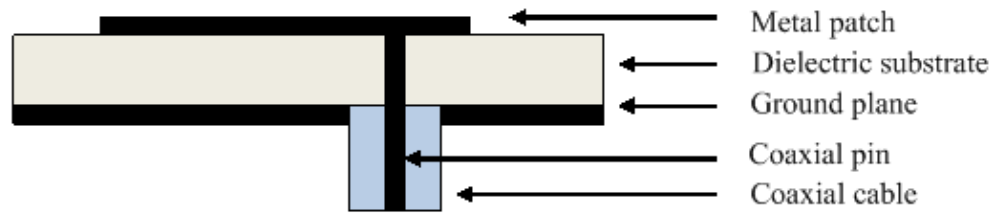
Figure 2-6 Cross section of rectangular patch

The patch and the ground plane are separated by a substrate of height 'h' and the dielectric constant is usually in the range of $2.2 \leq \varepsilon_r \leq 12$. For better efficiency and bandwidth, thick substrates with a low dielectric constant are preferred, but the size of the element increases. A thin substrate, with a higher dielectric constant, reduces undesired signals and coupling, resulting in greater loss, less efficiency and smaller bandwidth [23].

A patch antenna element of length L and width W positioned on top of a dielectric substrate of height h with a ground plane on the bottom is as shown in Figure 2.7. The radiation mechanism of this microstrip antenna has already been discussed in Chapter 2.2.
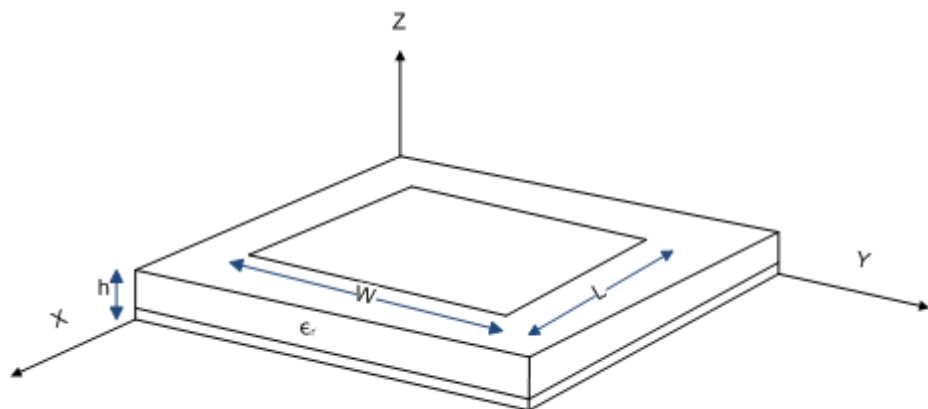
Figure 2-7 Rectangular patch antenna with Cartesian coordinate system

14

There are three popular models used to analyse microstrip antennas: transmission-line, cavity, and full wave analysis. The cavity model analysis has been used for this antenna model development and it has been discussed in Chapter 2.3. The cavity model is more accurate than the transmission line model and easier to use than the full-wave model

2.5 Antenna Parameters

The characteristics of an antenna are determined by various parameters that are associated with it. The following section will provide a brief overview of some of the important parameters. These parameters are mainly considered in the design of antennas.

2.5.1 Radiation Pattern

The radiation pattern is defined as a "mathematical function or a graphical representation of the radiation properties of antenna as a function of space coordinates. In most cases, the radiation pattern is determined in the far-field region and is represented as a function of the directional coordinates. Radiation properties include power flux density, radiation intensity, field strength, directivity, phase or polarisation" [23].

The radiation field can be represented in a spherical coordinate system, Figure 2.8(a). The angle θ is measured from the Z-axis and the angle $\emptyset$ measured counter clockwise from the X-axis [29]. The radiation pattern is usually represented by a three dimensional (3D) graph as shown in Figure 2.8(b), which shows the radiation pattern of a patch antenna.
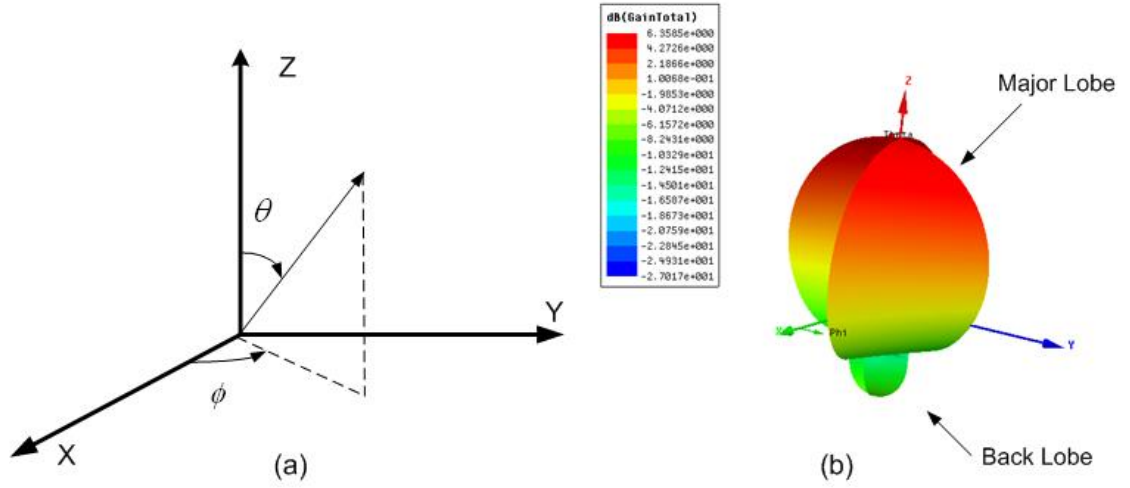
Figure 2-8 (a), Spherical coordinates [29] (b) 3D Radiation Pattern.

The radiation pattern contains radiation lobes, which is a "portion of the radiation pattern bounded by regions of relatively weak radiation intensity" [23]. The major lobe or main beam is the radiation lobe containing the direction of maximum radiation. In the Figure 3.3(b) the major lobe is pointing in the $\theta = 0$ direction. The back lobe is the radiation lobe whose direction θ is 180° away from the direction θ of the main beam of an antenna.

For a rectangular microstrip antenna, as shown in Figure 2.7, when the antenna element radiates, the radiated field is mainly produced by the TM_{10} and TM_{01} modes. The radiated field from the sides W for the dominant TM mode TM_{10} is given by [24]

$$E(\theta, \emptyset) = -jk \frac{e^{-jkr}}{4\pi r} 4E_o hW[\hat{\emptyset} \cos\theta \sin\emptyset - \hat{\theta} \cos\emptyset] F(\theta, \emptyset) \qquad 2.23$$

and similarly for the contribution by sides L with TM_{01} is:

$$E(\theta, \emptyset) = jk \frac{e^{-jkr}}{4\pi r} 4E_o hL[\hat{\emptyset} \cos\theta \cos\emptyset + \hat{\theta} \sin\emptyset] f(\theta, \emptyset) \qquad 2.24$$

where $F(\theta, \emptyset)$ and $f(\theta, \emptyset)$ can be obtained mathematically [24].

16

2.5.2 Input Impedance

In an antenna system, the transmission signal travels from the signal source through the transmission line to the antenna and then to free space. During this process the signal encounters impedance changes at each interface causing the signal to be reflected back towards the source. The reflected signal to the source forms a standing wave in the feed line and the ratio of maximum power transfer to minimum power in the wave can be measured which is referred to as the Standing Wave Ration (SWR). The ideal value is 1:1. For low power applications a value of 1.5:1 is typically acceptable.

The input impedance of the antenna is the ratio between the voltage and current at the antenna port. The input impedance is complex and a function of frequency (f); $Z_{in}(f) = R_{in}(f) + jX_{in}(f)$. The circuit representation of the antenna along with the lumped elements is as shown in Figure 2.9 [29].
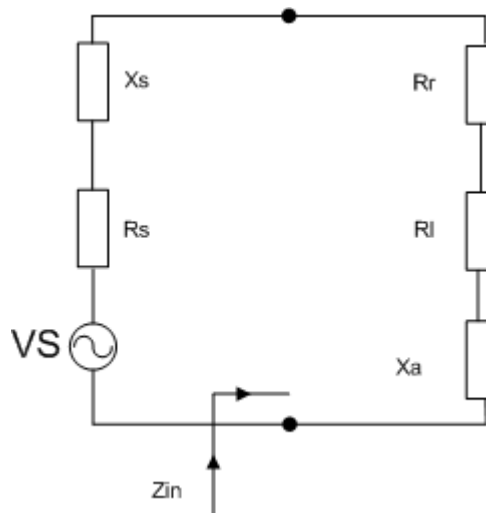
Figure 2-9 Equivalent circuit of an antenna

The antenna is connected to a source *VS*, with internal impedance $Z_s = R_s + jX_s$. The input impedance of antenna is, $Z_{in} = R_a + jX_a$. The real part of R_a consists of radiation resistance (R_r) and the antenna losses(R_l). The input impedance can be used to determine the reflection coefficient (Γ), voltage Standing Wave Ratio (*VSWR*) and return loss (*RL*).

17

$$\Gamma = \frac{Z_{in} - Z_o}{Z_{in} + Z_o} \qquad\qquad 2.25$$

where Z_o is the normalizing impedance of the port. The VSWR is given as

$$VSWR = \frac{1 + |\Gamma|}{1 - |\Gamma|} \qquad\qquad 2.26$$

And return loss is defined as

$$RL = -20log|\Gamma| \qquad\qquad 2.27$$

2.5.3 Antenna Efficiency

Antenna efficiency is defined as ratio of the power radiated to the input power of the antenna. The total efficiency of an antenna e_0 is affected by impedance mismatch and losses such as conduction and dielectric losses. The other efficiencies associated with an antenna are reflection efficiency, conduction efficiency and dielectric efficiency denoted as e_r, e_c and e_d respectively [23].

Conduction and dielectric efficiencies are difficult to calculate. Because it is hard to separate them, they are denoted as e_{cd}, antenna radiation efficiency.

Therefore

$$e_0 = e_r e_{cd} = e_{cd}(1 - |\Gamma|^2) \qquad\qquad 2.28$$

2.5.4 Directivity

The directivity of an antenna is defined as the "ratio of radiation intensity in a given direction from the antenna to the radiation intensity averaged over all directions" [23]. The average radiation intensity is equal to the total power radiated by the antenna divided by 4π. If the direction is not specified, the direction of maximum radiation

intensity is implied [23]. It is a measure of how directional an antenna's radiation pattern is. The mathematical form is

$$D = \frac{U}{U_o} = \frac{4\pi U}{P_{rad}}$$
2.29

Where:

D = Directivity

U = radiation intensity (W/unit solid angle)

U_0 = Radiation intensity of isotropic source (W/unit solid angle)

P_{rad} = Total radiated power (W)

The directivity for a patch antenna can be calculated using the equation [23]

$$D_1 = \frac{2}{15G_{rad}} \left(\frac{W}{\lambda_o}\right)^2$$
2.30

where W is the width of the patch, G_{rad} is the radiation conductance and λ_o is the wavelength. The directivity of a microstrip patch antenna can be approximated to 8.2 dB for $W \ll \lambda_0$ [23].

2.5.5 Gain

Antenna gain is closely related to its directivity. The gain of an antenna is defined by Balanis [23] as "the ratio of the intensity, in a given direction, to the radiation intensity that would be obtained if the power accepted by the antenna were radiated isotropically. The radiation intensity corresponding to the isotropically radiated power is equal to the power accepted (input) by the antenna divided by 4π." It is expressed as:

$$Gain = 4\pi \frac{radiation\ intensity}{total\ input(accepted)\ power} = 4\pi \frac{U(\theta, \phi)}{P_{in}}$$
2.31

where $U(\theta, \phi)$ is the radiation intensity in a given direction (θ, ϕ) and P_{in} is the total input power.

2.5.6 Polarisation

The polarisation of an antenna [23] is defined as the "property of an electromagnetic wave describing the time varying direction and relative magnitude of the electric-field vector; specifically, the figure traced as a function of time by the extremity of the vector at a fixed location in space, and the sense in which it is traced, as observed along the direction of propagation." Polarisation then is the curve traced by the end point of the arrow representing the instantaneous electric field. The field must be observed along the direction of propagation [30]. Figure shows a typical trace as a function of time.
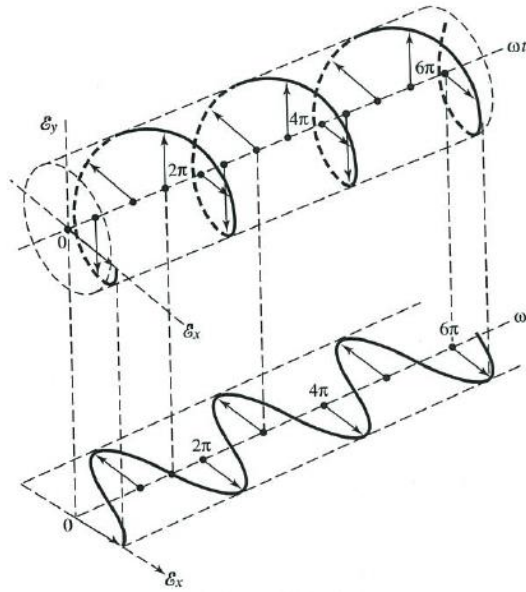
Figure 2-10 Rotation of wave [23]

There are three types of polarisation: linear, circular and elliptical polarisation. The definition of these three polarisations according to [23] is described below.

Linear polarisation: A time-harmonic wave is linearly polarised at a given point in space if the electric-field (or magnetic-field) vector at that point is always oriented along the same straight line at every instant of time. This is accomplished if the electric

or magnetic vector possess only one component or two orthogonal linear component that are in time phase or 180° out-of-phase.

Circular polarisation (CP): A time-harmonic wave is circularly polarised at a given point in space if the electric-field (or magnetic-field) vector at that point traces a circle as a function of time. The electric or magnetic vector fields must have two orthogonal linear components. The two components must have equal amplitude and must have a time-phase difference of odd multiples of 90°. The rotation of field can be right-hand or left-hand circular polarisation from the observer point of view.

Elliptical polarisation: A time-harmonic wave is elliptically polarised if the tip of the field vector traces an elliptical locus in space. For an elliptically polarised wave, the field must have two orthogonal linear components either the same or different amplitude. If the two field components are of different amplitude, the phase difference between them must not be 0° or multiples of 180°. If the fields are of same magnitude, the phase difference between the components must not be odd multiples of 90°.

2.6 Scattering Parameter

Scattering parameters or S-parameters are very useful to work with in electrical networks at microwave frequencies. In an N-port network, S-parameters relate a voltage wave incident on the ports to those reflected from the ports. Network analysis techniques can be used to calculate S parameters or they can be measured using a vector network analyser. Consider an N port network [31] as shown in Figure 2.11. On the nth port a terminal plane is defined by t_n along with equivalent voltages and currents for the incident (V_n^+, I_n^+) and reflected (V_n^-, I_n^-) waves. The scattering matrix or [S] matrix is defined based on incident and reflected waves,
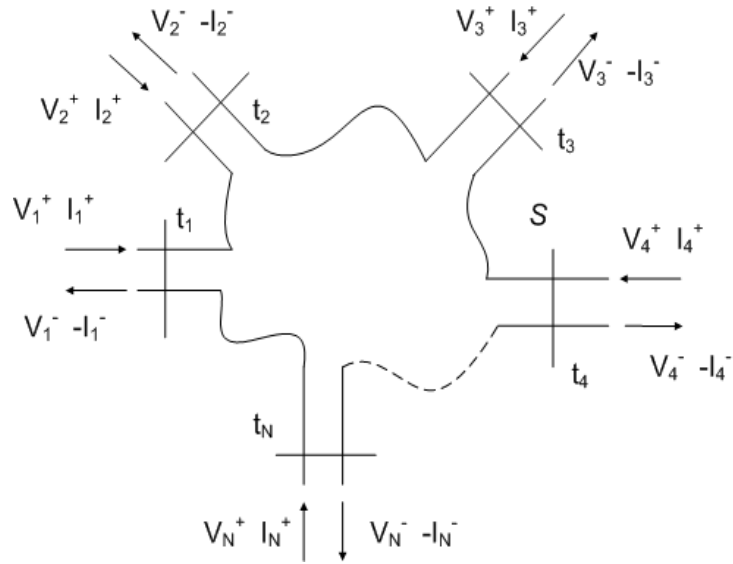
Figure 2-11 Arbitrary N-port microwave network [31]

$$\begin{bmatrix} V_1^- \\ V_2^- \\ \cdot \\ \cdot \\ \cdot \\ V_N^- \end{bmatrix} = \begin{bmatrix} S_{11} & S_{12} & \dots & S_{1N} \\ S_{21} & \cdot & \cdot & \cdot \\ \cdot & \cdot & \cdot & \cdot \\ \cdot & \cdot & \cdot & \cdot \\ \cdot & \cdot & \cdot & \cdot \\ S_{N1} & \dots & \cdot & S_{NN} \end{bmatrix} \begin{bmatrix} V_1^+ \\ V_2^+ \\ \cdot \\ \cdot \\ \cdot \\ V_N^+ \end{bmatrix} \qquad 2.32$$

or

$$[V^-] = [S][V^{\mp}] \qquad 2.33$$

The individual elements of the S matrix can be found by:

$$S_{ij} = \frac{V_i^-}{V_j^+} , V_k^+ = 0 \ for \ k \neq j \qquad 2.34$$

S_{ij} can be found by feeding port j with an incident wave of voltage V_j^+ and measuring the reflected wave V_i^-, from port i. For this all the ports except the jth port are terminated in matched loads to avoid reflections. Thus, S_{ii} refers to the reflection coefficient at port i when all other ports are terminated in matched loads, and S_{ij} is the transmission coefficient from port j to port i when all other ports are terminated in matched loads. Therefore in the S matrix all the diagonal elements refer to reflection coefficients of a particular port. The off-diagonal elements are called transmission

coefficients which describe the relation between one port and another [31]. The first number in the subscript corresponds to the responding port, while the second number refers to the incident port. Thus S_{21} means the response at port 2 due to signal at port 1. Example for a 2 port network is as shown below

$$\begin{bmatrix} S_{11} & S_{12} \\ S_{21} & S_{22} \end{bmatrix} \qquad\qquad 2.35$$

Scattering parameters are important in microwave design because they explain device characteristics. In antenna design, return loss refers to the proportion of signal that reflects from the end of a transmission line when the signal is fed from the other end. The transmitted signal is reflected due to impedance mismatch and maximum power transfer will not be possible in this situation. That is why return loss is an important parameter in antenna design.

S parameters are dimensionless because they are the ratios of complex signals but they can be converted to decibels 'dB' by using the following formulas:

Reflection coefficient magnitude (dB) = $20\times log|S_{ii}|$ = Return loss

Insertion loss (dB) = $20\times log|S_{ij}|$
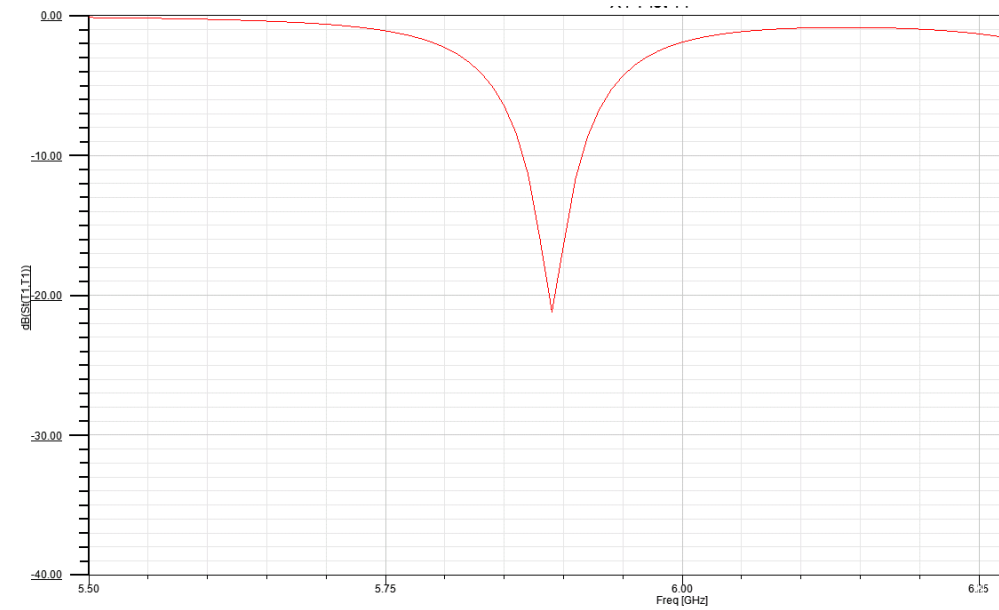
Figure 2-12 Return loss of a microstrip patch antenna

Figure 2.12 shows the return loss plot of an antenna, plotting $|S_{11}|$ in dB along the *Y*-axis and frequency along the *X*-axis. From Figure 2.12 it is possible to read the following. At frequency 5.5 GHz, S11 is 0dB, then there is no power transmission occurring. That means all power is reflected from the antenna port. If $S_{11} = -10$ dB then 10% of power is reflected from the antenna and 90% is transmitted or dissipated.

2.7 Dual-Frequency Microstrip Antennas

One of the drawbacks associated with a microstrip antenna is its bandwidth which restricts it from many applications. A dual-frequency antenna exhibits dual resonance behaviour in a single patch element. This advantage makes them in favour for application like wireless local networks, GPS, mobile phones and many other applications due to its compactness and low cost. This type of dual resonance helps to cover frequencies of interest in one design. Some of the design processes can be complex and complexity may increase when large arrays are considered mainly because of their feeding network.

24

For a dual frequency antenna both the resonance frequencies should operate with similar properties in terms of radiation and impedance. The simplest form of dual band antenna with two orthogonal linear polarisations can be obtained by feeding the rectangular patch along the diagonal [22, 32]. These antennas have two resonance frequencies which are orthogonally polarised. This design is advantageous as it has the ability to match impedance with a single feed. Another way to obtain dual frequency is by using multi-patch antennas. The advantage of these antennas is they can operate with the same polarisation at two frequencies as well as dual polarisation [33]. Feeding techniques can be placed either by conventional feeding arrangements or proximity coupling. Another approach to dual-frequency is by using resistive loading techniques with the patch antennas. An easy way to do this is by connecting a stub to one of the radiating edges in such a way that this stub introduces further resonant length [33]. Another approach to obtain dual-polarisation is by introducing slots along the edges of patch antennas [22].

Patch antennas have been employed for medical imaging and some of the designs used for breast cancer detection will be covered in Section 3.1.2. A dual band patch antenna was used in microwave tomography systems [34]. Other dual band patch antennas that are used for various applications can be found in the papers [35-37].

The Figure 2.13 shows some of the dual band antenna systems designed for various applications. Figure 2.13(a) is a proposed antenna designed for microwave tomography for BCD [34], Figure 2.13(b) is designed for WLAN operation [35], Figure 2.13(c) is a proposed design for mobile and wireless telecommunication [36] and Figure 2.13(d) for Ku-Band application [37].

Figure 2-13 Dual-frequency microstrip antennas
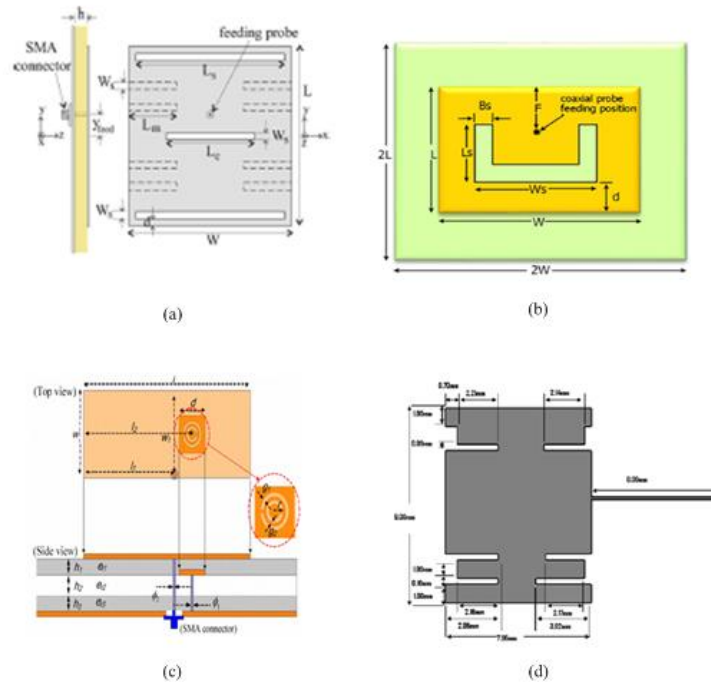
2.8 CAD Formula for Rectangular Microstrip Antenna

The following equations are based on the references [23, 29, 38, 39]. Consider Figure 2.7, a rectangular patch of length L, width W, on a dielectric substrate of permittivity $\in_r$ and height h.

The length of the patch determines the resonant frequency, f_r. The patch length L for the TM10 mode is given by

$$L = \frac{c}{2f_r\sqrt{\in_{eff}}} \qquad\qquad 2.36$$

Where $\in_{eff}$ is the effective dielectric constant given by [38],

$$\in_{eff} = \frac{\in_r + 1}{2} + \frac{(\in_r - 1)}{2}\left[1 + 12\left(\frac{h}{W}\right)\right]^{-1/2} \qquad\qquad 2.37$$

The width of the patch [23], where $W \ll L$, is

$$W = \frac{c}{2f_r}\sqrt{\frac{2}{\in_r + 1}} \qquad\qquad 2.38$$

where c is the speed of light. Because of the fringing effects, electrically the length of the patch looks greater than its physical dimensions. The extended distance ΔL is given by,

$$\Delta L = 0.412 * h * \frac{(\epsilon_{eff} + 0.30)(\frac{W}{h} + 0.264)}{(\epsilon_{eff} - 0.258)(\frac{W}{h} + 0.80)} \qquad 2.39$$

The effective length of the patch is,

$$L_{eff} = L + 2\Delta L \qquad 2.40$$

The antenna quality factor, bandwidth, and efficiency are interrelated. The quality factor (Q-factor) represents the antenna losses. The losses are associated with radiation, conduction (ohmic), dielectric and surface wave. Therefore the total quality factor Q_t of a patch can be written as [23]

$$\frac{1}{Q_t} = \frac{1}{Q_r} + \frac{1}{Q_c} + \frac{1}{Q_d} + \frac{1}{Q_s} \qquad 2.41$$

Q_t = total quality factor

Q_r = quality factor due to radiation (space wave) losses

Q_c = quality factor due to conduction (ohmic) losses

Q_d = quality factor due to dielectric losses

Q_s = quality factor due to surface waves

Dielectric Q, the dielectric Q factor is given by [40],

$$Q_d = \frac{1}{\tan \delta} \qquad 2.42$$

Where $\tan \delta$ is the loss tangent.

Conductor Q, the conductor Q factor is given by

$$Q_c = \mu_r \left(\frac{\eta_0}{2}\right) \left(\frac{k_0 h}{R_s}\right) \qquad 2.43$$

R_s is the surface resistance of patch and ground plane, σ is conductivity of the metal and the skin depth δ as

$$R_s = \frac{1}{\sigma\delta} \qquad 2.44$$

$$\delta = \sqrt{\frac{2}{\omega\mu_0\sigma}} \qquad 2.45$$

Space-wave Q, this accounts for the radiation into space

$$Q_r = \frac{3}{16}\left(\frac{\epsilon_r}{P_r c_1}\right)\left(\frac{L_{eff}}{W_{eff}}\right)\left(\frac{1}{h/\lambda_0}\right) \qquad 2.46$$

$W_{eff} = W + 2\Delta W$ is the effective width of the patch and L_{eff} is the effective length as shown in Equation 3.18 for $W << L$

$$\Delta W \approx h\left(\frac{ln4}{\pi}\right) \qquad 2.47$$

P_r and c_1 are given by [39]

$$P_r = 1 + \frac{a_2}{10}\left(k_0 W_{eff}\right)^2 + \left(a_2{}^2 + 2a_4\right)\left(\frac{3}{560}\right)\left(k_0 W_{eff}\right)^4$$

$$+ c_2\frac{1}{5}\left(k_0 L_{eff}\right)^2 \qquad 2.48$$

$$+ a_2 c_2\left(\frac{1}{70}\right)\left(k_0 W_{eff}\right)^2\left(k_0 L_{eff}\right)^2$$

$$c_1 = 1 - \frac{1}{n_1{}^2} + \frac{2/5}{n_1{}^4} \qquad 2.49$$

Where $n_1 = \sqrt{\epsilon_r \mu_r}$ is the refractive index of the substrate, a_2, a_4 and c_2 are the constants.

$$a_2 = -0.16605$$

$$a_4 = 0.00761$$

$$c_2 = -0.0914153$$

Surface-Wave Q, the surface-wave power is considered as a loss when the substrate is assumed to be infinite.

$$Q_s = Q_r \left(\frac{e_r{}^{sw}}{1 - e_r{}^{sw}} \right) \qquad 2.50$$

where $e_r{}^{sw}$ denotes the radiation efficiency of the patch,

$$e_r{}^{sw} = \frac{P_r}{P_r + P_s} \qquad 2.51$$

where P_r is the radiated power into space and P_s is the surface-wave power. The efficiency is approximately that of a unit-amplitude infinitesimal horizontal electric dipole (hed) on the substrate. Therefore efficiency is given by

$$e_r{}^{sw} = e_r{}^{hed} = \frac{P_r{}^{hed}}{P_r{}^{hed} + P_s{}^{hed}} \qquad 2.52$$

For thin substrates,

$$P_r{}^{hed} = \frac{1}{\lambda_0{}^2} (k_0 h)^2 (80\pi^2 \mu_r{}^2 c_1) \qquad 2.53$$

And

$$P_s{}^{hed} = \frac{1}{\lambda_0{}^2} (k_0 h)^3 \left[60\pi^3 \mu_r{}^3 \left(1 - \frac{1}{n_1{}^2} \right)^3 \right] \qquad 2.54$$

therefore,

$$e_r{}^{sw} = e_r{}^{hed} = \frac{1}{1 + (k_0 h) \left(\frac{3\pi}{4}\right) \mu_r \frac{1}{c_1} \left(1 - \frac{1}{n_1{}^2}\right)^3} \qquad 2.55$$

Bandwidth

The frequency limits (lower and upper) at which the standing wave ratio (SWR) reaches maximum is defined as the bandwidth, assuming the patch is matched to the characteristic impedance. For a SWR=S, the bandwidth can be considered as,

$$BW = \frac{S - 1}{\sqrt{2Q}} \qquad 2.56$$

Radiation Efficiency

Radiation efficiency in terms of Q factor is given by,

$$e_r = \frac{Q}{Q_r} \qquad 2.57$$

2.9 Summary

Chapter 2 described the basic theory of the microstrip patch antenna, cavity model analysis of microstrip patches and the various parameters for designing the microstrip antenna for this research. The chapter also described the CAD model based on the cavity model for designing a patch element. The next chapter will cover the literature review.

Chapter 3 Literature Review

3.1 Microwave Imaging Techniques for Breast Cancer Detection

X-ray mammography is currently the most effective imaging tool for detecting breast cancer. Mammography is the imaging of a compressed breast that uses special low-dose X-ray radiation. Despite its recognized ability to detect tumors it suffers some limitations such as false negative rate (4-34%) [41] and a high false positive rate (70%) [42]. This method is uncomfortable for women and there is a small but significant risk of radiation induced carcinogenesis associated with the X-ray examination of the human breast.

Early stage breast cancer detection using microwaves has been explored by many researchers. Several promising methods have been evaluated and can be classified as passive, hybrid and active. Active methods explore a wide range of techniques for breast cancer detection including Microwave Tomography, Ultra-Wide Band (UWB) radar techniques and Microwave Holography.

3.1.1 Microwave Tomography

Microwave tomography aims to reconstruct the electromagnetic properties such as conductivity and permittivity of the object under observation. In microwave tomography, microwave transmitters are used to illuminate the object under consideration. The scattered signals from the objects are measured at numerous locations surrounding the object. The object shape and distribution of complex permittivities are obtained by knowing the incident fields and the measurement of the corresponding scattered signals. Clinical experiments were conducted by Dartmouth College imaging in the frequency range of 0.5-3 GHz [13, 43]. They used 16 monopole antennas each for transmitting and receiving in a fixed array and this provided a good dynamic range. The system is automated for antenna array position control. One

antenna transmits the signal and scattered signals are received in parallel at the remaining antennas. The antennas are arranged in a cylindrical pattern and the breast has to be immersed in a liquid for scanning. Figure 3.1 shows an array arrangement used by Dartmouth College, Hanover, using monopole antennas oriented in a vertical direction.

Figure 3-1 Monopole antenna array for tomography Imaging, Meany P.M et al. [44]

3.1.2 Ultra-Wide Band (UWB) Techniques

The first study of UWB radar for medical imaging was presented by Hagness et al [45] and is called Confocal Microwave Imaging (CMI). CMI technology is based on the FM chirp radar used for screening passengers at airports. In CMI the breast is illuminated with a low power ultra-wideband pulse using a number of antennas surrounding the breast. The receiving antennas effectively collect the reflected microwave signals whose relative arrival times and amplitudes contain sufficient information which can later be processed to determine the tumor location. In microwave imaging for breast cancer detection, significant scattering of signals is caused by the difference in the dielectric properties of normal breast tissue and the tumor.

The UWB techniques operate on the following basis: calibration, skin subtraction (to remove reflection from the skin), integration, radial spreading compensation and focusing [46]. The signals received contain early time content and late time content. The

early time content can be removed by calibration. The antenna array is rotated to subtract all unwanted signals. The rotation gives two sets of measured data. The unwanted signals, such as antenna mutual coupling or noise in the system, can be eliminated in this way. The late-time content contains the tumor response. The methodology and results are based on finite-difference time-domain (FDTD) modelling.

For radar based MI, researchers have developed various antenna systems. An antenna array using the bowtie antenna has been used for UWB MI [4]. Resistively loaded bowtie antennas have been employed for this. The antenna is embedded in a lossy dielectric which has similar dielectric properties to normal breast tissue. Coaxial cable transmission is used to feed the antennas. A Gaussian pulse containing a broad range of frequencies (5 GHz to 15 GHz) is sent to each antenna in turn to transmit the signal, and the neighbouring antennas collect the received signals. A network analyser is connected to measure the scattering parameters for analysis [5, 47]. The object under investigation or the antenna array is rotated to increase the information from the reflections. Monopole and dipole antennas were used in [48-51] and Vivaldi antennas in [52]. The measurements are mostly carried out in planar, cylindrical or hemispherical geometries depending upon the position of the patient. The scanning antennas are either scanned over the breast surface or the signals are transmitted through a medium. Figure 3.2 shows a few of the antenna designs used in the UWB techniques.

Figure 3-2 UWB antennas: (a) Bowtie antenna [4] (b) Monopole antenna [50] (c) Dipole antenna [51] (d) Vivaldi antenna [52] (e) Stacked-patch antenna array [6] (f) Wide-slot antenna array [12].

Microstrip based antenna designs for MI using radar techniques have been demonstrated by the University of Bristol in which they have developed hemispherical antenna arrays comprising of 16 and 31 antennas respectively [12]. The antenna was designed based on the stacked patch antenna [6] and wide-slot antenna [12]. The wide-slot antenna performance was excellent compared to the stacked patch antenna [53] and these antenna designs are able to operate in UWB mode.

3.1.3 Microwave Holography

Holography was originally developed by Gabor et al [54, 55] in optics. The implementation of optical holography has since been extended to microwave and acoustic holography [7, 56, 57]. These imaging techniques based on holography used the interference pattern of a reference wave with the wave scattered from the target. The interference pattern is recorded on an aperture called a hologram. The hologram is illuminated with the reference wave to reconstruct an image of the object. Modern microwave holography has been proposed for near-field analysis of antennas [11], biomedical imaging and concealed weapon detection [10]. It is quite distinct from

34

conventional holography techniques, as the magnitude and phase of back scattered signals are recorded. The data can be mathematically reconstructed in a computer, with reconstruction of the target based on a sequence of direct and inverse Fourier transforms.

Elsdon et al [8] introduced microwave imaging using indirect holography for breast cancer. Two stages are involved in microwave holographic imaging for breast cancer; the recording of a sampled intensity pattern and image reconstruction. The intensity pattern is obtained from interference between a scattered wave and a coherent plane wave introduced at an angle to the recording plane. An electronically synthesized wave is used as the reference wave with the object being illuminated with the microwave source. A fraction of the signal is fed through a variable attenuator and phase shifter to create a synthetic reference wave with constant amplitude and linearly increasing phase shift. A Hybrid tee is used to combine the scattered signal and the output of the reference wave is measured using a power meter. A Fourier transform is performed on the intensity pattern to obtain a pattern in the spatial frequency domain. Filtering removes the unwanted terms from the Fourier transform and then the inverse Fourier transform gives the original scattered field of the object in the measurement plane. A method to obtain 3D holographic image is by using two orthogonal holograms of the same image and following the same process as in 2D holography [10].

3.1.3.1 Single Frequency Microwave Holography

In single frequency microwave holography the data collection is performed by scanning a transmitting and receiver antenna over a 2D aperture that has an object under investigation (target) within the field of view. A simplified schematic for a single-frequency microwave transceiver is shown in Figure 3.3.
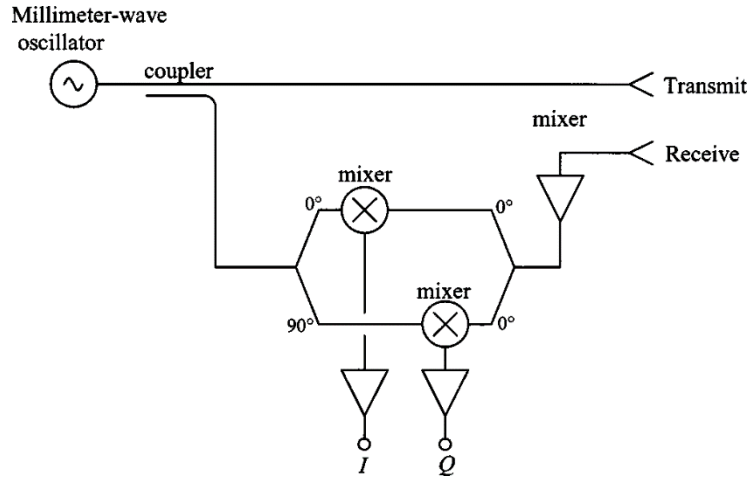
Figure 3-3 Single frequency microwave holography [58]

The signals are transmitted using a transmitter antenna and the reflected signals from the target received by the receiving antenna placed adjacent to the Transmitter antenna. The received signal is fed to mixers to produce in phase (0° phase shift) and quadrature (90° phase shift) signals. The output signals are called in-phase and quadrature for *I* and *Q* respectively. They contain the information on amplitude and phase of the scattered wave.

$$I + jQ = Ae^{-j2kR} \qquad\qquad 3.1$$

Where *A* is the amplitude of the scattered signal, *R* is the distance to the target, and *k* is the wavenumber, *k=ω/c,* where *ω* is temporal angular frequency and *c* is the speed of light. This signal is sampled over an *x-y* aperture using a 2D scanner to obtain the input to the image-reconstruction algorithm [58]. This single frequency measurement can provide a 2D image of the target's cross-section in a plane parallel to the acquisition plane.

Microwave holography uses a continuous wave for transmitting and the frequency of operation is typically 10 GHz. A pyramidal horn antenna is used in single frequency microwave holography to scan the object using a transmitting and receiving antenna [9].

3.1.3.2 Wide-band Microwave Holography

This method is similar to single frequency holography, with the extension to wide-band illumination, which allows for obtaining true 3D high resolution image of an object under investigation from a 2D planar aperture.
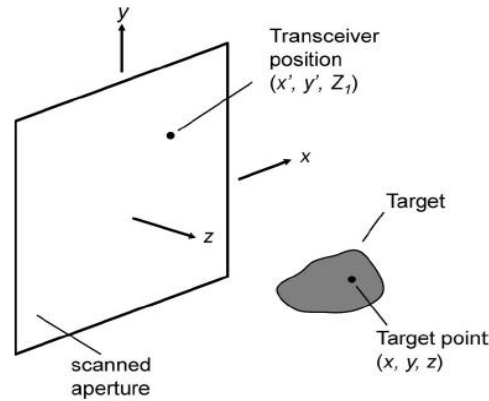
Figure 3-4 Wide-band microwave holography [58]

At each sampling point in the 2D plane, a wide beam-width transmitting antenna is used to emit the RF signal. The signal is swept over a wide frequency bandwidth and the transmitted signal illuminates the target and the scattered signal is recorded by a receiving antenna in the same 2D plane. The transceiver antennas are scanned simultaneously over the plane as in Figure 3.4. The data received will be unfocused so it is important to capture the phase of the scattered signal at each point in the aperture with the resulting I and Q signals being processed in a 3D imaging algorithm [59].

The application for medical imaging using wide-band holography is demonstrated using a dipole antenna [59]. Unlike the backscattering (transmitter and receiver on same plane) technique used in single frequency microwave holography, wide-band microwave holography uses the forward scattering technique. In the forward scattering technique, the transmitter and receiver antennas are facing opposite each other with the object under investigation in between. Both the transmitter and receiver antennas move

while scanning the object. The frequency of operation for wide-band holography was between 25 GHz and 45 GHz.

3.2 Application of Microstrip Antennas in other Fields

Microstrip antennas are widely used in wireless, mobile, satellite and GPS communication. Modern communication devices aim to reduce the size of their components. Microstrip antennas are compact in size and can be easily fabricated on surfaces using printed circuit board (PCB) technology. Microstrip antennas with antenna characteristics such as polarisation, dual-band, narrow and wide-band frequencies are of interest depending on the application.

Various microstrip antennas have been designed by researchers for wireless communications. Some of the designs are mentioned in this section. A wideband microstrip lotus antenna was designed to operate in between 1 GHz and 7 GHz [60] for GSM, ISM and WLAN applications, a dual-polarised antenna operating in narrow bandwidth [61], pentagonal antenna for ultra wideband application [62], and a loop antenna for wireless digital TV [63]. Dual-band, UWB microstrip antennas are used for satellite communication for mobile communication and navigation [64-72].

Microstrip antennas can also be found in radio-frequency identification (RFID) application. An RFID device basically contains a small chip and an antenna. They have many applications in our daily life. To increase the RFID reader coverage, an array of rectangular microstrip antennas has been designed [73], an edge slotted microstrip antenna for handheld reader [74]. For RFID tags, broadband microstrip antennas [75], monopole antennas [76], and circularly polarised antennas [77] are among the microstrip antenna designs for RFID applications. Figure 3.5 shows some of the microstrip antenna designs.

Figure 3-5 Microstrip antenna designs (a) Lotus Antenna [60] (b) Triangular slot Square patch antenna [61] (c) UWB pentagon antenna [62] (d) Truncated patch and ring patch antenna [71] (e) Miniature monopole antenna [76]

3.3 Summary

Chapter 3 provides a background study on various techniques and antennas developed for microwave breast cancer detection. The next chapter deals with patch antenna design and its major characteristics.

Chapter 4 Microstrip Antenna Design

4.1 Design Considerations

The resonant frequency for the design is considered first and the microstrip antenna design will be based on this. Similarly for a patch antenna the substrate chosen for the design and its height are also important. The following section discusses the frequency and substrate used for the antenna element design.

4.1.1 Frequency of Operation

The frequency range considered for this research project is in between 5-7 GHz. This frequency band has been chosen due to availability of components, manufacturing and cost effectiveness to build the whole system. The centre frequency of 6 GHz is used as the reference frequency for the design to determine the wavelength for the frequency band. The wavelength is given by

$$\lambda = \frac{c}{f} \qquad\qquad 4.1$$

Where $c = 3 \times 10^8 \text{m/sec}$, speed of light in vacuum and f being the frequency of operation. Therefore, the wavelength at the centre frequency is $\lambda = 5cm$.

4.1.2 Substrate Material and Height

The choice of the microstrip substrate and height affects the bandwidth of the patch antenna. Higher $\in_r$ values result in a smaller patch size therefore narrower bandwidth. The height of the substrate increases the bandwidth and the surface wave excitation [30]. High dielectric constant $\in_r$ increases the cost of the material and as the size becomes more compact it is harder to attain manufacturing tolerances. Therefore based on the availability of material, including cost factors, Rogers (Roger Corp) material RO4003C was used as the substrate. RO4003C has $\in_r = 3.55$ and $\tan \delta = 0.0027$, the height of the substrate is 0.0508 cm and the standard copper cladding is ½ ounce [78].

4.2 MATLAB

MATLAB [79] is an interactive environment for numerical computing using a high level language. The basic data element is an array that does not require dimensioning. This helps to solve matrix and vector computing problems, plotting of functions and data. MATLAB can be used to analyse data, develop algorithms, create models and applications. The MATLAB language provides tools and built-in math functions to solve numerical problems efficiently. MATLAB is the language of technical computing and it is used in applications such as signal processing, image processing, control systems, test and measurements, computational finance and computational biology.

MATLAB tools help to acquire and analyse data and it creates 2-D and 3-D plots with the help of built-in functions. MATLAB can access data from other applications. MATLAB can read data from Microsoft Excel, text, binary, images, sound and video files. The data analysis for this project is carried out in MATLAB. The results from HFSS (High Frequency Structure Simulator) and the data obtained experimentally from an Agilent (currently - Keysight Technologies) N5230A [80] network analyser are analysed using MATLAB.

4.3 ANSYS HFSS

HFSS is a simulation tool from ANSYS Corporation [81] for 3-D full-wave electromagnetic field simulation. HFSS allows the use of the finite element method (FEM) or integral equation method as a solver. HFSS can calculate matrix parameters like S, Y, and Z, resonant frequencies and fields (electric and magnetic). The near and far electromagnetic fields can be visualized in 3-D. This is useful for antenna design. Simulating a structure is simple in HFSS. The user provides the geometry, material properties, excitation and desired output. HFSS will automatically generate an appropriate, efficient and an accurate mesh for solving the problem using the selected

41

solver [81]. In FEM, HFSS divides the whole geometry into smaller elements of tetrahedrons. The field solutions are obtained for each tetrahedron. For this research project, scattering parameters are calculated by the antenna simulation. The S-parameter for the model is calculated by dividing the model into a finite element mesh. The meshed structure undergoes iterations with the previous one until it reaches a threshold level which is specified in the analysis setup. The field patterns are calculated assuming that only one port is excited at a time.

There are different radiation boundary conditions that can be used for the simulation. Boundary conditions are assigned so that radiation from the device does not reflect back to itself. For this research project PML (Perfectly Matched Layer) is used. PML allows waves to radiate infinitely far into space. It is a fictitious material that absorbs the electromagnetic fields impinging upon them. PML can only be placed on planar surfaces and they do not suffer from the distance or incident angle issues. It is required that PML is placed at least one-tenth of a wavelength from strong radiators.

The simulation is carried out in an IBM x3650 M3 computer with Processor Intel® Xeon® CPU E5620 at 2.40 GHz, RAM 18 GB, running Windows Server 2008 R2, 64 bit operating system.

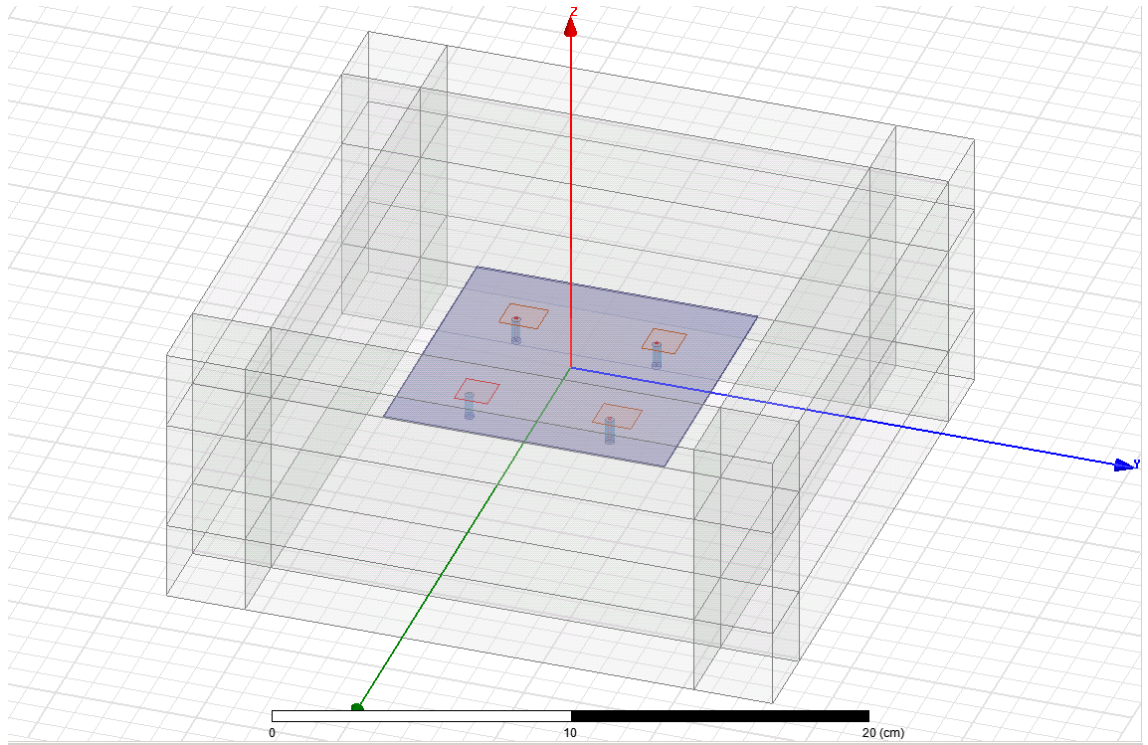Figure 4.1 shows the PML boundary condition applied for 2×2 antenna array.

**Figure 4-1 HFSS window showing PML boundary condition applied to a model**

4.4 Initial Antenna Design

The following sections below describe the important parameters for the design process and the development process of the antenna elements.

4.4.1 Circular Polarised Patch Antenna

The antenna design started with a circular polarised (CP) patch antenna. The idea was to use a circular polarised antenna to capture all the reflections (vertical and horizontal polarised signals) from the object under investigation. The antenna array design started by designing single antenna element. The centre frequency of 6 GHz is used as the resonance frequency. Circular polarised patch antenna design is based on [82]. The idea is to feed the antenna using a single feed point to obtain circular polarisation. The patch antenna designed looks like near square patch antenna as mentioned in [82]. The aspect ratio *a/b* is chosen such that the antenna radiates from both the edges at a single frequency with the same magnitude and a 90° phase difference.

43
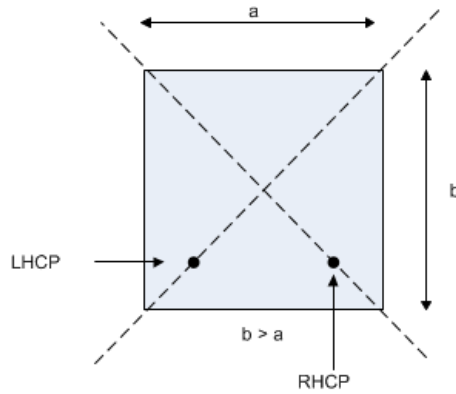
Figure 4-2 Near square CP antenna

The Figure 4.2 shows a near square patch antenna with a single feed location along the diagonal. The antenna will be left handed circular polarised if it is fed along the lower left diagonal and right handed circular polarised if the feed point is through the lower right along the diagonal. The radiation from the edges corresponds to two modes TM_{10} and TM_{01} having a phase centre which is located at the centre of the patch. When the patch dimension is $a=b$, it produces a slanted linear polarisation along the diagonal at far field, by adding the two modes. When the patch dimensions are changed such that $a>b$, the resonant frequency of each mode shifts. The two modes are not exactly in resonance at the same frequency. This causes the edge impedance of each mode to possess a phase shift. The total phase angle of 90° required for circular polarisation is obtained when the phase angle of one edge impedance is +45° and the other is -45°. The antenna element is designed to operate at 6 GHz, following the equations as described in Section 2.8.

The dimensions for a rectangular patch are obtained based on the equations in Section 2.8. The length and width obtained are $L=$ 1.31cm, $W=$ 1.66 cm and the total quality factor Q_t is 56. The square patch aspect ratio is adjusted to produce circular polarisation [82] and is described in [20].

$$\frac{a}{b} = 1 + \frac{1}{Q_t} \tag{4.2}$$

$$a = a' + \Delta L, b = a' + \Delta L \tag{4.3}$$

$$\Delta L = \frac{a'}{2Q_t + 1} \tag{4.4}$$

$$a' = \frac{L + W}{2} \tag{4.5}$$

The new dimensions after adjusting the dimensions based on [82] are a=1.50cm and b=1.47cm. A coaxial feed is used for the design which has a characteristic impedance of 50 Ω. The inner conductor is connected to the patch (in practice it will be soldered to the patch) and the outer conductor to the ground plane. Simulation was carried out using HFSS for the model developed with feed location along the diagonal. Coaxial cable RG 402 [83] was used as the feed. The feed location was varied along the diagonal as described in [82] to obtain 50 ohm impedance match. Figure 4.3 is the plot for the reflection coefficient as the coax feed varies along the diagonal of the patch.
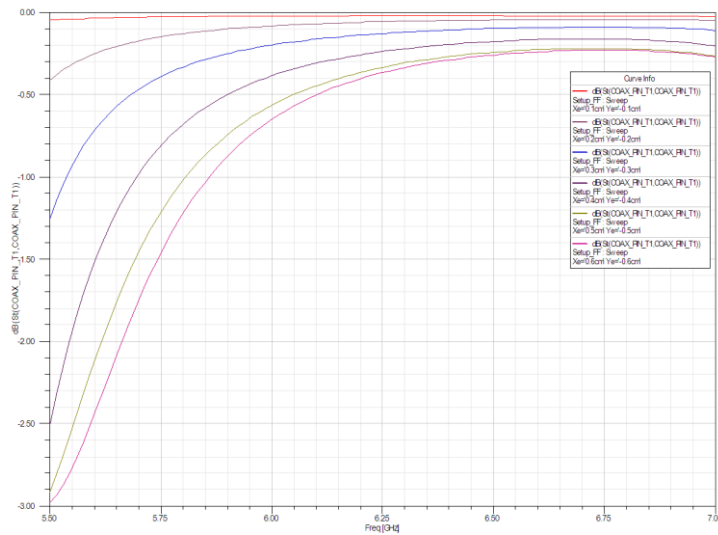

Figure 4-3 S11 as feed-point varies along the diagonal

The results for the designed patch show that the simulation never attained an impedance match and the plot for the reflection coefficient is shown in Figure 4.3. The circular

polarisation operation is possible only for a narrow frequency band. The correct dimensions were found through trial and error.

The orientation of the antenna in the simulation is as shown in the Figure 4.4. The centre is at *x*=0, *y*=0 and *z*=0. The axes are shown in positive directions with the positive *z* axis pointing towards the viewer.
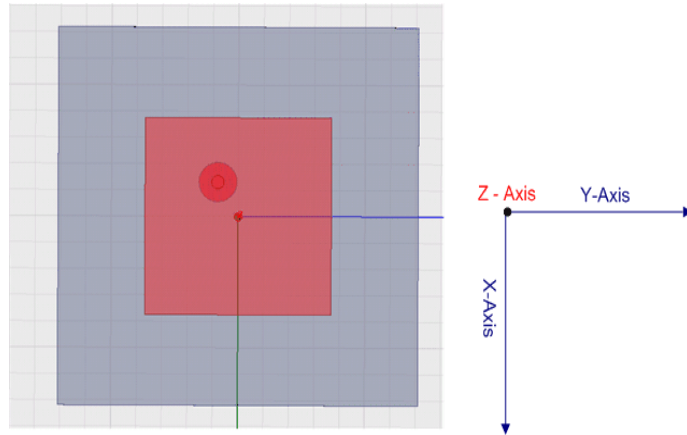
Figure 4-4 Coordinates of the patch antenna

The next step was to utilize the capabilities of the modelling software to its full extent. The patch antenna was designed using a trial and error method to obtain circular polarisation (CP) this was carried by optimising the feed location in one quadrant of the patch antenna element. The original dimensions for the 6 GHz resonance frequency design, *L*=1.31 cm and *W*=1.66 cm from the original patch design were kept constant. The Length *L*=1.31 cm was assigned as *a* in Equation 4.3 and the width *b*= 1.29 cm was obtained by substituting the total quality factor Q_t. Figure 4.5 shows the S$_{11}$-parameter for the feed varied along the diagonal of one quarter of the designed patch. The antenna impedance match -12.75 dB was obtained at 5.95 GHz at feed points (-0.2, -0.2), but the axial ratio magnitude which determines the CP was 10. Ideally it should be 1 for CP.
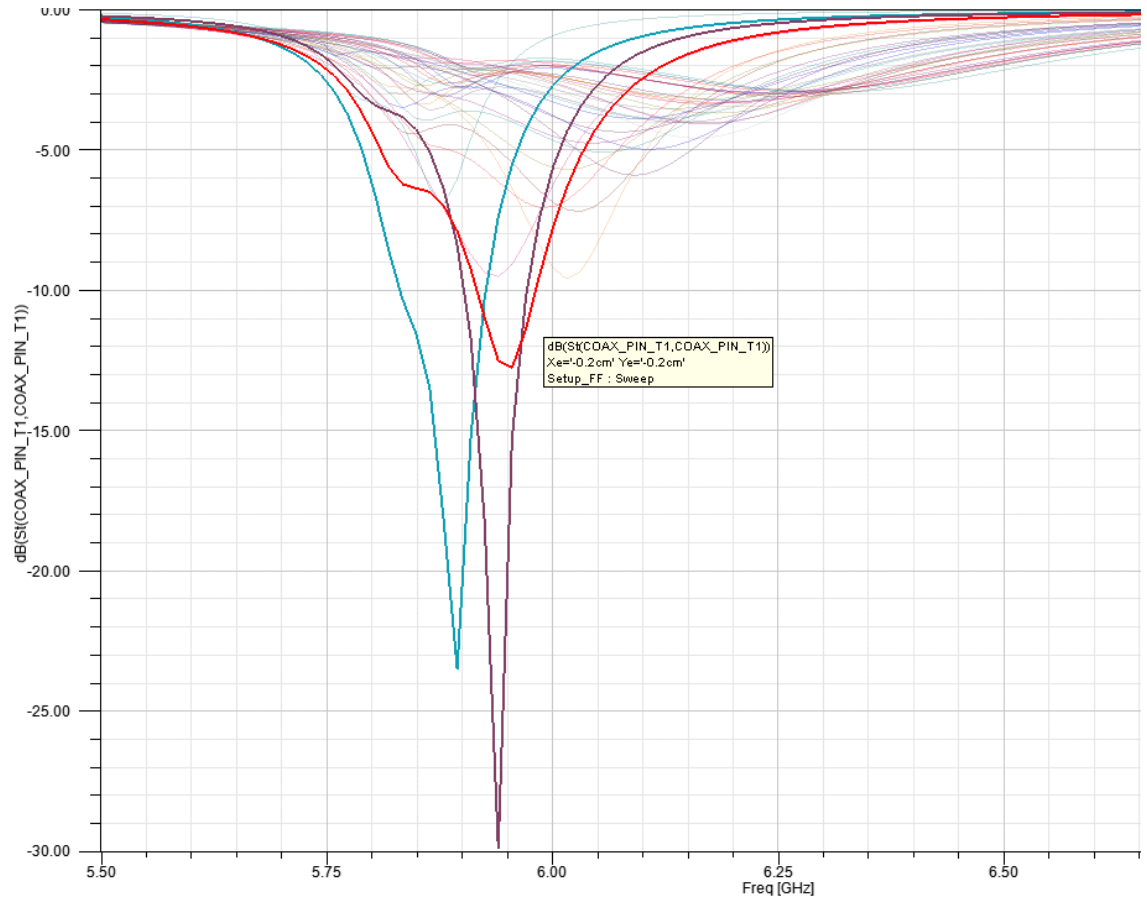
Figure 4-5 S11 of patch antenna in trial and error method

Since the simulation result shows an impedance match at (-0.2, -0.2) axis, the patch dimensions were varied to observe the CP and feed point variation. The feed points were fixed at (-0.2, -0.2) and the length was varied from 1.29cm to 1.33cm and the width from 1.26cm to 1.31cm in steps of 0.01cm. The simulation result showed the dimension of the patch with length 1.30cm and width 1.27cm which provided a sufficient impedance match of -11.10dB at 5.92 GHz and good axial ratio of 1.16. The feed point was optimized as (-0.26, -0.16) for the axial ratio of 1.16.

One of the practical issues faced with this design was to obtain the correct impedance match along with the required axial ratio for circular polarisation. Also the frequency of interest for the operation between 5-7 GHz and CP for a wide band operation is not easily achievable with this setup.

The second option is to design an antenna element that can produce two resonance frequencies (dual-band frequency). The frequency range between 5-7 GHz is divided into 4 so that two pairs of antenna can produce each pair of resonance frequencies. Simplicity was the key factor in developing the experimental setup. Also the resonances in the patch should be separated to eliminate any detection of unwanted signals at the receiving end. The idea of splitting the frequencies will help to construct an antenna array that can cover the whole frequency range of interest. Then the behaviour of the reflection can be analysed.

The dimensions for the dual frequency antenna elements are for the frequencies 5.6 GHz, 5.9 GHz, 6.2 GHz and 6.5 GHz. The corresponding dimensions are found using simple approximations based on the dimensions obtained from previous simulation results. The dimensions for the patch element were 1.30cm and 1.27 cm for the CP antenna (this dimension was obtained via simulation). The length 1.30 cm corresponding to 5.90 GHz was taken as a reference and the other lengths for the required frequencies found using the equations below.

$$1.3 \times \frac{5.9}{6.5} = 1.18 \ cm \rightarrow 6.5 \ GHz \qquad\qquad 4.6$$

$$1.3 \times \frac{5.9}{6.2} = 1.24 \ cm \rightarrow 6.2 \ GHz \qquad\qquad 4.7$$

$$1.3 \times \frac{5.9}{5.6} = 1.37 cm \rightarrow 5.6 \ GHz \qquad\qquad 4.8$$

So the new patch elements have the following dimensions 1.30 cm × 1.18 cm and 1.24 cm × 1.37 cm respectively. The antenna elements were simulated to determine the impedance match. The corresponding input reflection coefficient is shown in the Figure 4.5. Figure 4.6 (a) corresponds to 1.30 cm × 1.18 cm and Figure 4.6 (b) 1.24 cm × 1.37 cm. The patch antenna element was modelled in HFSS along with the PML boundary

condition is as shown in Figure 4.7. The size of the PML box is set to half a wavelength (3cm), at 5 GHz being the lowest frequency of operation.
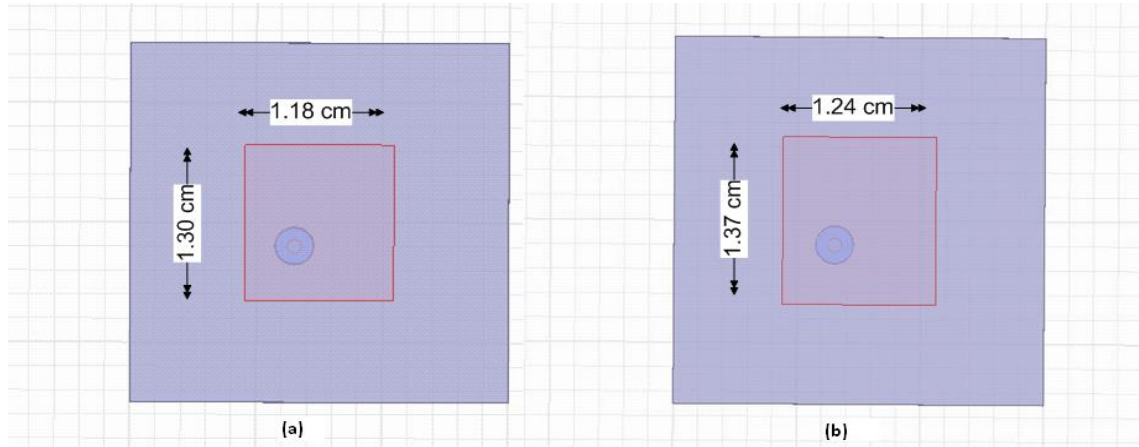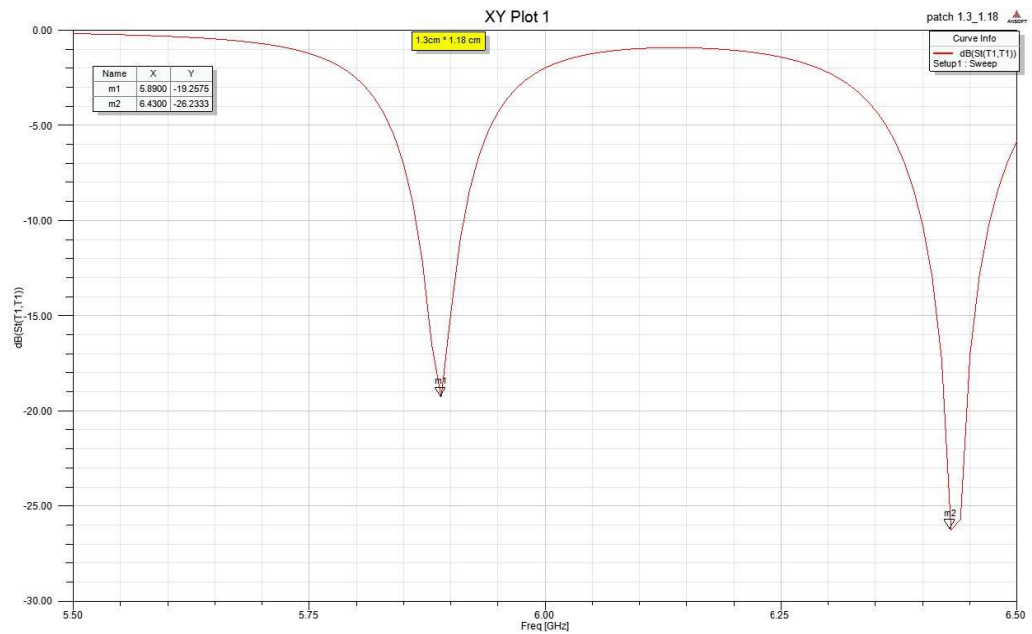

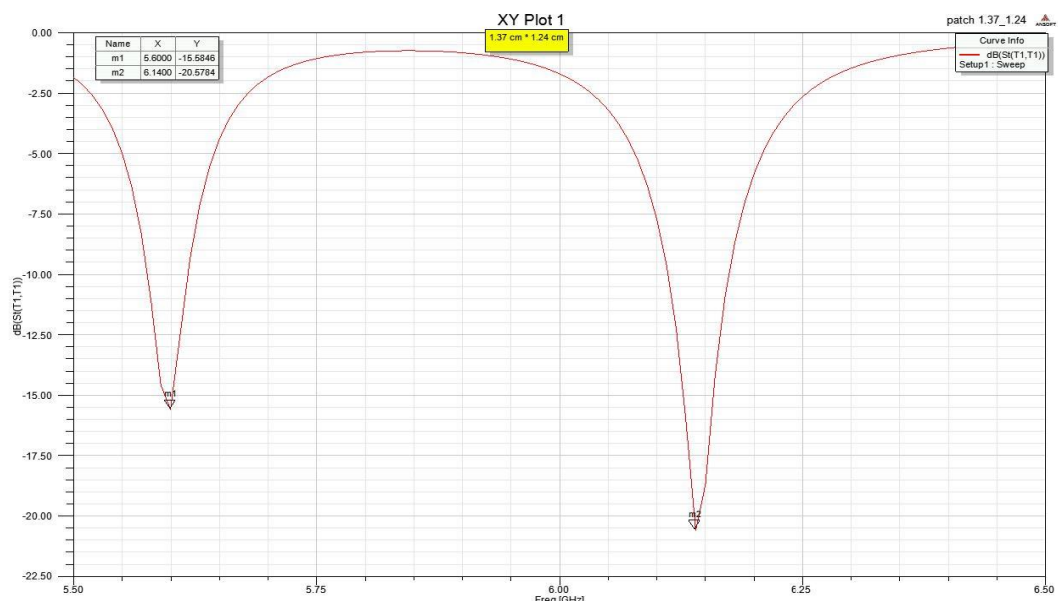**Figure 4-6 (a) Patch element 1 (b) Patch element 2**
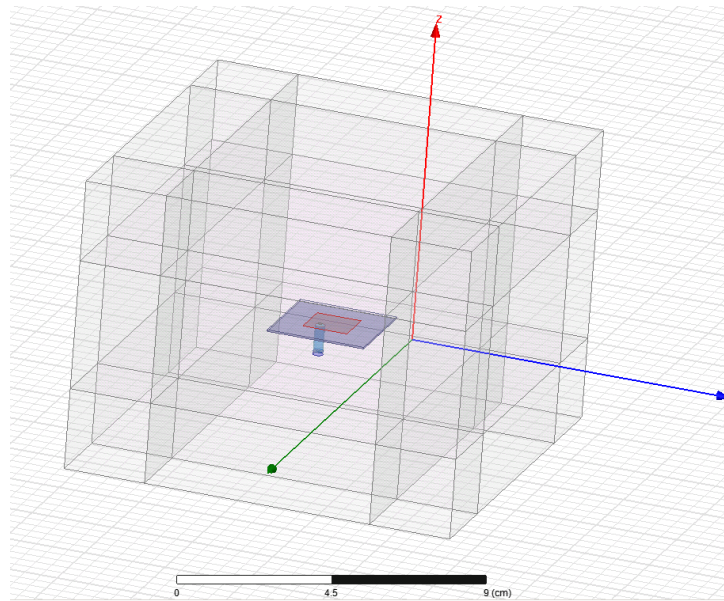
Figure 4-7 Single antenna element simulation in PML boundary

The simulated S11 for the patch element 1.30 cm × 1.18 cm is -19.25 dB (5.89 GHz) and -26.23 dB (6.43 GHz). For the 1.37 cm × 1.24 cm patches S11 is -20.57 dB (5.6 GHz) and -15.58 dB (6.14 GHz) respectively. Figure 4.8 shows the return loss for patch element 1.30 cm × 1.18 cm and Figure 4.9 for patch element 1.37 cm × 1.24 cm. The calculated resonant frequencies were found to agree reasonably well with simulation. The feed point for the coaxial inner conductor is at (0.2, -0.2) for both the antenna
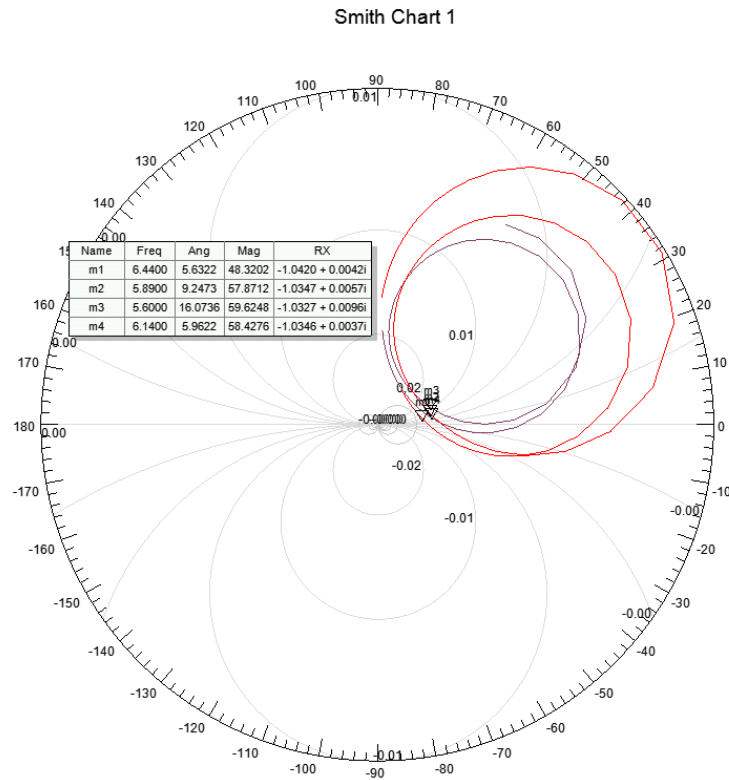
49

elements (with centres at x=0, y=0).The impedances for the designed antenna elements are plotted on the Smith chart as shown in Figure 4.10 The corresponding frequencies have been marked.

Figure 4-8 Return loss for patch element 1.30 cm × 1.18 cm

Figure 4-9 Return loss for patch element 1.37 cm × 1.24 cm

Figure 4-10 Impedance plot in Smith chart

4.5 Antenna Array Development

The four antenna elements were arranged on a 10 cm × 10 cm square dielectric with centre to centre distances between the patches equal to 5cm. The planar array configuration was chosen to keep the design simple and to be compactible with using rectangular antennas. The antenna elements in the substrate were arranged in two different patterns named as Model 1 and Model 2. In Model 1 the patch dimensions of diagonally opposite elements (see Figure 4.11) were the same. In Model 2, neighbouring patches had one equal length edge and one unequal length edge (see Figure 4.13). The two different simulation models allowed the analysis of the coupling and signal reception in the antenna elements with different patch configuration. All the simulations were carried out with the PML boundary condition in HFSS allowing for radiation into space.

51

4.5.1 Antenna Array-Model 1

The antenna element for this simulation setup is arranged on Rogers RO4003C dielectric substrate of sides 10 cm × 10 cm and thickness of 0.0508 cm. The distance between the centre of antenna elements is 5cm. The diagonal elements are the same, the *T1* and *T3* elements have the dimensions 1.30 cm × 1.18 cm whereas the *T2* and *T4* have dimensions 1.37 cm × 1.24 cm respectively. The centre of the substrate is located at x=0, y=0 and the feed locations for *T1* and *T3* are (2.7,-2.7), (-2.3, 2.3) and for T2 and T4 are (2.7, 2.3), (-2.3,-2.7). Figure 4.11 shows the arrangement of the antenna elements.
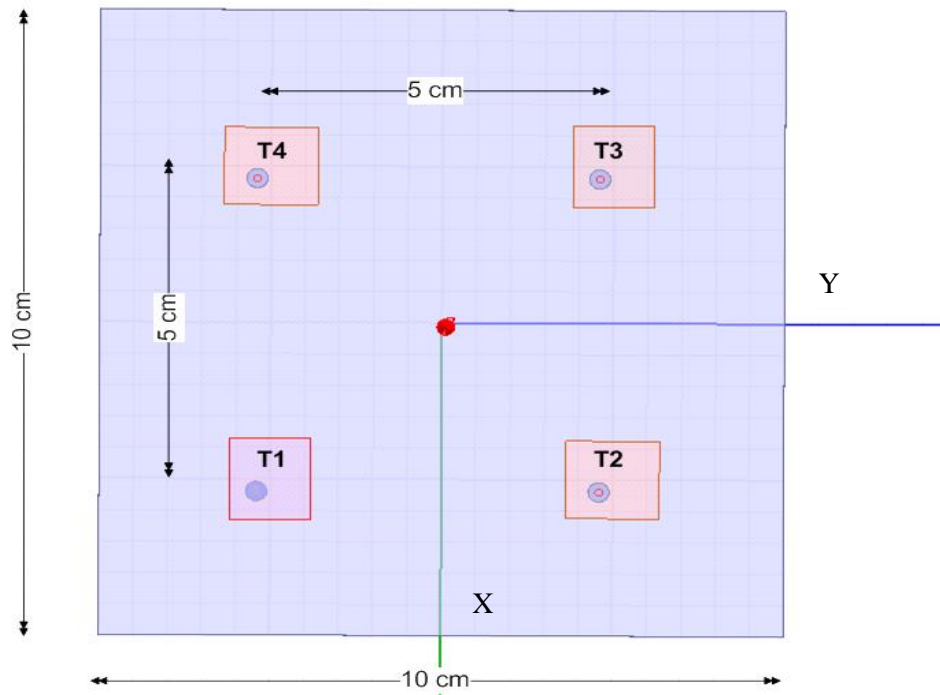

Figure 4-11 Antenna Array-Model 1

The magnitudes of the reflection coefficients (S_{11}) of the elements in the array for Model 1 are shown in Figure 4.10. In the figure each dip below -10 dB represents a resonant frequency.
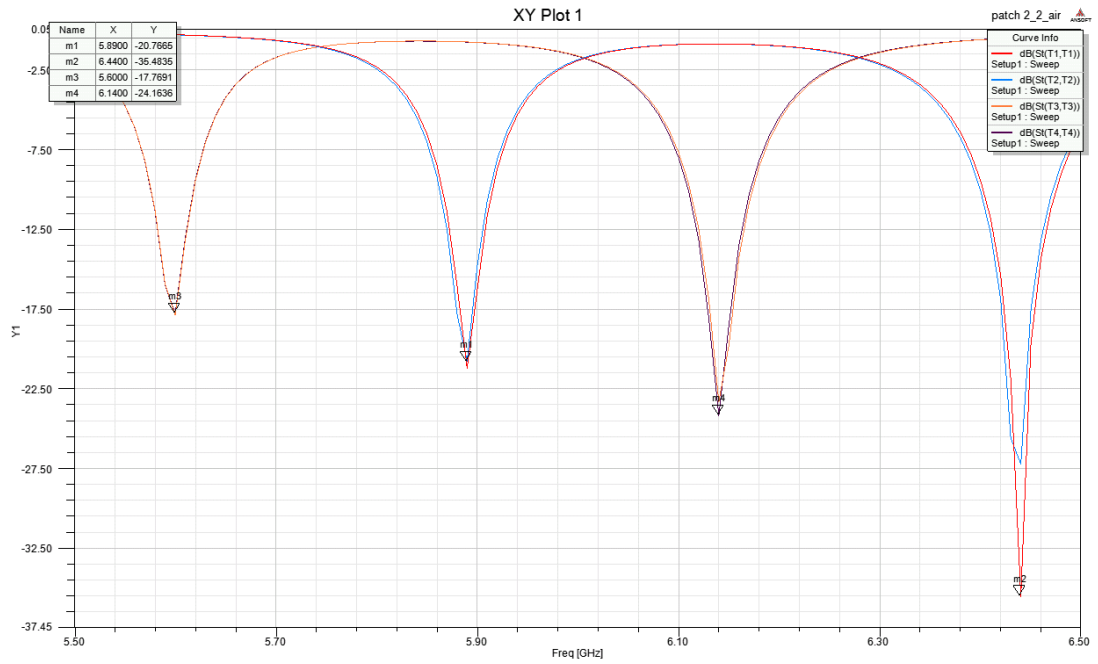
Figure 4-12 S11 of antenna elements in Model 1

4.5.2 Antenna Array-Model 2

The resonant frequencies of the antenna elements are arranged such that the resonant frequencies along the *X*-axis are constant and along the *Y*-axis are also constant. The centre to centre distances between the antennas are the same as in Model 1. The length and width of the elements were rearranged as shown in the Figure 4.13. *T1*= 1.30 cm × 1.18 cm, *T2*= 1.24 cm × 1.18 cm, *T3*= 1.24 cm × 1.37 cm and *T4*= 1.30 cm × 1.37 cm. The feed location of the antennas is optimized to get the best impedance match. Patches *T1* and *T3* are fed from (2.7,-2.7), (-2.3, 2.3) and *T2* and *T4* from (2.72, 2.3), (-2.3,-2.8) respectively. The return loss of the antenna elements for Model 2 are shown in Figure 4.14.

53

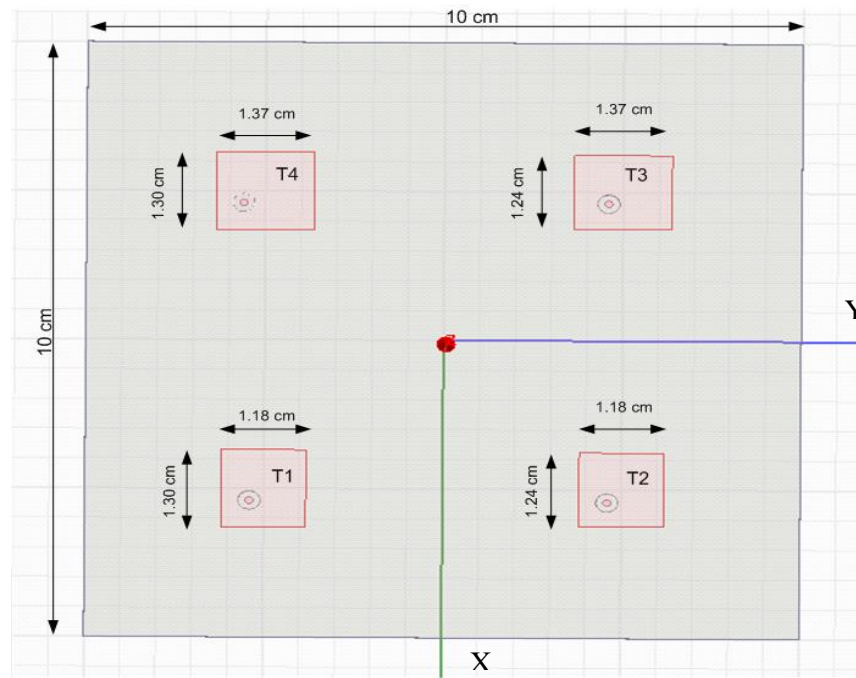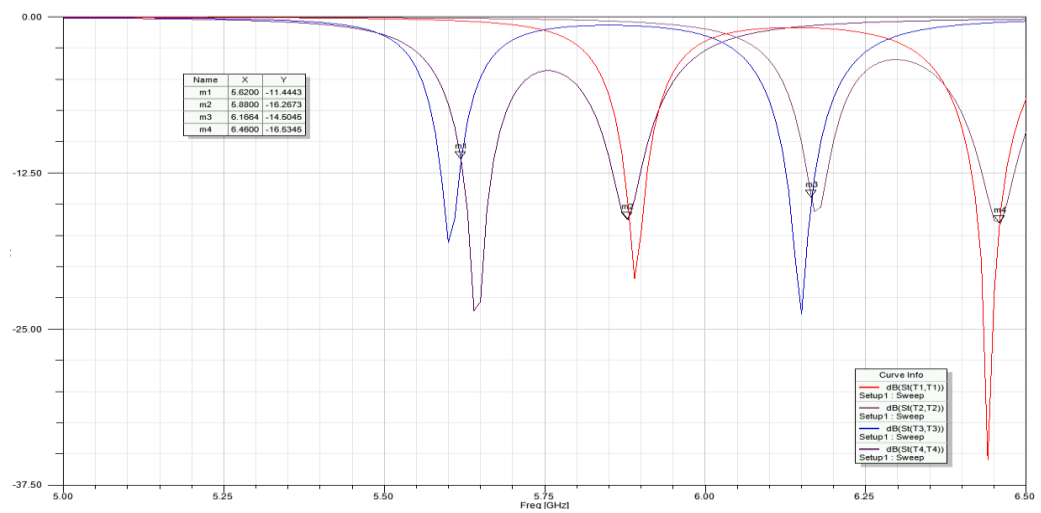**Figure 4-13 Antenna Array-Model 2**

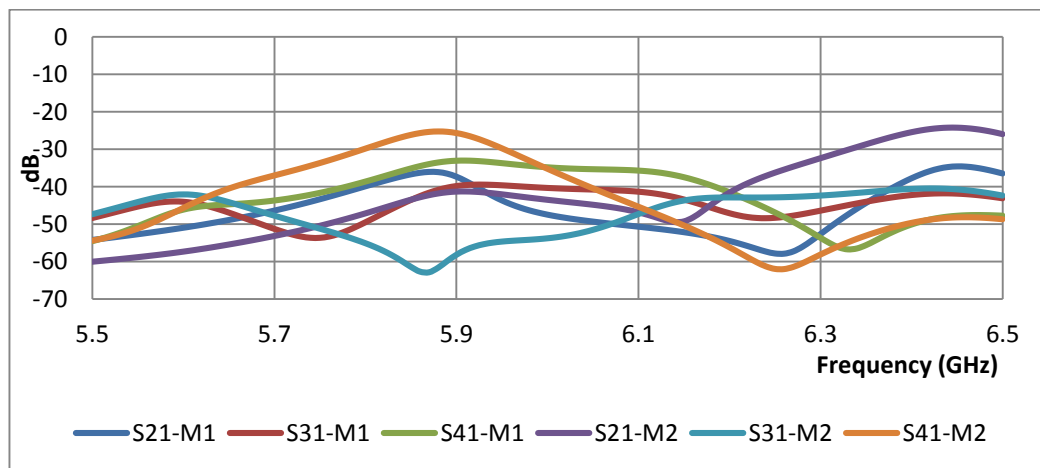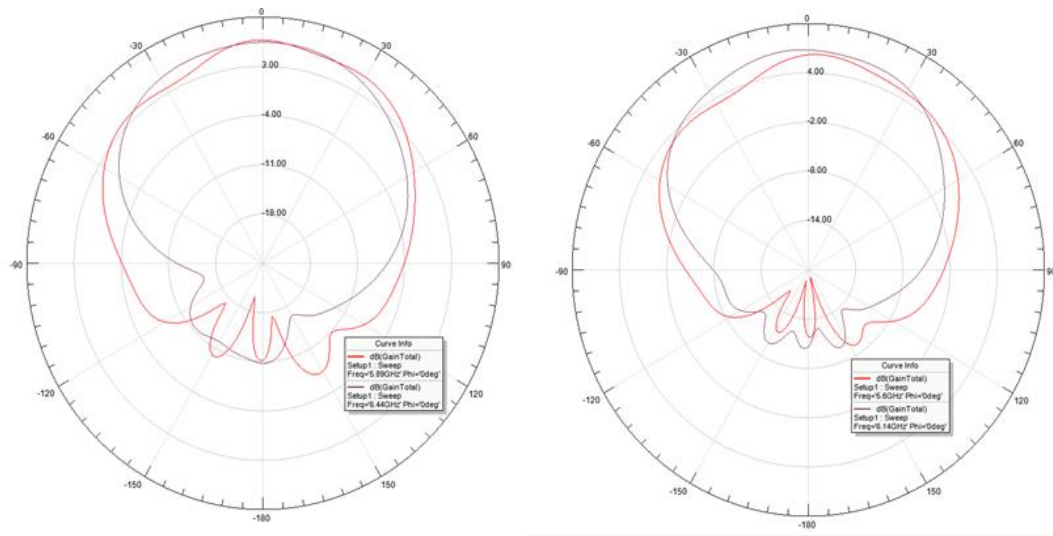**Figure 4-14 S11 of antenna elements in Model 2**

Figure 4-15 Mutual coupling for Model 1 (M1) and Model 2 (M2)

The mutual coupling between the antenna elements for Model 1 and Model 2 are shown in Figure 4.15. The results plotted are for antenna *T1* transmitting and the other patches receiving. The gain of antenna elements at the resonant frequencies are as shown in Figure 4.16. For Model 1 the peak gain is 6.7 dB and for Model 2 the peak gain is 6.8 dB for $\theta = 0^o$ θ is the measured from the Z-axis as in Figure 2.8. For all the plots above, the simulation environment in HFSS assumes that the antenna is freely radiating to space.

Figure 4-16 Gain of antenna elements

For Model 2 there were significant variations in the resonant frequencies obtained because the patches did not have the same lengths on both sides. Figures 4.12 and 4.14 clearly show the mismatch in the S11 plots with different resonant frequencies for the same lengths in the patch. The antenna characteristics for Model 1 were very consistent (as expected) based on the simulation results. The electric field in the substrate for the resonant frequencies for Model 1 is plotted in the Figure 4.17 for resonant frequencies, (a) 5.89 GHz, (b) 6.44 GHz, (c) 5.60 GHz and (d) 6.14 GHz. The radiation efficiency results from the simulation for the corresponding resonant frequencies of the Model 1 array are shown in Table 4-1.
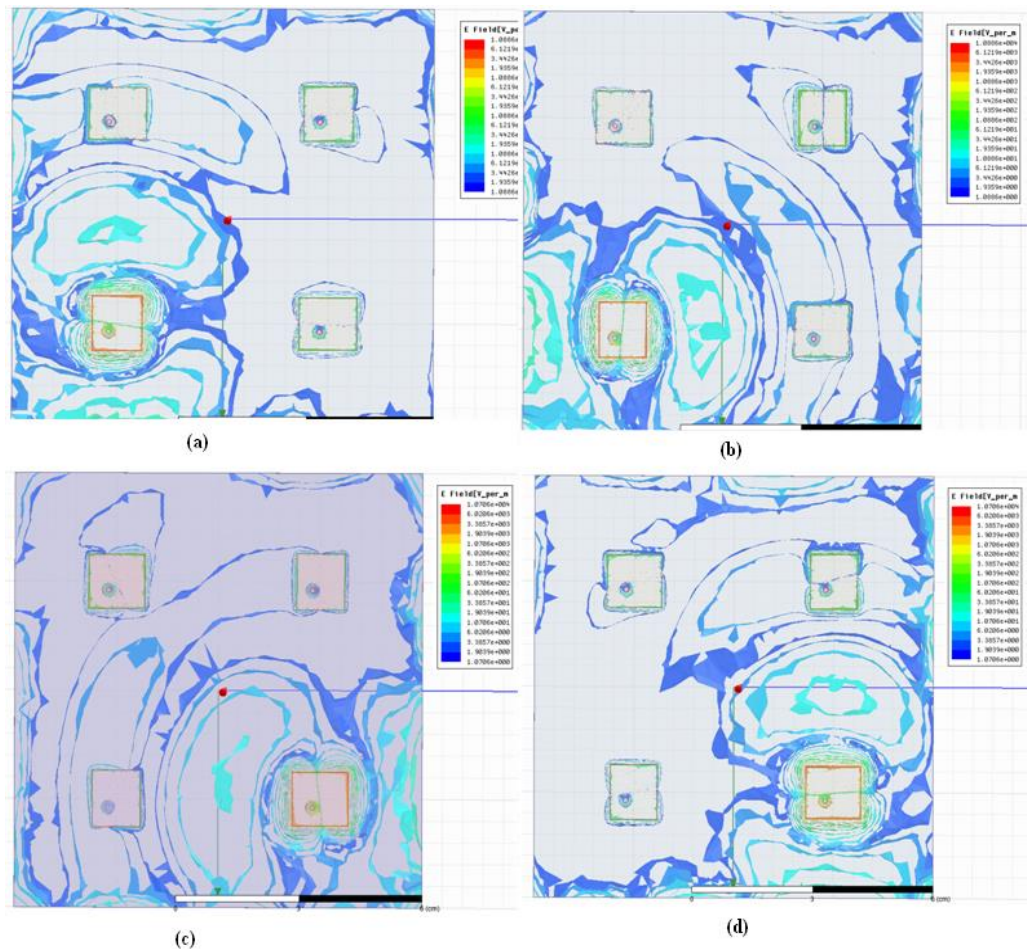
Figure 4-17 Electric field in the substrate (a) 5.89 GHz (b) 6.44 GHz (c) 5.6 GHz (d) 6.14 GHz

Frequency (GHz)	Radiation Efficiency (%)
5.60	77.75
5.89	79.86
6.14	83.45
6.44	86.12

Table 4-1 Radiation efficiency for patch Model 1

Model 1 was developed further to shift its resonant frequencies from 5.60 GHz and 5.90 GHz to 5.50 GHz and 5.75 so that the frequencies are more evenly distributed over the range 5-7 GHz. The new dimensions were calculated based on the previous simulated data. The lengths 1.37 cm and 1.30 cm were modified to 1.40 cm and 1.33 cm based on

the design experience gained from previous simulations rather than using the CAD formula in Section 2.8.

$$1.18 \times \frac{6.5}{5.75} = 1.33 \; cm \rightarrow 5.75 \; GHz \qquad 4.9$$

$$1.33 \times \frac{5.75}{5.5} = 1.40 \; cm \rightarrow 5.5 \; GHz \qquad 4.10$$

4.5.3 Antenna Array-Model 1 Redesigned

The Model 1 was simulated again the patch elements' lengths, widths and feed points were optimised to obtain the new dimensions. The new dimensions of the microstrip antenna elements were 1.33 cm × 1.18 cm and 1.26 cm × 1.42 cm. The size of the substrate was kept the same as in the previous design (10 cm × 10 cm). The optimized resonance frequencies were 5.46 GHz, 5.79 GHz, 6.10 GHz and 6.51 GHz respectively. The resonant frequencies for the new dimensions were close enough to the expected resonant frequencies in Equations 4.9 and 4.10. The reflection coefficient plot from the simulation for the new Model 1 2 × 2 array is shown in Figure. 4.18.
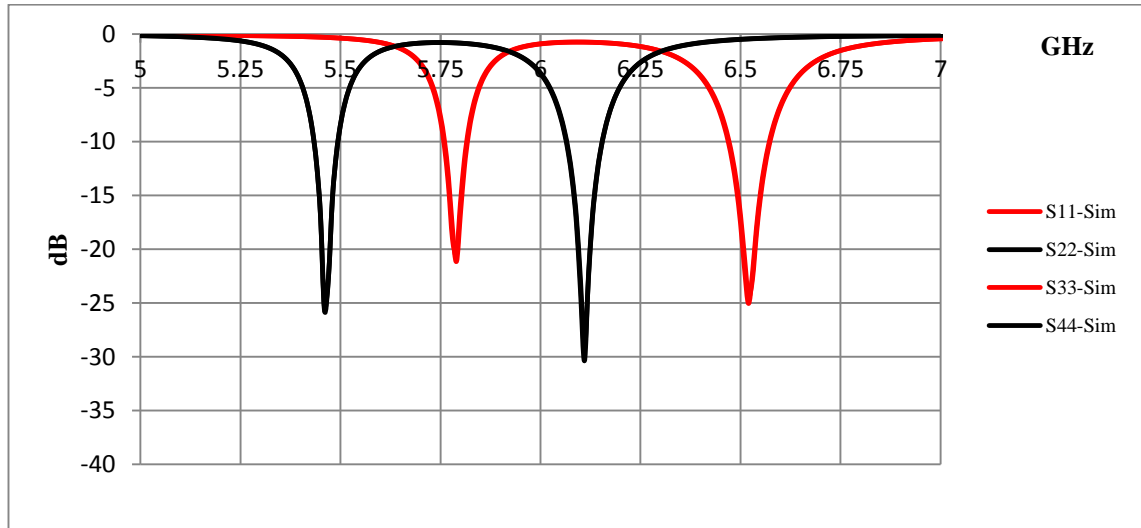

Figure 4-18 S11 plot for redesigned antenna array of Model 1

The antenna characteristics are compared for both the models. The input impedance of the antenna elements are compared in Table 4-2 and Table 4-3. The impedance at the feed points is closely matched for both the models.

Frequency (GHz)	Resistance (Ω)	Reactance (Ω)
5.45	54.43	-3.44
5.78	60.7	4.06
6.10	44.34	-4.63
6.50	44.22	-8.98

Table 4-2 Impedance of antenna elements in Model 1

Frequency (GHz)	Resistance (Ω)	Reactance (Ω)
5.46	58.39	-0.2731
5.79	59.02	10.82
6.10	51.36	-9.34
6.51	47.01	-10.81

Table 4-3 Impedance of antenna elements in Model 1 redesigned

The radiation pattern polar plot is shown in Figure 4.19 for the total gain of the redesigned antenna array. Table 4-4 compares the total gain for both the old and new Model 1 antenna arrays. The radiation efficiency for the redesigned elements at corresponding frequencies is shown in Table 4-5, which is similar to Model 1 as shown in Table 4-1.
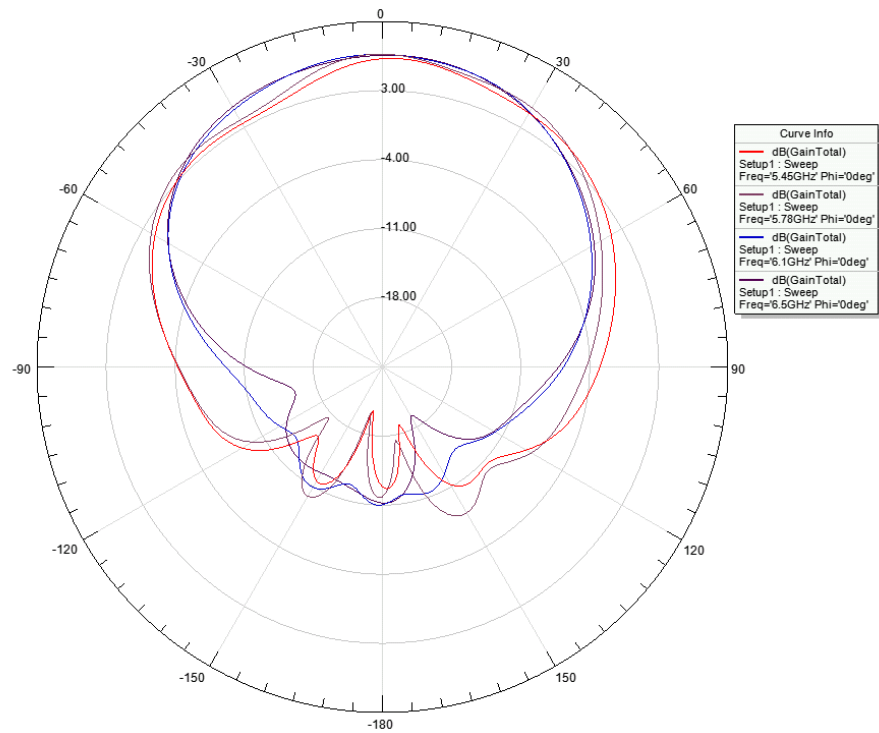
Figure 4-19 Radiation pattern for redesigned antenna array

Frequency (GHz) Model 1/ Model 1 redesigned	Model 1-Total Gain (dB)	Model 1 redesigned-Total Gain (dB)
5.60/5.46	6.27	6.21
5.89/5.79	6.69	6.69
6.14/6.10	6.46	6.65
6.44/6.51	6.45	6.57

Table 4-4 Total Gain of antenna elements for the array models

Frequency (GHz)	Radiation Efficiency (%)
5.46	77.26
5.79	79.66
6.10	83.96
6.51	88.66

Table 4-5 Radiation efficiency for redesigned patch Model 1

4.6 Summary

This chapter shows the model development and design of the antenna elements. HFSS was extensively used to simulate the antenna array. This chapter also demonstrates the difference between the theoretical model development and simulation. The next chapter

outlines the experiment and simulation comparison of the antenna array Model 1 to find the antenna characteristics.

Chapter 5 Antenna Array Results

The previous chapter described the simulation results for the basic design parameters such as return loss, input impedance and resonant frequency. In this chapter the simulation results for the antenna array designed are verified experimentally. The antenna array model in Section 4.5.3 was developed for the initial experimental tests. For ease of manufacturing the array size was reduced to 7 cm × 7 cm to make the antenna array more compact. The new array configuration was simulated in HFSS software to identify any changes in the antenna parameters. The centre to centre distance between the patch elements is now 3.5 cm.

5.1 Experimental Model

The experimental antenna array model is built on Rogers 4003 substrate as mentioned in Section 3.6.2. Semi rigid coaxial cable RG402 of length 2.50 cm as well as PCB mount F-SMA (Female SubMiniature version A or simply called as SMA) connectors are used. Figure.5.1 shows the manufactured antenna arrays. F-SMA connectors are soldered to one end of the RG402 cable which in turn connects to the network analyser. Five antenna arrays have been built. Three of the arrays were connected using RG402 cable through F-SMA connectors. In the other two arrays, the F-SMA connectors are soldered directly to the PCB board. This arrangement is to find the effect of the coaxial cable length on the measurements. The antenna arrays are named as Patch1-SMA, Patch2-SMA, Patch3-RG, Patch4-RG and Patch5-RG, where Patch1-SMA and Patch2-SMA have the SMA connector soldered directly to the ground plane and Patch3-RG, Patch4-RG and Patch5-RG use the RG402 coaxial cable. These names will be used to address the experimental model in the following sections and chapters.
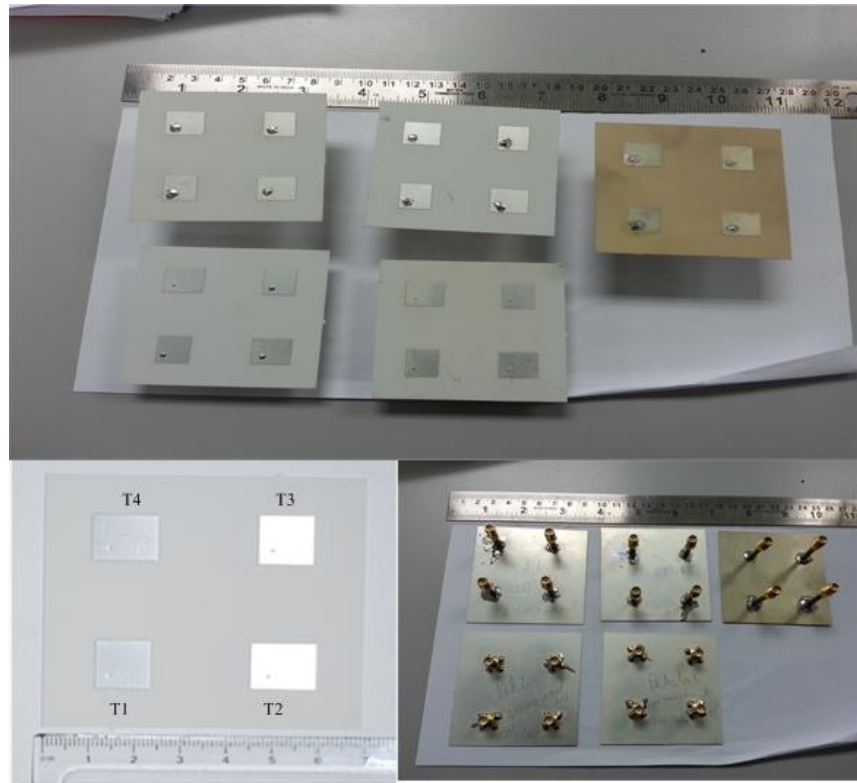
Figure 5-1 Antenna array developed for experiments.

The measurements are conducted with the antenna in a vertical plane. The antenna is held on a custom built holder which is 3-D printed from nylon. The antenna holder and the experimental setup for antenna array measurement when it is freely radiating to air is shown in Figure 5.2. The antenna array end is fixed to a measurement ruler which has got a linear scale marked in millimetres.
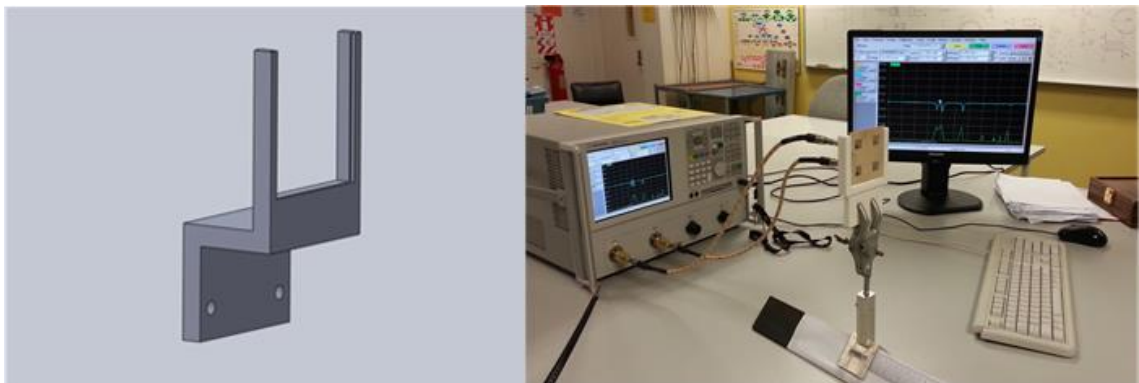
Figure 5-2 Antenna holder and experimental arrangement when antenna array freely radiating.

5.2 Measurement Set Up

The network analyser (NA) Agilent N5230A was used for the antenna array measurements. The network analyser is calibrated to compensate for errors associated with the instrument. The calibration technique followed for this measurement set up was SLOT (Short, Load, Open, Through). The Agilent 85052D 3.5 mm economy calibration kit was used to calibrate the network analyser. Only two ports were utilized for the measurements because of instrument difficulties using the 4 port calibration and measurements. Once the calibration was completed, the NA was used to make measurements on the antenna array. The calibration settings can be saved and they can be used for further measurements, if the test conditions are kept the same. Experimental setup is shown in Figure 5.2. Frequency sweeps between 5-7 GHz and 10 MHz-15 GHz were used, with the frequency changing in steps of 10 MHz. The longer frequency sweep range was used to examine the effect of higher frequency modes.

The antenna array measurement for air was conducted as follows. The terminals of the antenna array were considered as in Figure 5.1, so *T1* was connected to port 1 of the NA and *T3* is connected to port 2 to measure the respective antenna characteristics of these two patches. Then *T2* was connected to port 1 and *T4* is connected to port 2. The file format obtained was in Touchstone format. Each s2p file lists the input frequency and the 4 complex S-parameters (S_{11}, S_{21}, S_{12}, and S_{22}). The results obtained are exported into MATLAB for further analysis.
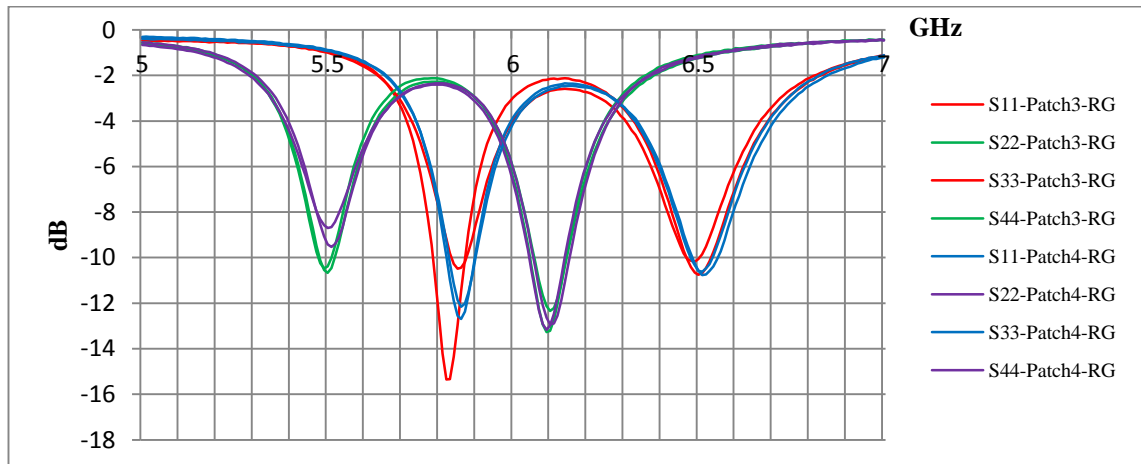
5.3 Experimental Results

The S-parameter values obtained from the NA were S_{11}, S_{31}, S_{13}, and S_{33} for the antenna elements *T1-T3* and is S_{22}, S_{42}, S_{24}, and S_{44} for the *T2-T4*. The return loss can be calculated from S_{11} S_{33} S_{22} and S_{44} and similarly the input impedance can be obtained by converting the S-parameters to Z-parameters Z_{11}, Z_{33}, Z_{22} and Z_{44}. The patch

Patch5-RG was not analysed due to damage to the coaxial cable and patch element while conducting the experiment. Figure 5.3(a) shows the return loss of antenna arrays Patch1-SMA and Patch2-SMA, and Figure 5.3(b) shows this for Patch3-RG and Patch4-RG respectively.
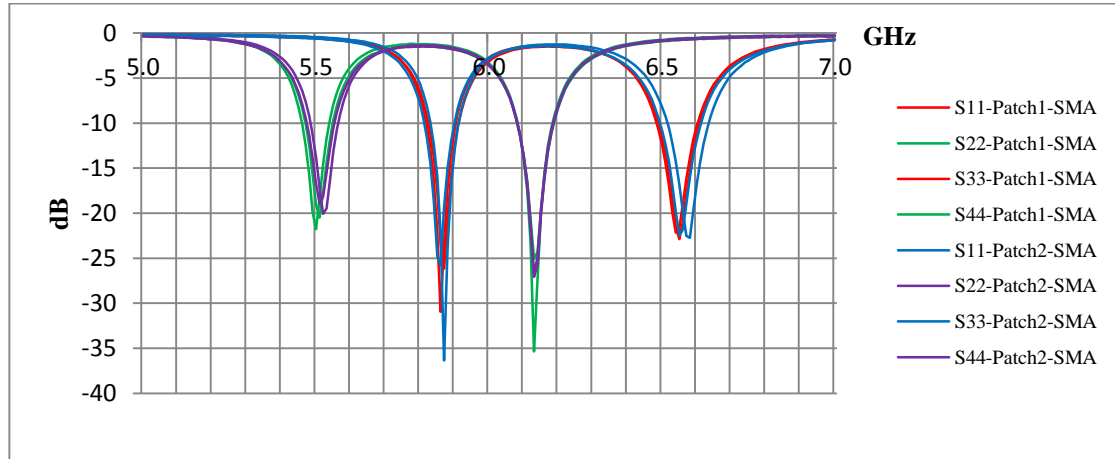

(a)

(b)

Figure 5-3 (a)-(b), (a) Return loss of antenna array with SMA connected to ground (b) Return loss of antenna array with RG402 cable

A comparison of the experimental results along with simulation is shown in Figure 5.4. This figure also shows simulation and experimental results for the higher order mode TM_{11}. The higher order modes were only examined to investigate any possible effect in the frequency range 5-7 GHz. Figure 5.4 clearly shows that the antenna array models with SMA connectors soldered on to ground plane have good return loss which signifies a good impedance match at the terminal. The results also show much better return loss

compared to the SMA connected boards. The S-parameter S_{11} and S_{33}, S_{22} and S_{44} are almost identical and one of each is shown in the figure below.
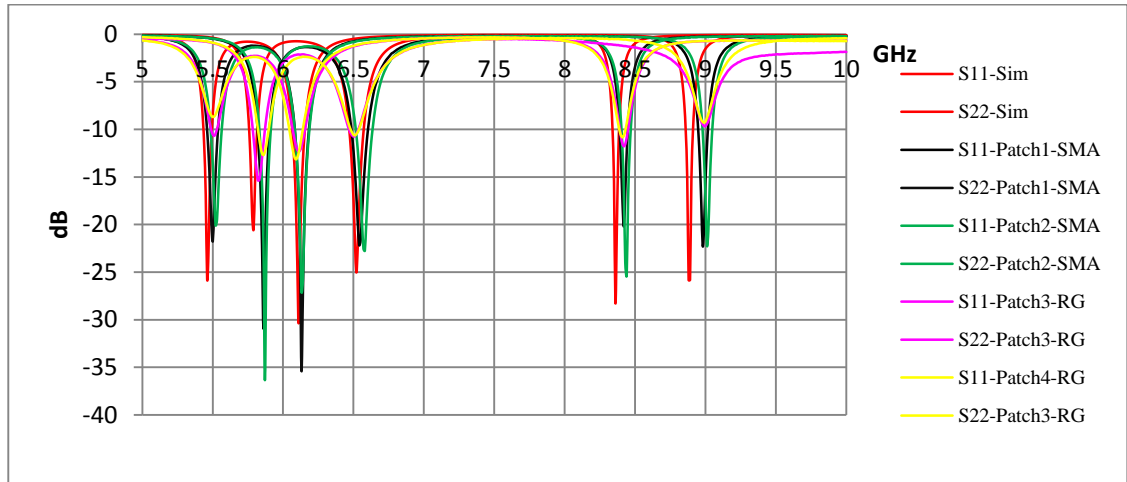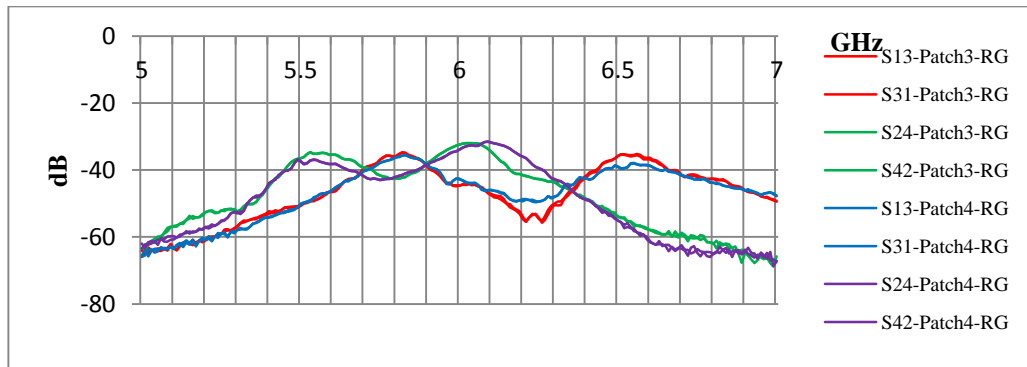

Figure 5-4 Return loss of antenna elements for simulation and experiment.

The coupling between the antenna array elements is shown in Figure 5.5. Only the major coupling between the elements is shown.
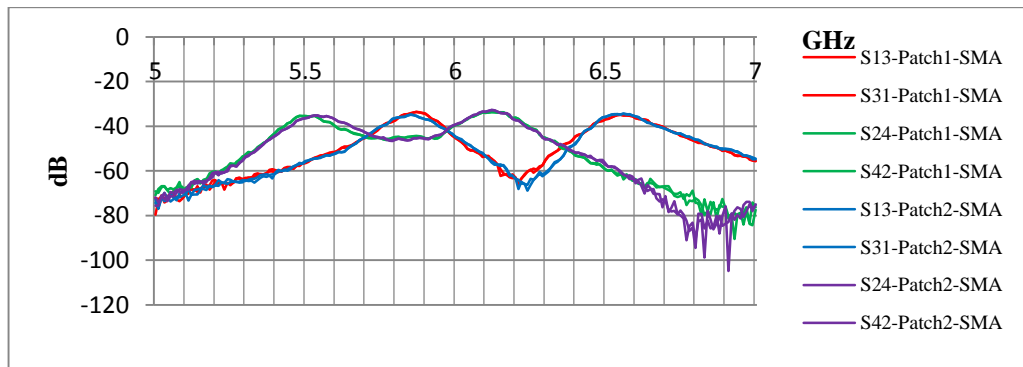

(a)

(b)

Figure 5-5 (a)-(b), (a) Coupling between antenna elements for SMA connected arrays (b) Coupling between antenna array elements with coaxial cable.

The comparison of coupling between the elements is shown in Figure 5.6. The coupling between the elements is less than -30dB. From Figure 5.5 it is clear that antennas of the same type have similar mutual couplings, so one of each is shown in the figure below.
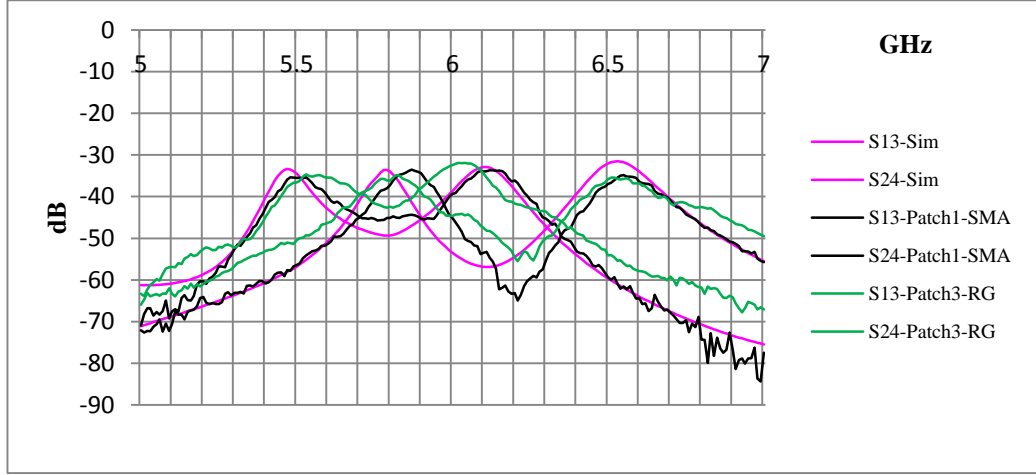
Figure 5-6 Coupling of antenna elements in simulation and experiment

In simulation the Z-parameters can be obtained directly from the simulation software but for the experiments the value of the input impedance at the terminal can be calculated from the S-parameter using the following equations [31]:

$$Z_{in} = Z_0 \frac{(1 + S_{nn})}{(1 - S_{nn})}$$
5.1

where Z_0, is the characteristic impedance, which is 50Ω in this case.

The comparison of the parameters from simulation and experiment is shown in Table 5.1. The resonant frequency, return loss and input impedance are compared for the array models; simulation, Patch1-SMA, Patch2-SMA, Patch3-RG and Patch4-RG. The resonant frequencies are slightly different from the simulation but the models with the same connectors/cables have very similar characteristics. The design and results from experiments shows that the antenna array developed has a good impedance match.

One of the reasons for the poorer performance of the RG402 coaxial cable connected antenna array could be due to the effect of soldering on the cable. There is a possibility that the dielectric material in the coaxial cable was changed due to thermal effects while soldering. In practice, the coaxial cable mounted antenna array was very hard to solder compared to the SMA mounted array, so repeated heating might have changed the dielectric properties.

F=Frequency in GHz, R=Resistance in ohm, X=Reactance in ohm, RL=Return loss in dB

Simulation				Experiment															
				Patch1-SMA				Patch2-SMA				Patch3-RG				Patch4-RG			
F GHz	R Ω	X Ω	RL dB	F GHz	R Ω	X Ω	RL dB	F GHz	R Ω	X Ω	RL dB	F GHz	R Ω	X Ω	RL dB	F GHz	R Ω	X Ω	RL dB
5.46	58.39	-0.27	-22.0	5.51	41.31	-10.6	-20.5	5.51	54.62	-10.5	-18.9	5.49	45.33	38.95	-10.5	5.48	47.52	32.37	-8.54
5.79	59.02	10.82	-18.4	5.87	42.92	-4.16	-26.1	5.87	56.07	-1.36	-36.3	5.84	61.09	25.6	-10.8	5.85	89.9	1.12	-12.6
6.10	51.36	-9.34	-26.4	6.13	51.41	-5.00	-25.1	6.13	52.31	-5.91	-26.8	6.11	70.06	22.04	-12.7	6.09	72.36	18.91	-12.6
6.51	47.02	-10.8	-21.2	6.55	45.14	-9.30	-22.9	6.58	62.31	4.17	-22.7	6.47	58.86	35.6	-10.1	6.49	86.15	10.62	-10.3

Table 5-1 Comparison between simulation and experimental results on antenna characteristics.

5.4 Summary

The antenna element parameters such as return loss, resonant frequency, input impedance and mutual coupling are experimentally verified with the simulation results. The design and manufactured arrays have similar characteristics for the SMA connected antenna array, whereas the coaxial cable connected antenna array performs less well. The next chapter focuses on reflection analysis based on the simulation.

Chapter 6 Analysis of Simulation Reflection Results

6.1 Model Development for Simulation Analysis

The simulation uses the PML boundary which is mentioned in Section 4.3. The simulation environment with an object is as shown in Figure 6.1. PMLs represent complex anisotropic materials. Tensors are designated as PMLs for each direction (axis). These PMLs are joined to form a box of PML walls. An air-box is created around the antenna array along with the OUI (object under investigation). PMLs are automatically created throughout the air-box face. The thickness of the uniform layer obtained is 3 cm and the minimum radiation frequency is 5 GHz. The minimum radiation frequency corresponds to the lowest frequency in the solution setup that has been used in the simulation. The calculated minimum radiating distance from the strongest radiating edge to the PML surface is 4 cm. The antenna elements are excited using a wave port assigned on the coaxial cable. The impedance of the terminal is 50 Ω.

The initial setup for the antenna array simulation is to calculate the antenna characteristics when it is radiating freely into space. In the second arrangement the setup includes a reflecting metal plate of size 11 cm × 11 cm and thickness of 0.20 cm. Metal was used as an object for measurement to maximize the reflection to the receiving antennas. To analyse the antenna reflection characteristics it is desirable to use object with known reflection coefficient and zero dielectric properties.

The metal surface is positioned parallel to the antenna array. The metal is placed at distances along the Z axis in steps of 1 cm from 1cm to 12 cm from the antenna surface. Figure 6.1 shows the antenna array element radiating to a metal plate 4cm away from the antenna elements.
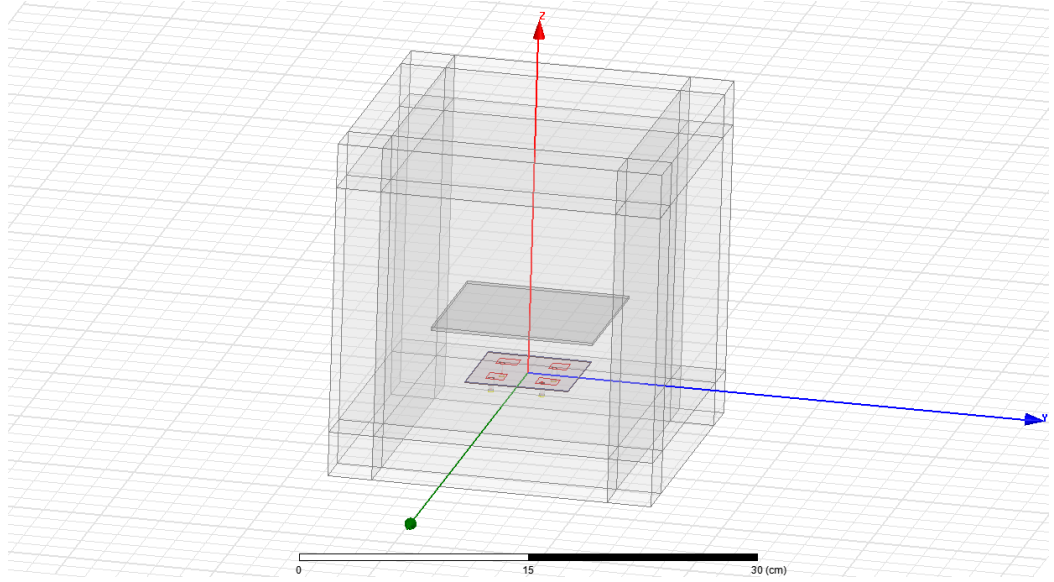
Figure 6-1 Model developed in ANSYS HFSS with metal plate in front of antenna array

The scattering parameters forming a 4×4 matrix were obtained from the simulation with corresponding real and imaginary parts for the frequency sweep for 5 to 7 GHz. The S-parameter matrix has the form:

$$S = \begin{bmatrix} S_{11} & S_{12} & S_{13} & S_{14} \\ S_{21} & S_{22} & S_{23} & S_{24} \\ S_{31} & S_{32} & S_{33} & S_{34} \\ S_{41} & S_{42} & S_{43} & S_{44} \end{bmatrix} \qquad 6.1$$

The terminals of the antenna elements in the array are named, *T1*, *T2*, *T3* and *T4* as in Figure 4.11. A fast sweep has been used in the simulation setup so that it provides a field solution for each step within a frequency range. The frequency was swept from 5-7 GHz on all the models with a step size of 10 MHz. The diagonal elements in Equation 5.1 give the values of the reflection coefficients while the off-diagonal elements correspond to the transmission coefficients.

6.2 Overview of Simulation Analysis with No Reflector

The antenna array model when freely radiating into space was simulated in HFSS as described in Section 4.5.3. The S-parameter results when freely radiating into space provide values for the reflection coefficients such as *S11*. The values of S-parameters

(such as S_{12}) measure the mutual coupling between the antenna elements. The data was exported and analysed in MATLAB.

6.3 Magnitude Analysis of the Simulation

The magnitudes of the transmission S-parameters have been calculated from the complex S-parameters. These magnitudes are plotted in Figure 6.2 (The reflection coefficients of the antenna elements in the array were described in Section 4.5.3, Figure 4.18.
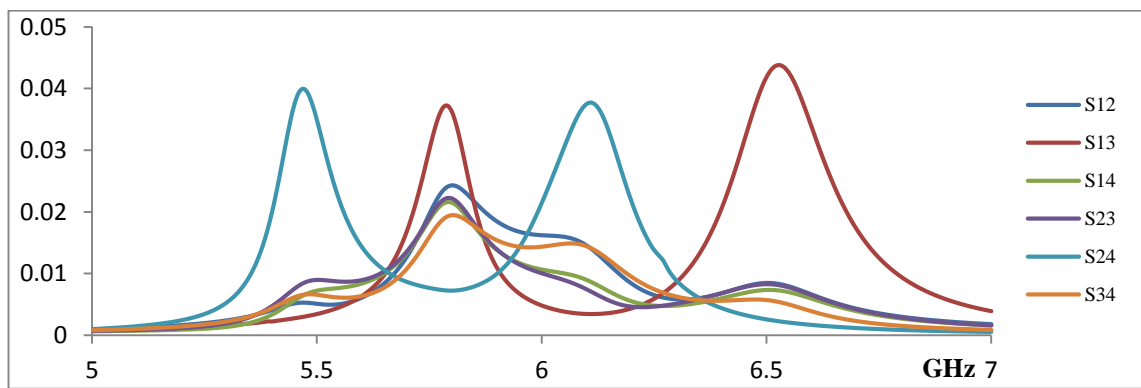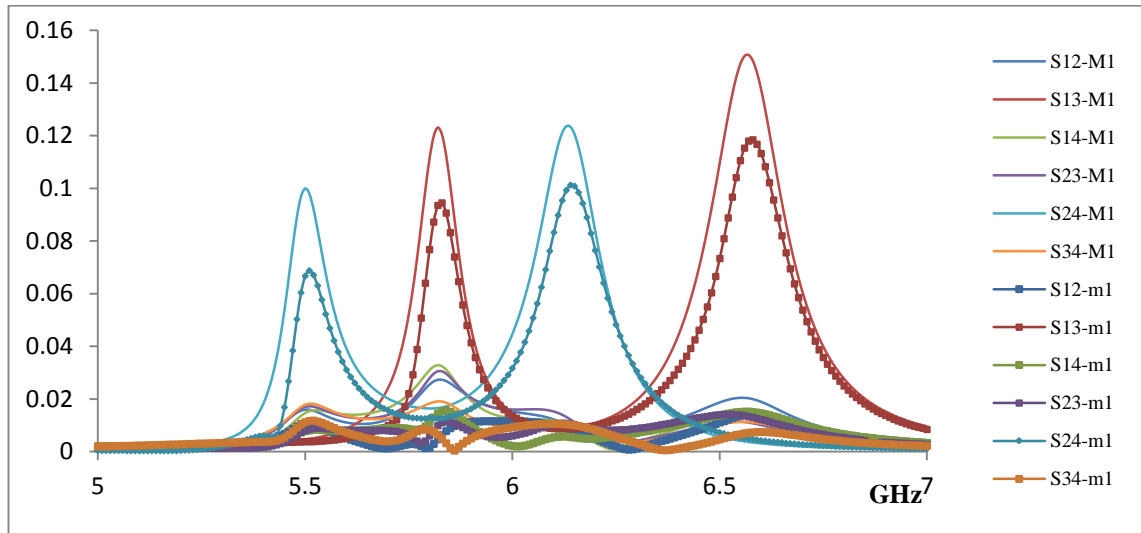

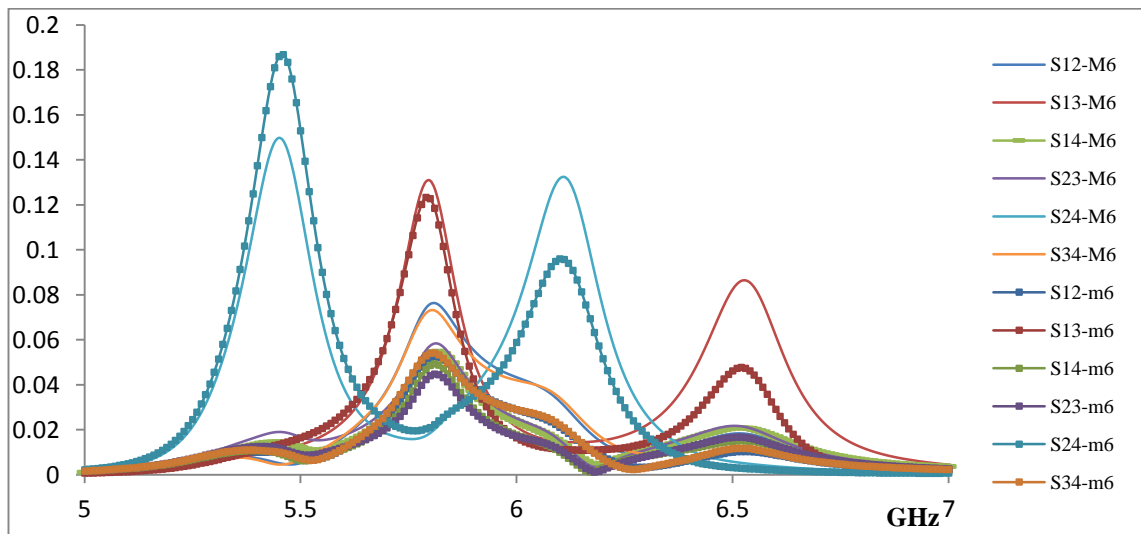**Figure 6-2 Magnitude plot of transmissions coefficient between antenna elements in air.**

In this antenna array arrangement, the maximum signal is transmitted between the pairs of patch elements with terminal numbers *T1-T3* and *T2-T4*. This is expected because these are the patches with the same resonant frequencies.

A simulation was then conducted using a metal plate as a reflecting object as described in Section 6.1. The idea of using metal as an object is to analyse the reflection and to find if the antenna element is able to detect reflection from the object and the location from where it is reflected. The metal plate is placed as shown in Figure 6.1 and it is moved along the *z* direction from 1cm above the antenna surface, up to 12 cm, in steps of 1cm. The S-parameter results are extracted from the simulations as the metal plate is moved.

The direct antenna coupling is removed from each metal reflection measurement by subtracting the air measurement S-parameter from the corresponding metal reflection S-parameter. Figures 6.3 (a)-(c) show the magnitudes of the S parameters for the measurements. Plots for reflector distances of 1 cm, 6 cm and 12 cm are plotted respectively. The legend in the plot shows the S-parameter, and the letter *M* corresponds to raw reflection results, and letter *m* corresponds to reflection results with coupling removed (dotted lines). The numbers following *M* or *m* show the step size in centimetres. The *X* axis is frequency in GHz and the *Y* axis is the magnitude of the S-parameter.


(a)

(b)
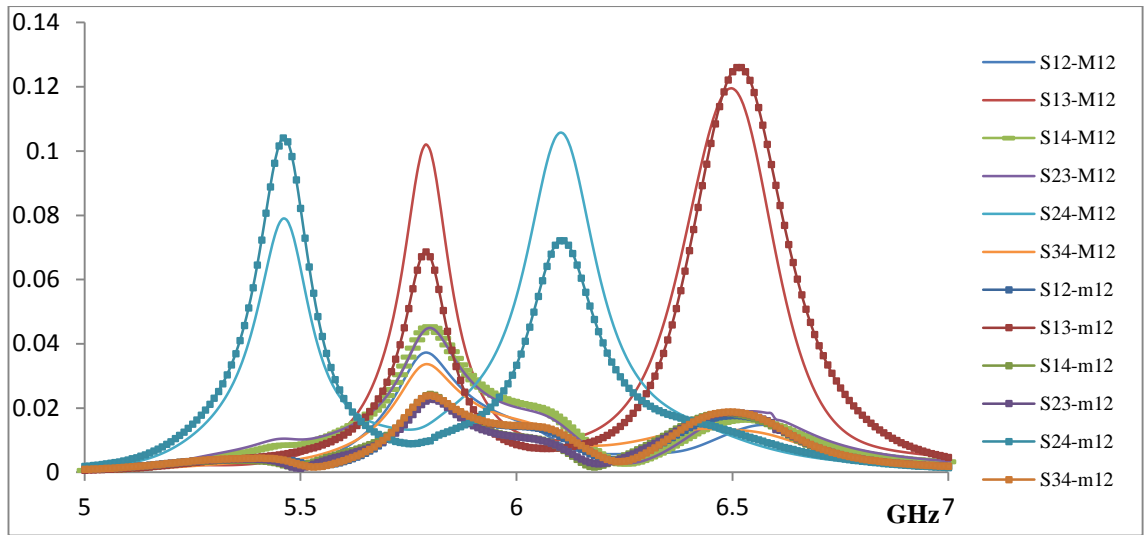
(c)

Figure 6-3 (a)-(c) Magnitude plot of transmissions coefficient between antenna elements on metal reflector, 1cm, 6cm and 12 cm distance.

From Figure 6.3 it is clear that only the major pairs, *T1-T3*, *T2-T4* have significant signal reception near their resonant frequencies. Figure 6.4 shows the amplitude variation for transmission between *T1-T3* and *T2-T4* after removing coupling, as the reflector moves from 1cm – 12 cm (*M1-M12*). The amplitude of the signal does not vary uniformly as the reflector distance changes from 1 cm – 12 cm.
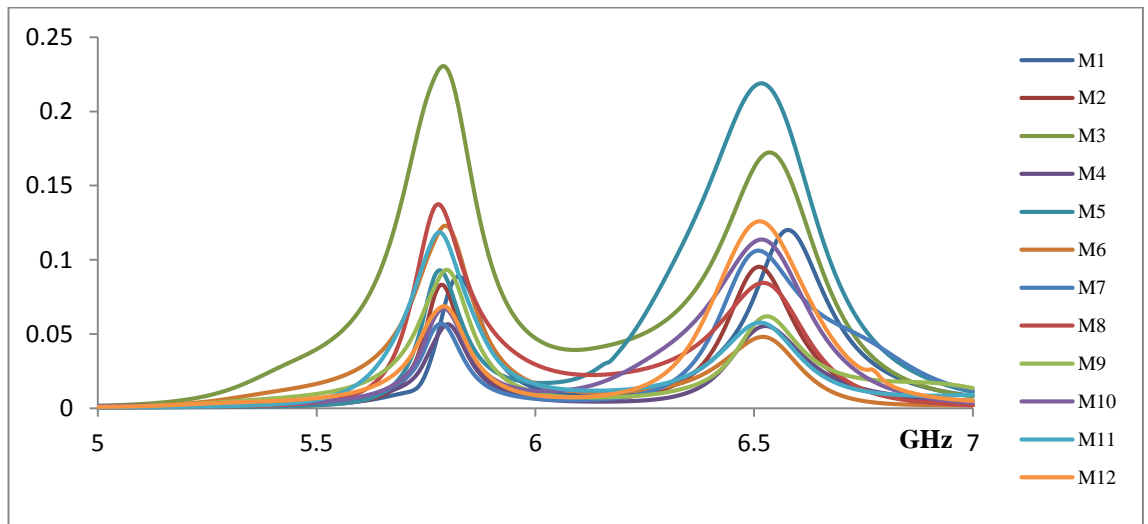

(a)
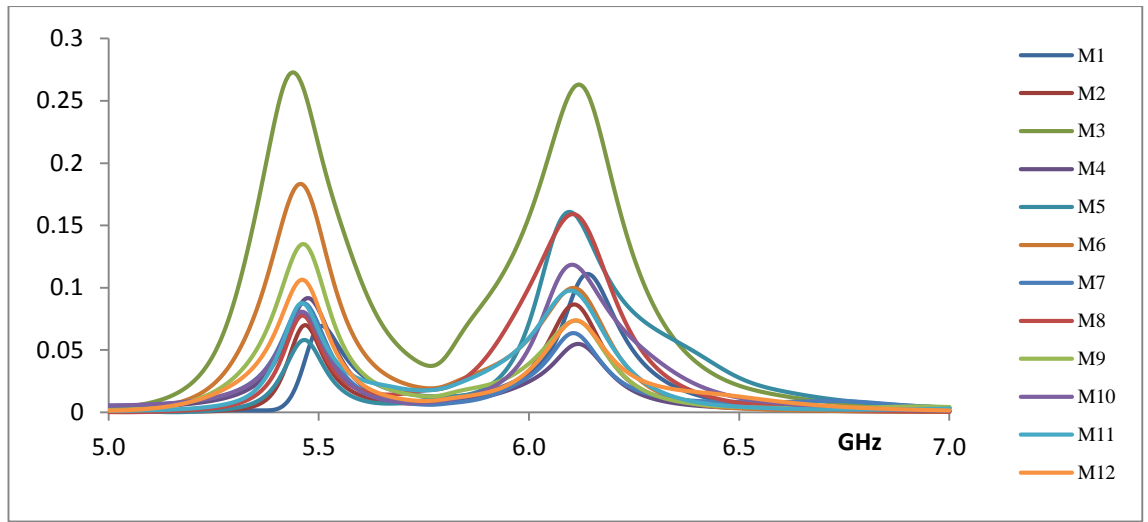
(b)

Figure 6-4 (a) Magnitude plot of T1-T3, 1cm-12cm (b) Magnitude plot of T2-T4, 1cm-12cm

6.4 Phase Analysis of the Simulation

The analysis of the signal is based mainly on the phase of the S-parameters. One of the main reasons for concentrating on the phase is that the propagation affects the amplitude of the signal in ways that are more difficult to quantify, whereas phase depends mostly on distance travelled and the antenna characteristics. The following section describes how the patch antenna phase information from S-parameter is used to analyse the reflections from reflection coefficient, S_{ii}. A brief overview of the analysis of the phase of a signal is described here.

According to [84], the general network representation of the input impedance for a patch antenna is as shown in Figure 6.5.
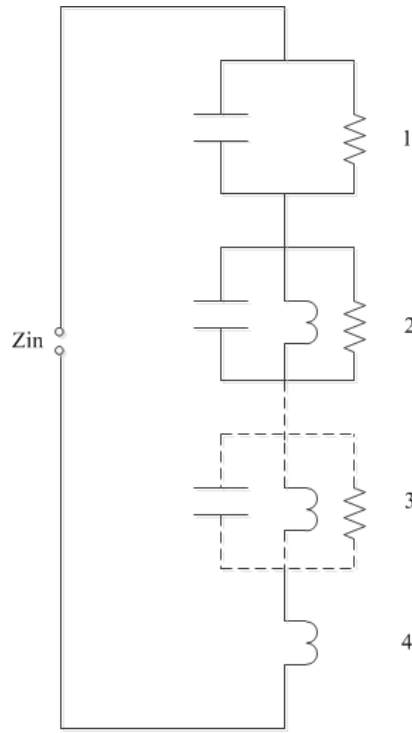
Figure 6-5 General network model representation of microstrip antenna [84]

The circuit section is categorised into four sections 1, 2, 3 and 4 respectively, where Z_{in} is the input impedance. The explanation for this circuit will be based on the frequency sweep between 10 MHz to 10 GHz, the frequency sweep used for this research. Section 1 represents the low frequency static capacitance of the patch and associated (very small) losses. Note there is no inductance. Sections 2 and 3 represent the resonant frequencies associated with modes 10 and 01. Section 4 represents the total inductance of all the higher modes. For these modes, the effects of resistance and capacitance are negligible in the 5-7 GHz range.
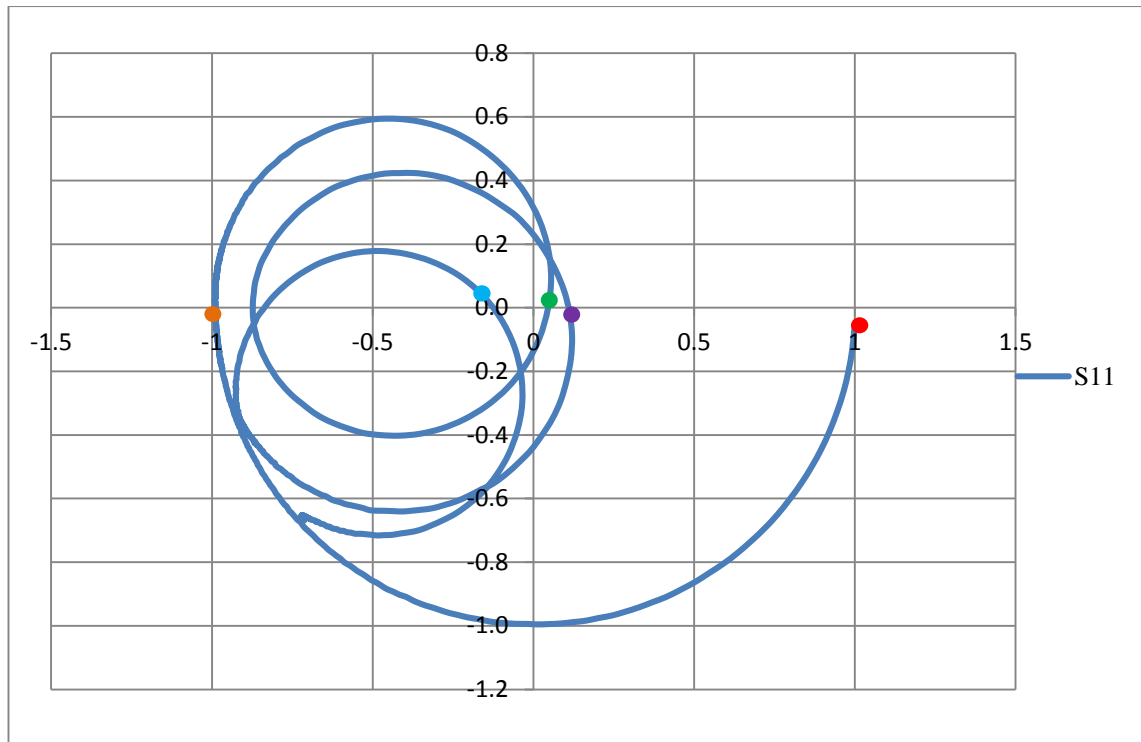
Figure 6-6 Polar plot of return loss in an antenna, 10 MHz-10 GHz.

At low frequencies the reflection coefficient curve on a polar plot starts just below the (1,0) point marked as a red dot in Figure 6.6. The patch antenna behave like a static capacitor and the curve follows a semi-circle around to near the (-1, 0) point. For a large range of low frequencies the reflection coefficient is negative and its value is near to −1 with a phase angle of -180°. The value of S11 is very close to -1 (orange) which shows that most of the input signal is reflected back with a 180° phase change.

As the frequency increases and nears the lowest resonant frequency, circuit section 2 will be dominant. The inductive and the capacitive currents cancel out and conduction will be only through the resistor. This is exactly the behaviour of a RLC circuit. The dominant mode will be (1, 0) for section 2 in Figure 6.5. At the resonance, in Figure 6.6 there is a phase shift of 360°. This is the point where the minimum reflection takes place (marked with a green dot) and the curve takes a full circle near to the origin. For the dominant mode (0, 1) at second resonant frequency, the circuit 3 will be dominant and in Figure 6.6 the phase changes by another 360° for the second resonance, the purple

dot. The conduction of current will be through the capacitors in circuits 1 and 2 and through the resistor in circuit 3 and inductor at 4. As the frequency is increased beyond this resonant frequency, the impedance will be inductive due to the higher order modes in the patch. The conduction will be through the capacitors in circuit sections 1 to 3. Mode (1, 1) resonance near 9 GHz causes the reflection coefficient polar plot to go through another 360° rotation as shown by blue dot in Figure 6.6.

Figure 6.7 shows the phase angle behaviour for reflection coefficient for the above explanation. The unwrapped plot in degrees is shown in Figure 6.7 for a dual band antenna. Unwrapping of phase means whenever the phase of the S-parameter jumps from -180° to $+180^o$ then 360 is subtracted from the phase to make the phase graph a continuous line.
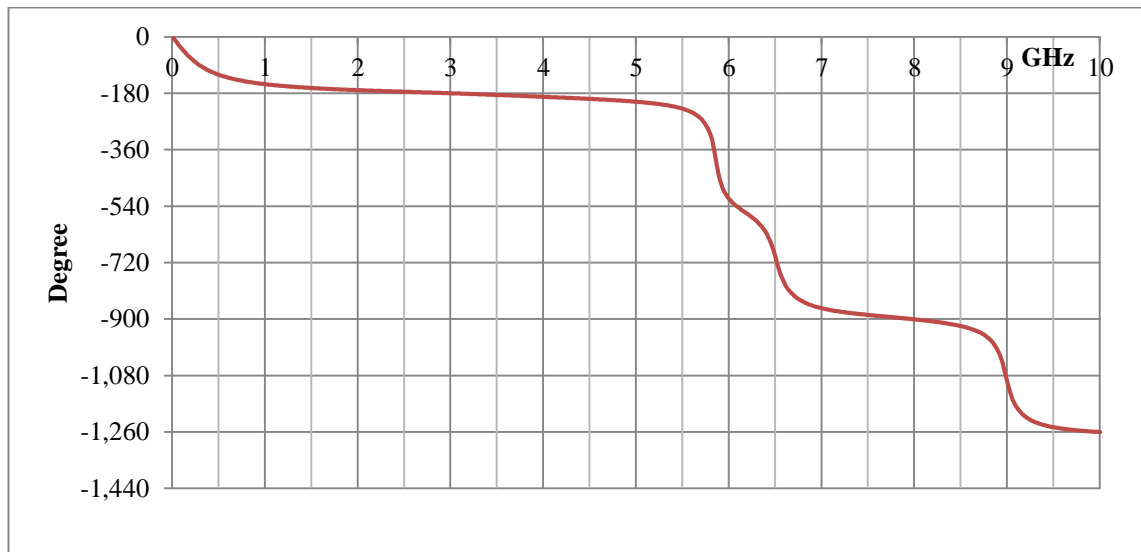
Figure 6-7 Phase angle plot for the designed dual-band patch antenna.

At low frequencies the magnitude of S_{11} is almost one and most of the signal will be reflected. As the input frequency reaches resonant frequency of 5.75 GHz, the phase angle has a 360° phase change, and at the second resonance near 6.5 GHz another 360° phase change occurs. When the input frequencies increased beyond the second

resonance frequency, the phase angle is approximately -900° it reaches the higher order resonance near 9 GHz.

In Figure 6.8 (a) when a signal is applied to antenna T1 or T2, the signal travels through air, hits the object and some of the signal is reflected back to the transmitting antenna.
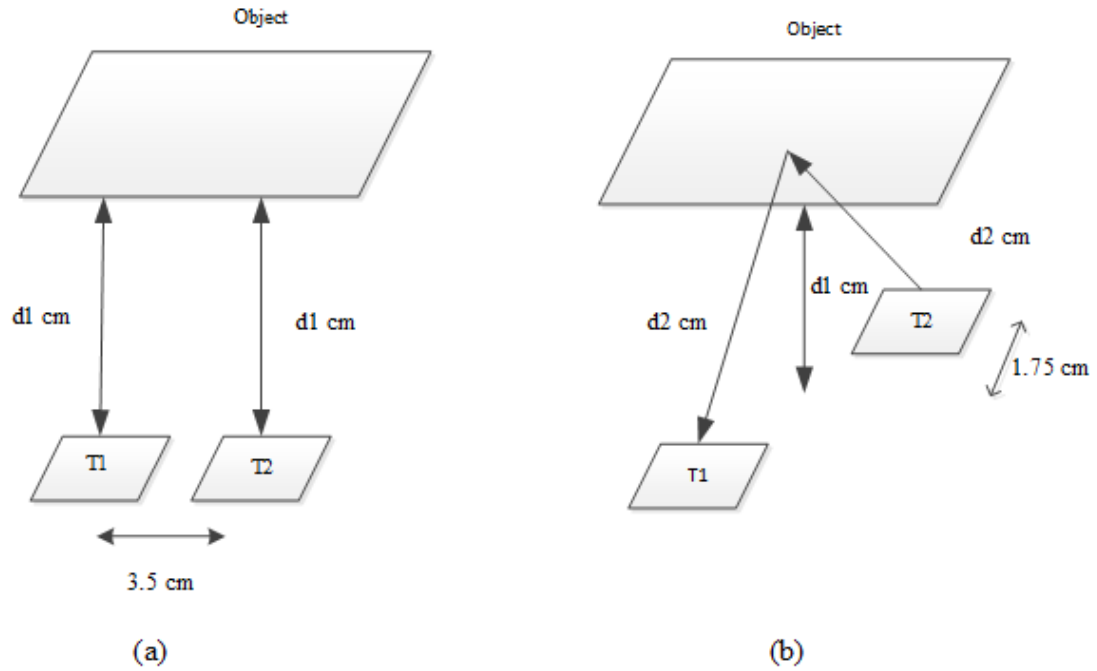
Figure 6-8 (a) Transmission and reflection of wave to same antenna (b) Transmission and reflection of wave to diagonal antennas.

The total distance travelled by the wave will be:

$$d = 2d1 \hspace{3cm} 6.2$$

The ideal phase angle variation for distance travelled for the setup shown in Figure 6.8 (a) is plotted in Figure 6.9 for the frequency range from 5.3 GHz to 6.7 GHz. The numbers shown in the legend represent variation of distance in centimetre from the antenna array to the reflector.
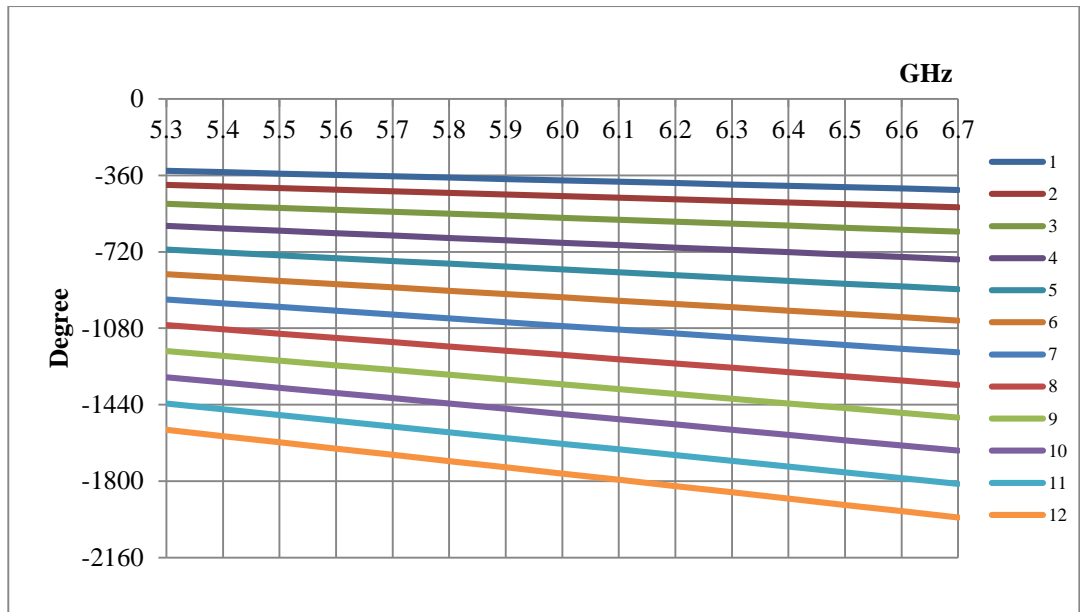
Figure 6-9 Phase angle variation for signal receiving at the same terminal for reflector distance in centimetre.

Similarly when the antenna elements are diagonally opposite as in Figure 6.8 (b) the total distance travelled by the wave will be:

$$d = 2d2 \qquad\qquad 6.3$$

Where $d2 = \sqrt{1.75^2 + d1^2}$

The variation of phase angle versus frequency is plotted in Figure 6.10
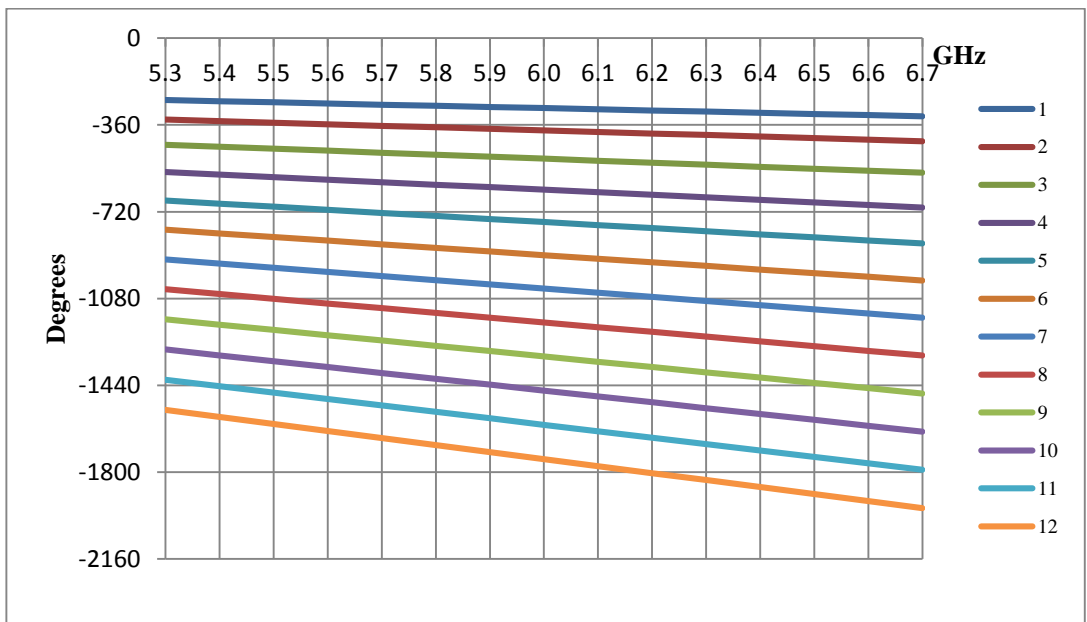

Figure 6-10 Phase angle variation for signal receiving on diagonal antenna element for reflector distance in centimetre.

The data for the Figure 6.9 and Figure 6.10 were obtained based on the following, for example at 6 GHz wavelength λ= 5 cm and for an object at 5 cm the total distance D travelled for Figure 6.8 (a) is 10 cm and for Figure 6.8 (b) is 10.59 cm. So the phase in degrees of the wave at 6 GHz is:

$$\frac{Distance\ travelled\ (D)}{\lambda} \times 360 \qquad\qquad 6.4$$

From the simulation, the S-parameters are exported and the phase of the signal is extracted from the S-parameter after subtracting the coupling effect. The metal is moved through distances 1 cm to 12 cm from the antenna array. Thirteen S-parameter data files are obtained, 12 for the metal reflector and 1 data file when freely radiating to space. The S-parameters $S_{11}, S_{33}, S_{13}, S_{31}, S_{22}, S_{44}, S_{24}$, and S_{42} are analysed. The other S-parameters have very low magnitude and can be disregarded.   The respective unwrapped phase is plotted for decoupled data as shown in Figure 6.11. The phase variations for 1-12 cm for reflected signal at transmitting antenna *T1, T2* and S-parameter S_{13} and S_{24} are plotted since they provide the major information about the reflection. The legend in the plot shows the reflection coefficient and letter *M* corresponding to metal and the numbers following shows the step size in centimetres. The *X*-axis is frequency in GHz and *Y*-axis is phase in degrees.
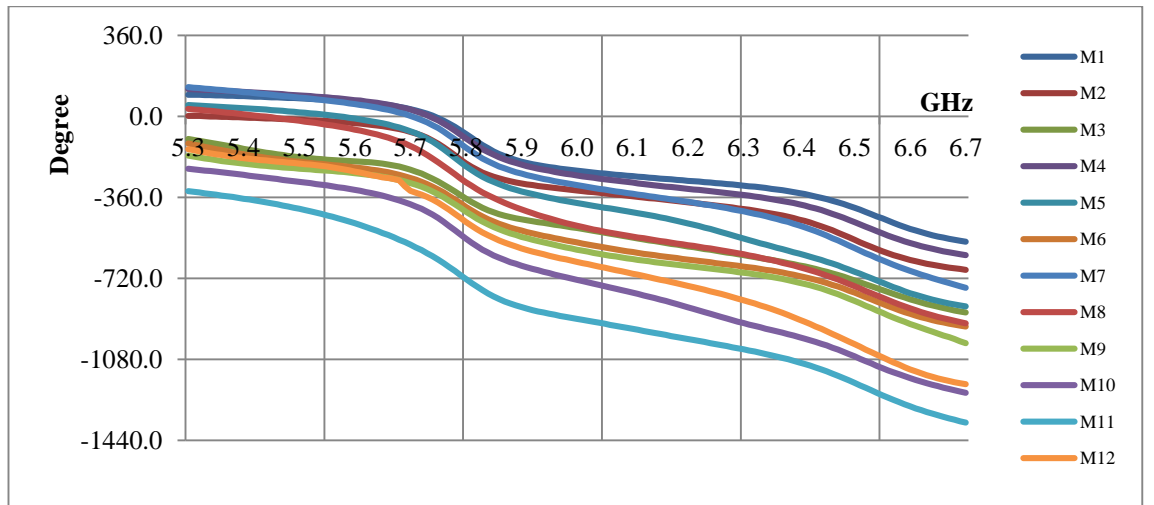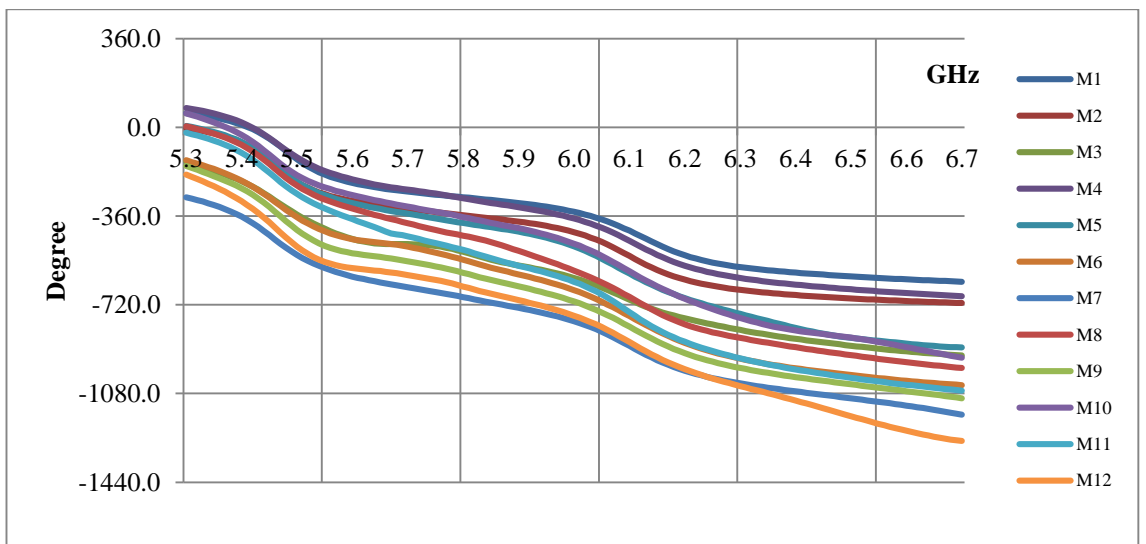

(a)
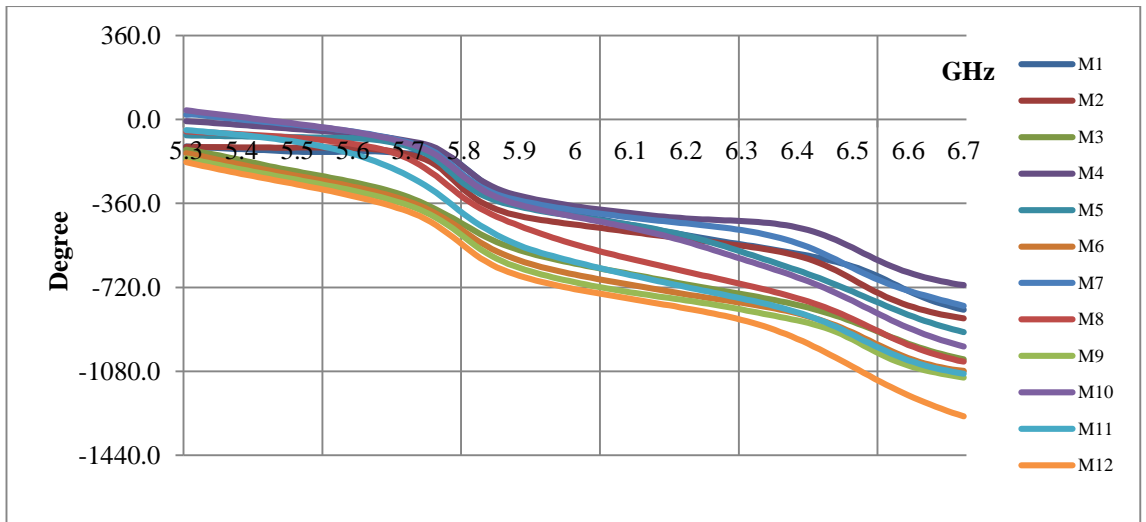
(b)
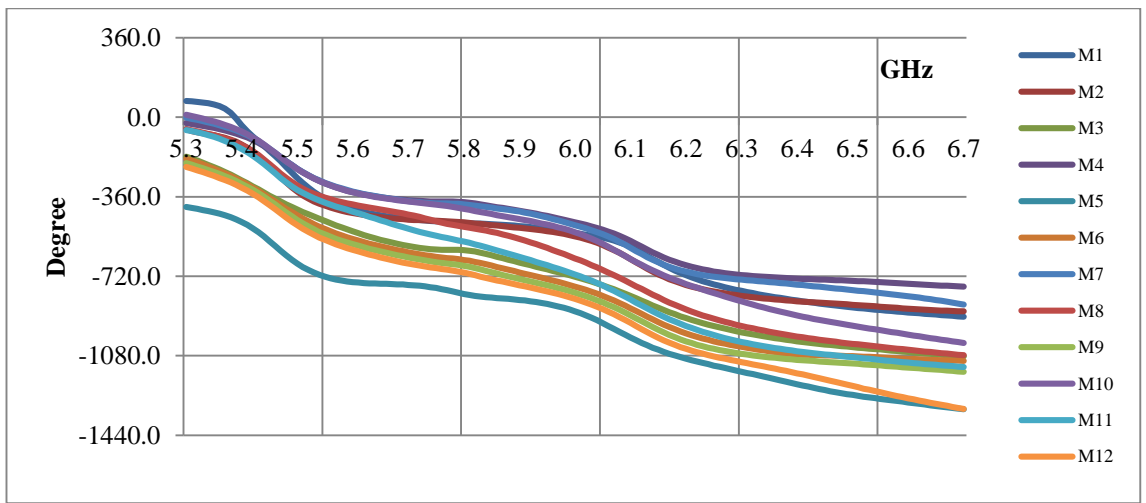
(c)

(d)

Figure 6-11 Unwrapped phase plot for antenna elements with metal reflector in simulation, 1cm-12cm for (a) T1 (b) S13 (c) S24 (d) T2.

The variation of phase angles compared with Figure 6.9 for reflection to the transmitter and Figure 6.10 for transmission to the receiver does not agree with Figure 6.11. The phase angle plot in Figure 6.11 needs further compensation so that it follows a pattern which can distinguish the various reflection distances.

First the phase angle can be compensated by adding multiples of 360° so that longer distances have more negative phase angles.

Figure 6.12 (a)-(d) shows the compensated phase angle plot for the simulation model which follows a pattern in which phase of the angle increases as the distance between antenna and metal increased from 1 cm to 12 cm.
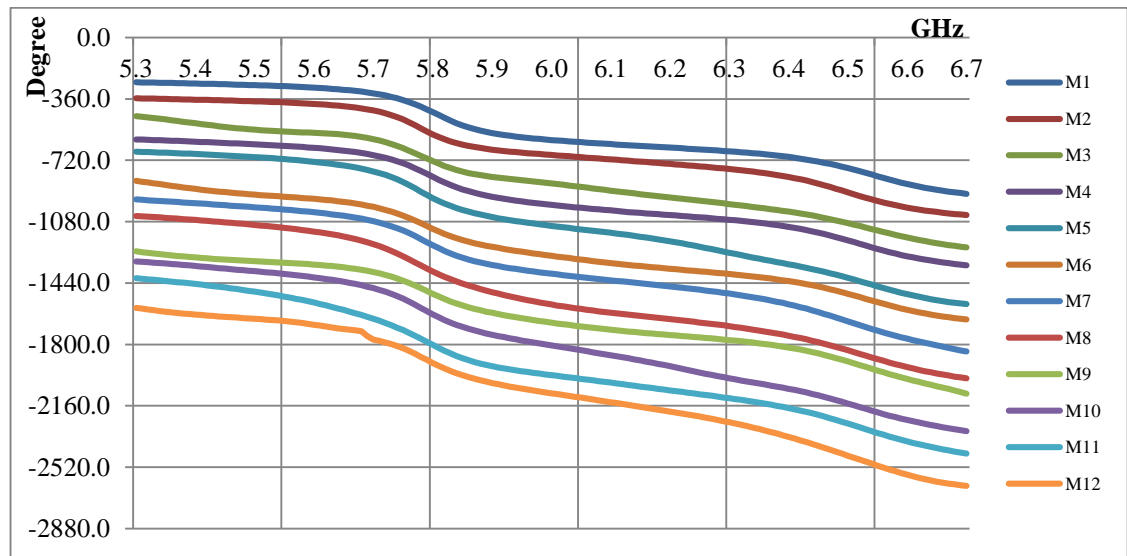
(a)
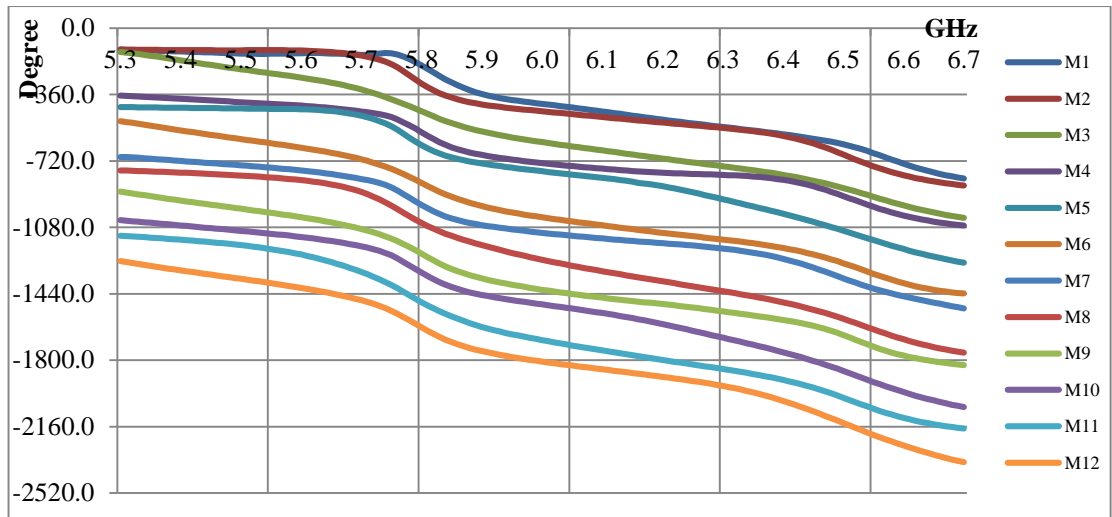
(b)

(c)

(d)

Figure 6-12 (a)-(d), Corrected phase angle plot for simulation results (a) T1 (b) S13 (c) S24 (d) T2.

Comparing the graphs in Figure 6.12 it clearly suggest that the reflections received at *T1, T2* provide better phase angle for objects that are p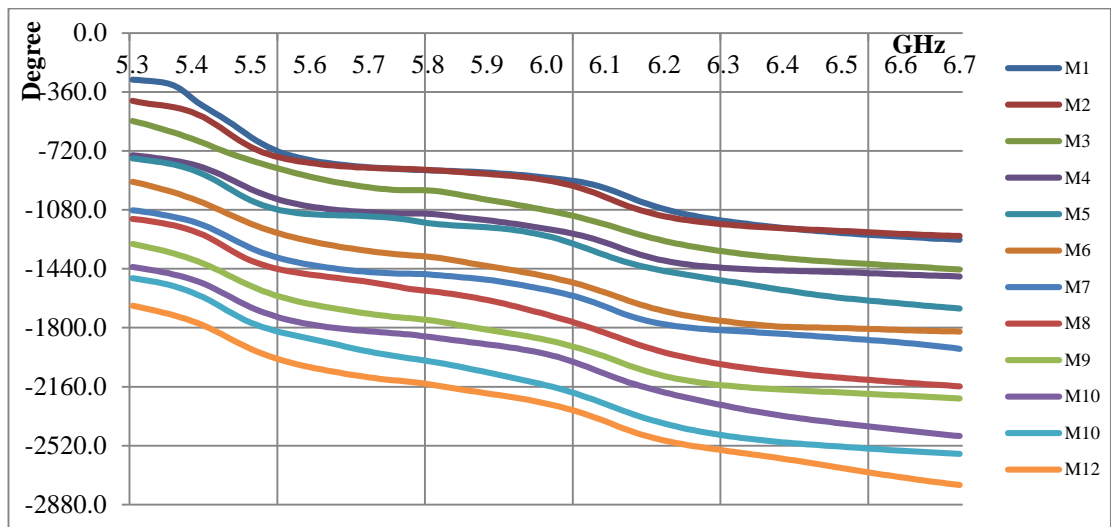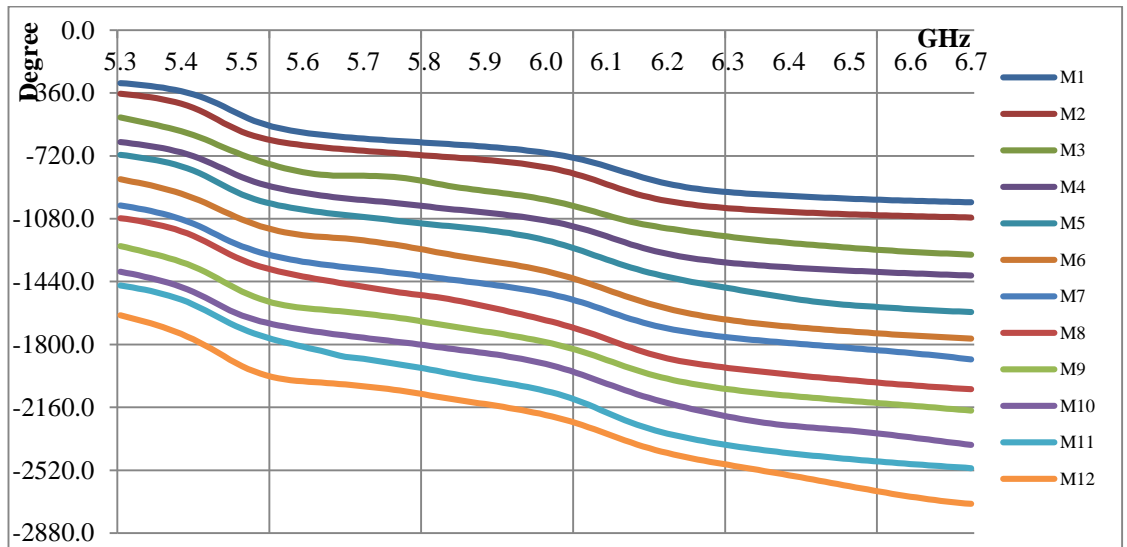arallel to the antenna surface. It clearly distinguishes the distance between each step size compared to the transmission coefficient (S_{13}, S_{24}) where the initial step sizes are overlapping with each other. This needs to be verified experimentally and the next section will cover the experimental model.

6.5 Summary

Chapter 6 describes the reflection analysis of the object as it is moved away from the antenna surface. The phase is analysed to obtain the relation between the distances travelled as the object is moved from the surface. The analysis is based on simulation results for the S-parameters. From the simulation results, it is found that the distance variation from the reflection based on the phase angle can be obtained after compensating. In the next chapter the analysis is performed on the experimental results to verify the simulation analysis.

Chapter 7 Analysis of Experimental Reflection Results

The antenna array and reflector are mounted vertically on two custom built holders similar to the one described in Section 5.1. The antenna array holder is fixed and the reflector holder is moved away from it. A linear scale marked in mm shows the distance from the fixed antenna array to the reflector. The holders are made so that they are centrally aligned. Both the holders are clamped vertically. The antenna array and the metal plate can easily slide through the grooves of the holder. Wooden sticks are placed through the holes inside the holder so that it can be aligned properly. The arrangement is as shown in Figure 7.1.
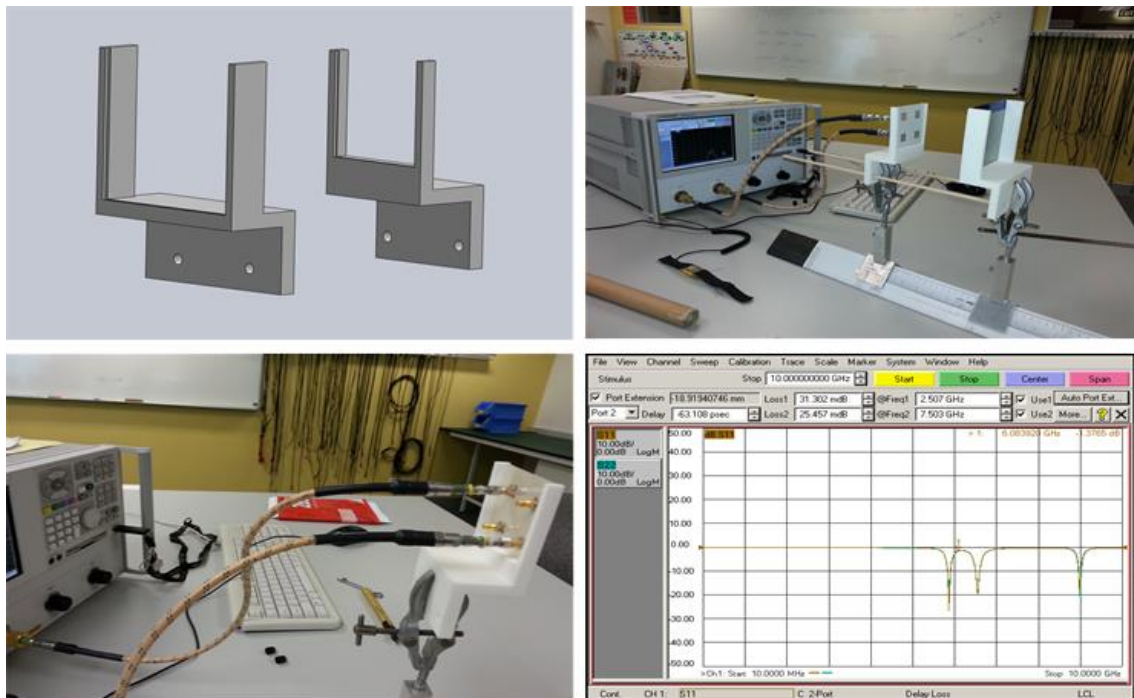
Figure 7-1 Experimental setup for antenna array measurement.

The antenna array measurement for reflection measurement is conducted as follows. The setup is similar to the one used for antenna measurement when freely radiating as in Section 5.2. *T1* is connected to port 1 of the NA and port 2 is connected to *T2*, *T3* and *T4* to obtain the respective antenna terminal measurements. The set of measurements taken are between *T1-T2*, *T1-T3* and *T1-T4*. Then *T2* is connected to port 1 and port 2 is connected with the other terminals for their respective antenna element

measurements, *T2-T3*, *T2-T4*, and finally the ports are connected to take the measurements for *T3-T4*. These measurements are repeated with metal in front of the antenna and the distance varied from 1cm to 12 cm respectively. Measurements are conducted for the other three antenna arrays.

7.1 Calibration for Extra Phase in the Measurement

When the NA is calibrated as described in Section 5.2, the measurement plane is brought up to the end of the connectors in the NA that are used to connect the coaxial cable/SMA connector with the antenna array. So the effect of coaxial cable RG402 and the F-SMA soldered to antenna array will add additional phase to the measurement.

The expected graph for the phase angle variation of S_{nn} for the dual band patch antenna is shown in Figure 6.7. Figure 7.2 shows the actual variation of phase for reflection coefficient measurement for Patch1-SMA, Patch2-SMA and Patch3-RG. Only three plots are shown for understanding the effect of the extra phase added due to the coaxial cable/connectors. These are measured when freely radiating. As expected the Patch3-RG with the coaxial cable has a noticeable slope compared to the antenna with the SMA soldered onto the board. The slope is calculated for the phase at each terminal for the reflection coefficient and the phase angle delay/GHz is calculated based on the ideal phase angle variation as in Figure 6.7. This extra phase delay is subtracted from the original phase as in Figure 7.2 to obtain the calibrated phase angle variation as in Figure 7.3 (a)-(c).
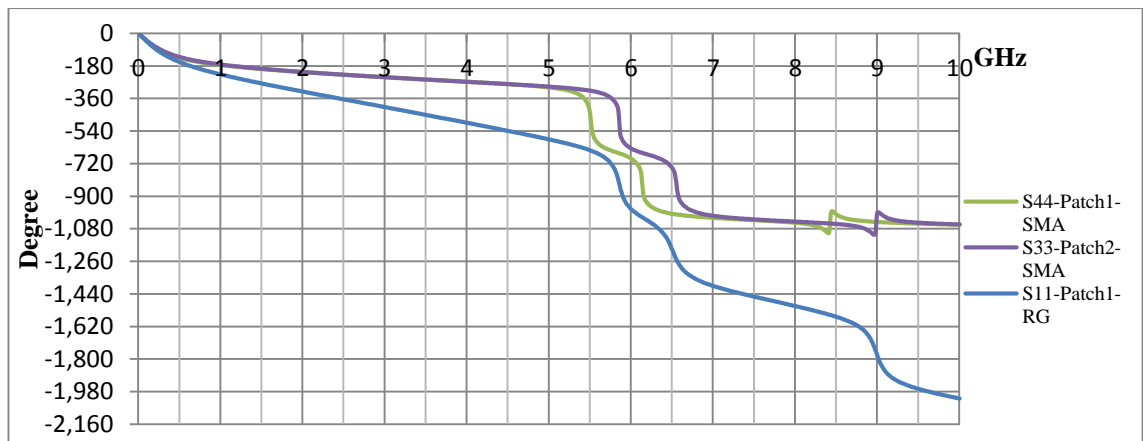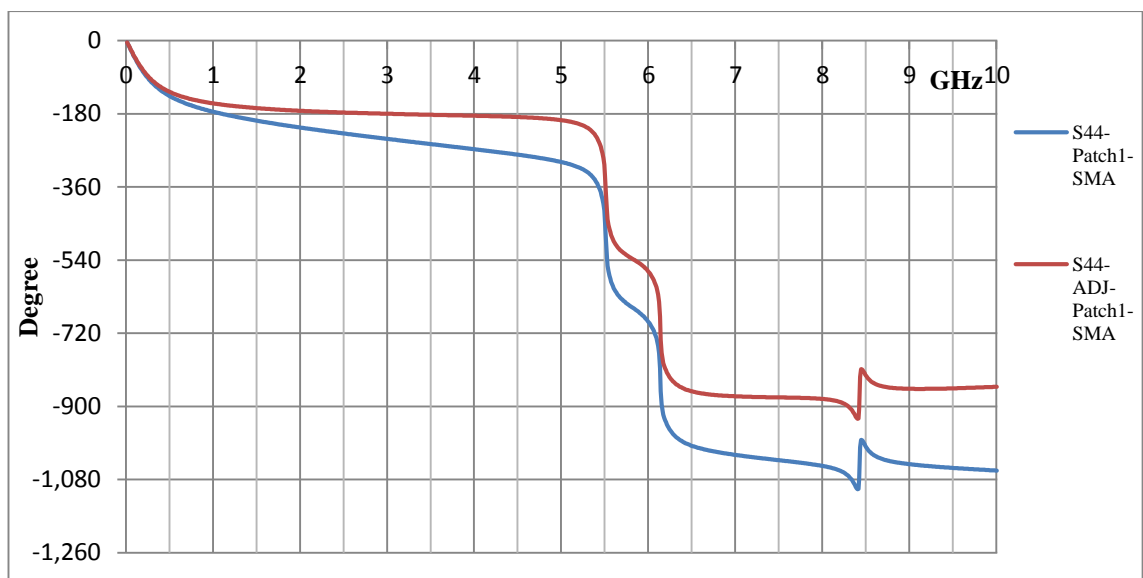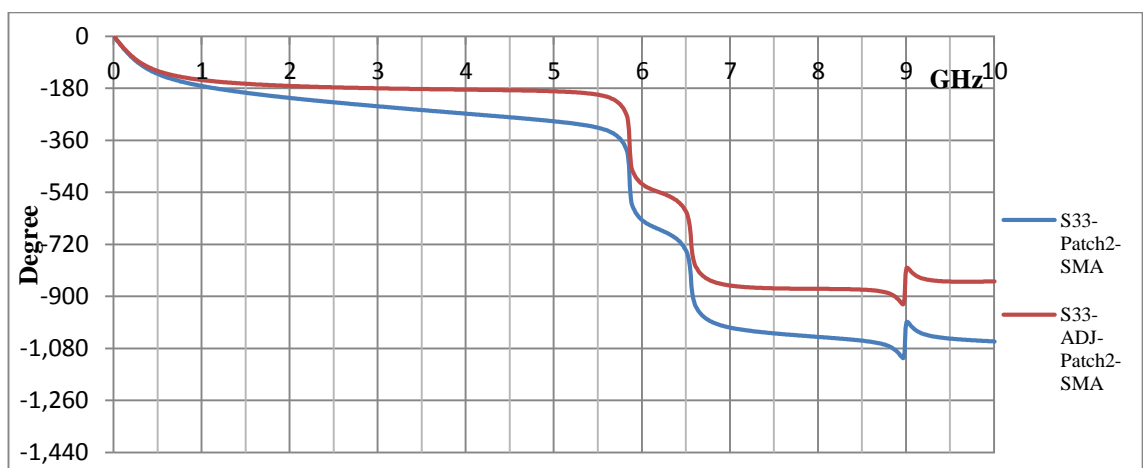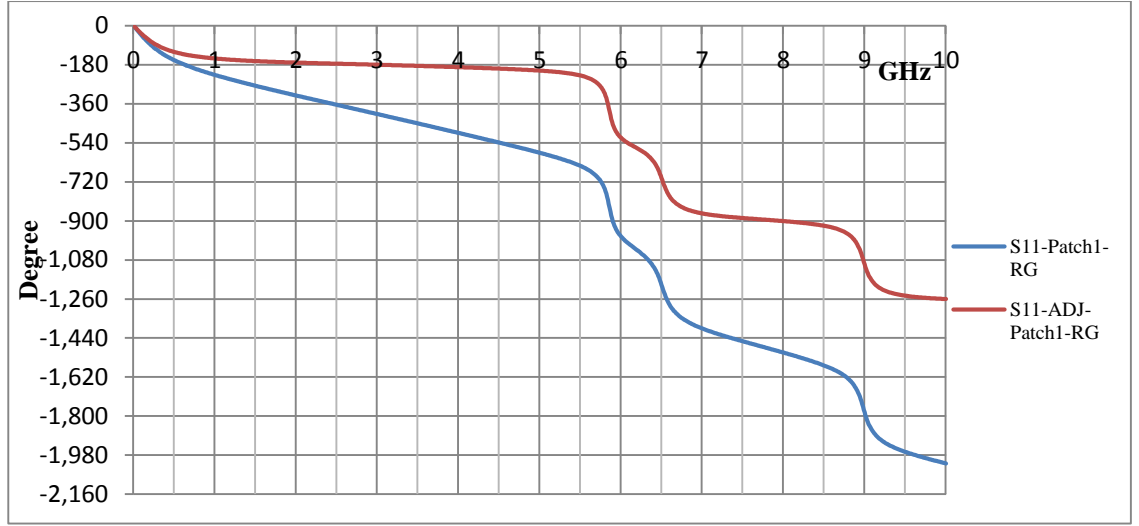
Figure 7-2 Phase angle variation in reflection coefficient measurement.

(a)

(b)

(c)

Figure 7-3 Calibrated phase plot for three antenna array build, (a) Patch1-SMA (b) Patch2-SMA (c) Patch1-RG.

This calibration is conducted for the entire terminal reflection coefficient and for all the antenna array measurements i.e. S_{11}, S_{33}, S_{22} and S_{44} to find the phase delay for each cable/connector associated with the each individual patch element. The S-parameter air measurement (without reflector) was subtracted from the S-parameter metal measurements (with the reflector) to remove the coupling effect and then the extra phase delay is removed.

Referring to Figure 6.8 (a), the extra phase delay at *T1* is denoted by 2α and at *T2* by 2β. These are the individual phase delays through each terminal. These phase delays can be calculated for S_{11}, S_{33}, S_{22} and S_{44} and subtracted from each terminal. Similarly when S_{13}, S_{31}, S_{24} and S_{42} are considered $(\alpha + \beta)$ is subtracted since the wave travels through *T1*, is reflected from the metal and the received on *T2*. Therefore the total calibration procedure for a reflection from the metal plate at 3 cm distance (for example) will be:

$$S_{11}M3_{cal} = S_{11}M3 - S_{11}Air - 2\alpha$$

$$S_{13}M3_{cal} = S_{13}M3 - S_{13}Air - (\alpha + \beta)$$

7.1

89

$$S_{33}M3_{cal} = S_{33}M3 - S_{33}Air - 2\beta$$

where $M3$ denotes the metal reflector at 3 cm and , Air denotes the S parameter when freely radiating in air. The same procedure is applied for other antenna terminals and on each antenna array.

7.2 Magnitude Analysis

The magnitude of the reflections received at the terminals *T1-T3* and *T2-T4* are also obtained from the experiment. This magnitude is refined by removing the mutual coupling. The measurements when freely radiating in space are subtracted from each reflection measurements. The magnitude plot for each antenna array as the distance varied from 1-12 cm is shown in Figure 7.4 (a)-(d). Only S_{13} and S_{24} are shown as in Figure 6.4, S_{13} on the right and S_{24} on the left of each plot. The X-axis is frequency in GHz and the Y-axis is the magnitude and the legend for the plot is shown at the bottom of the figure.

(a)
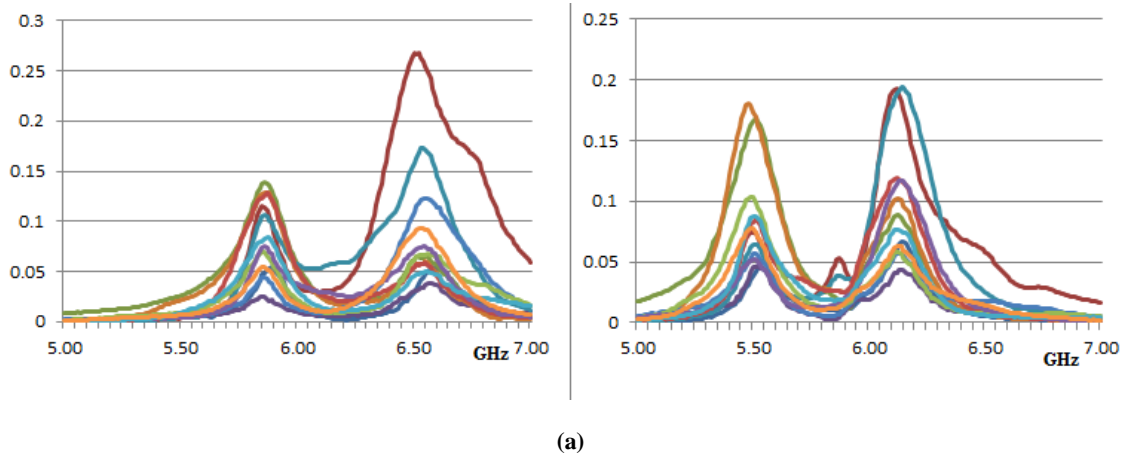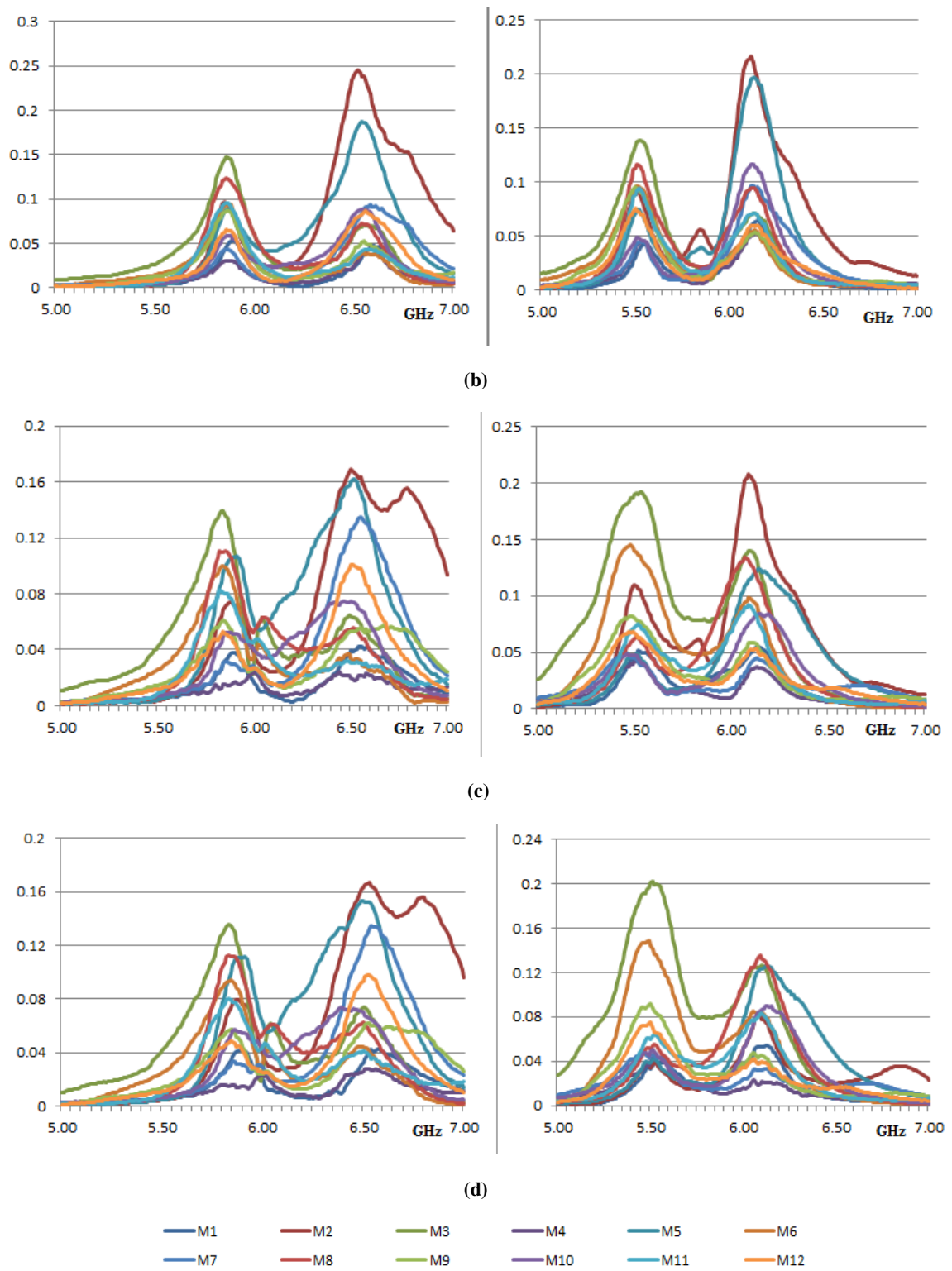
Figure 7-4 Magnitude plot of S13 and S24 for reflections from 1cm-12cm (a) Patch1-SMA (b) Patch2-SMA (c) Patch3-SMA (d) Patch4-SMA.

The magnitude plots of the reflections received by the antenna elements suggest that the antenna array, Patch1-SMA and Patch2-SMA have good reception compared to the other patch antenna arrays.

7.3 Phase Analysis on Experimental Results

An overview of how the phase is used to categorise the reflection at various distance is described in the simulation analysis of reflections in Section 6.4. The measurements are taken for all four antenna arrays and the phase angle is extracted from the complex S-parameters after removing the coupling as well as phase delay using Equation 7.1. The phase angle variations for 1-12 cm for S-parameters are considered here. All the significant S-parameters are considered: $S_{13}, S_{31}, S_{24}, S_{42}$ and the reflected signals received at the transmitter antennas T1, T2, T3 and T4. Since the manufactured antenna array with SMA soldered to the ground plane gave good results, those antenna array models Patch1-SMA and Patch2-SMA are analysed here. Figure 7.5 shows the phase angle variation of S-parameter for Patch1-SMA.

(a)

(b)

(c)

(d)

(e)

(f)

(g)

94
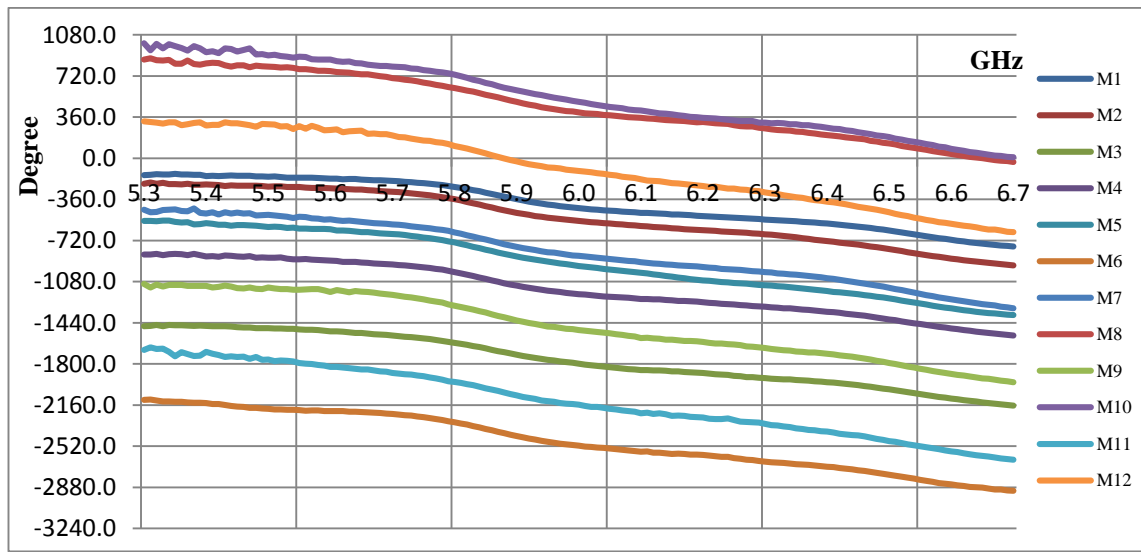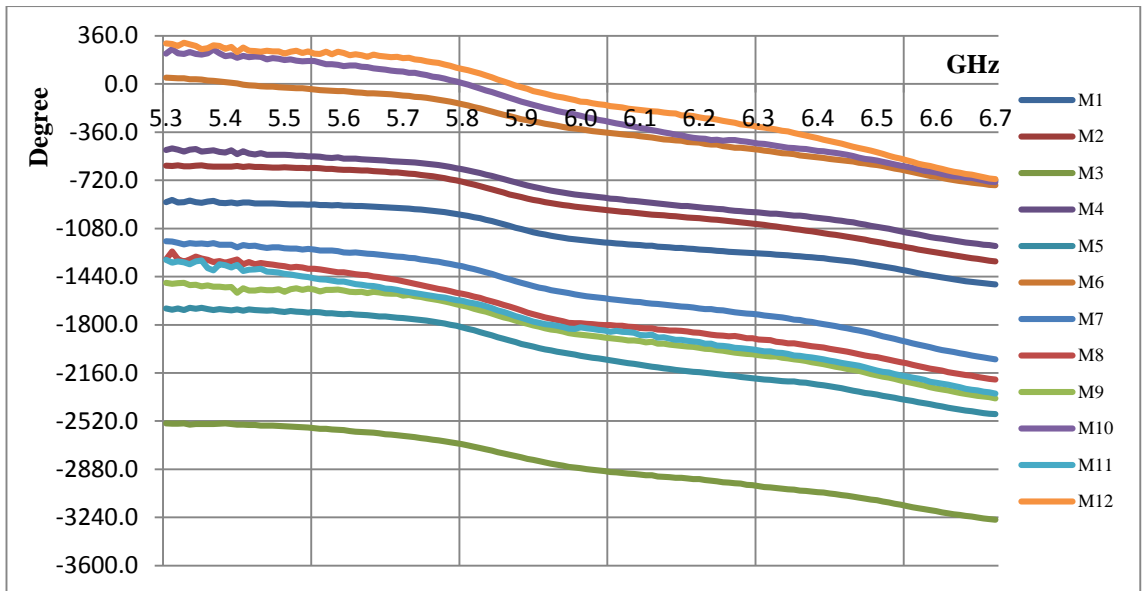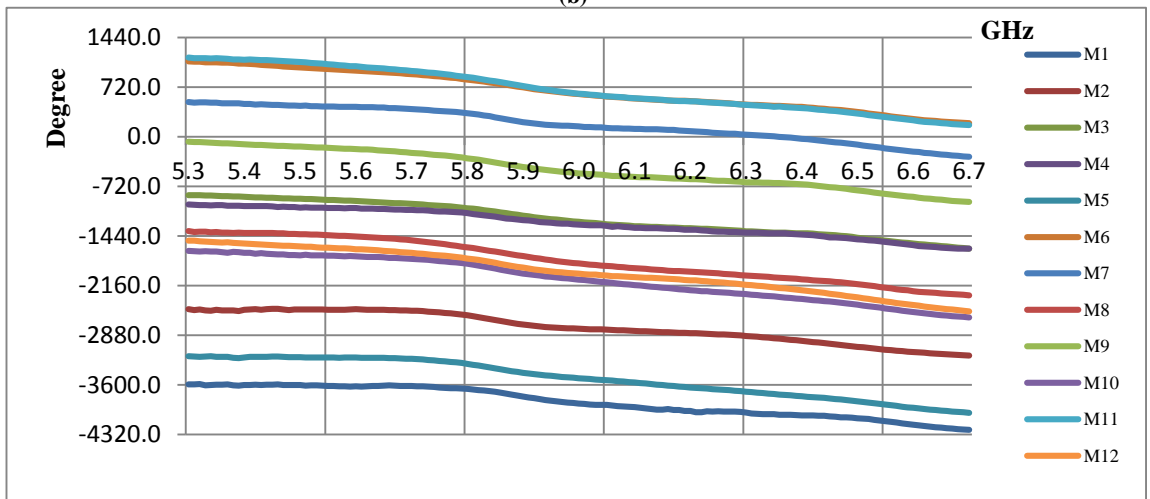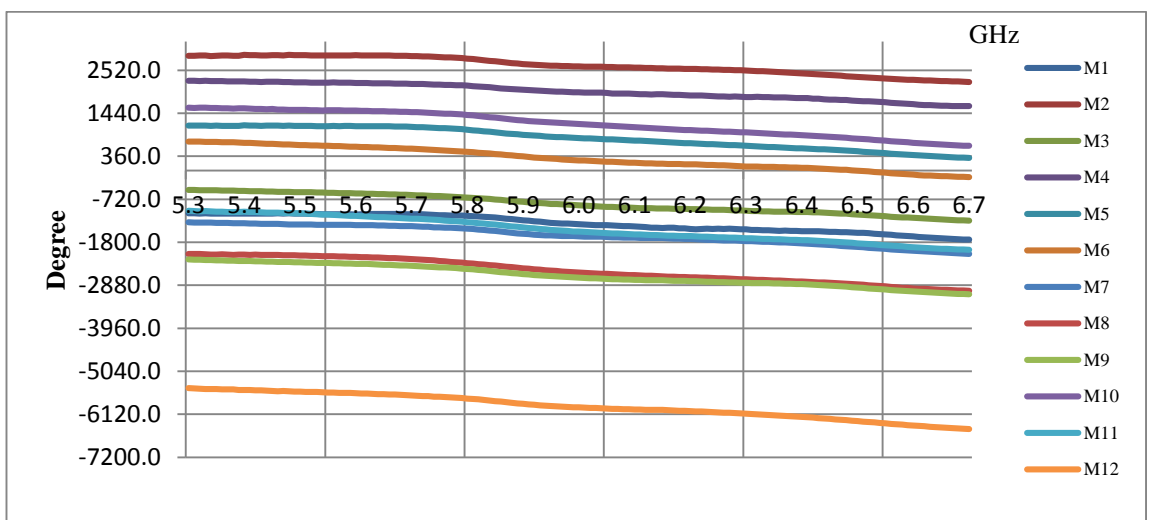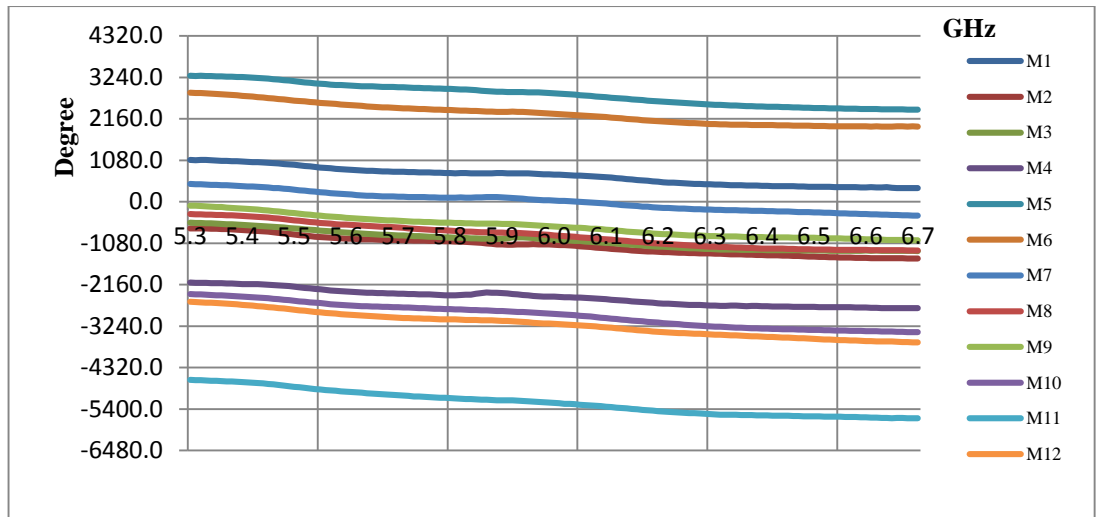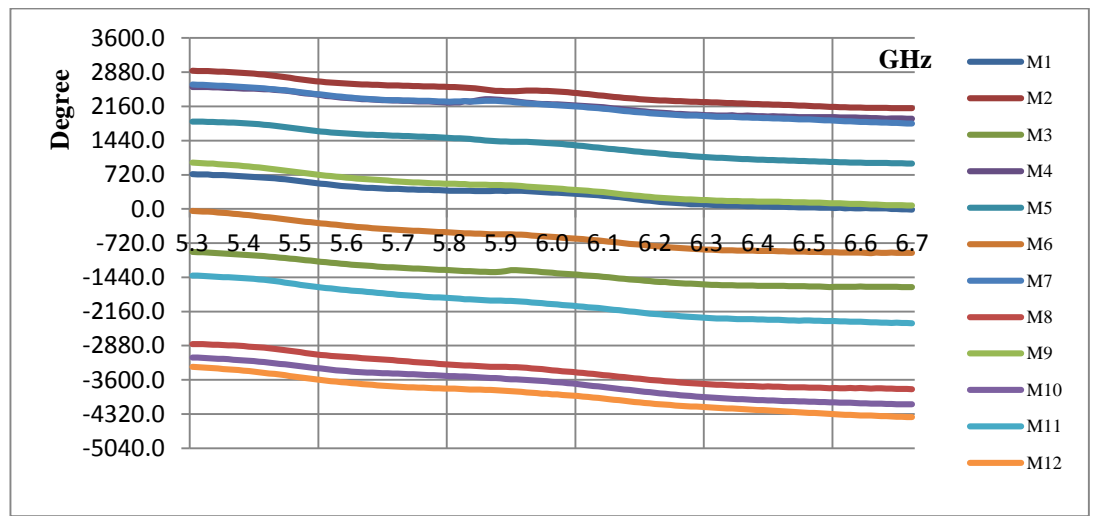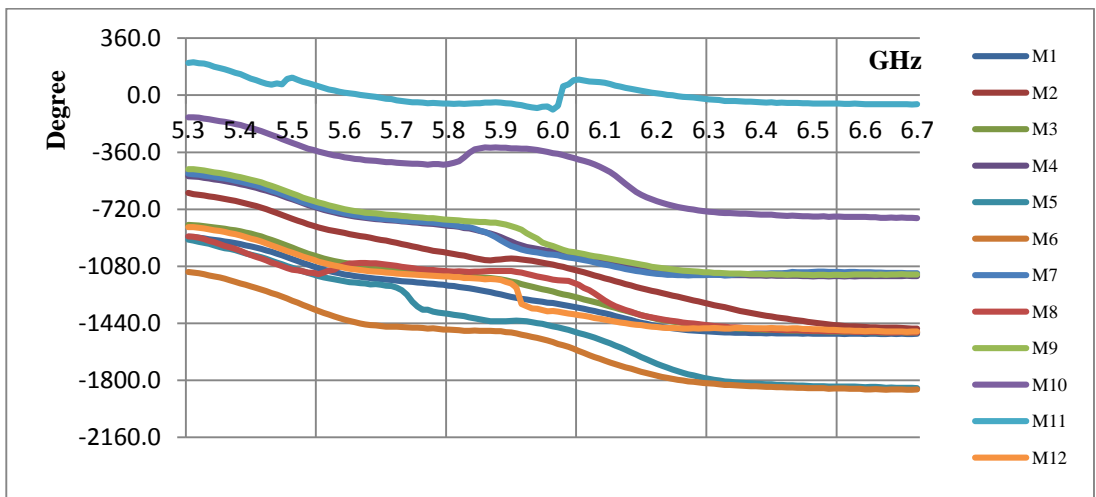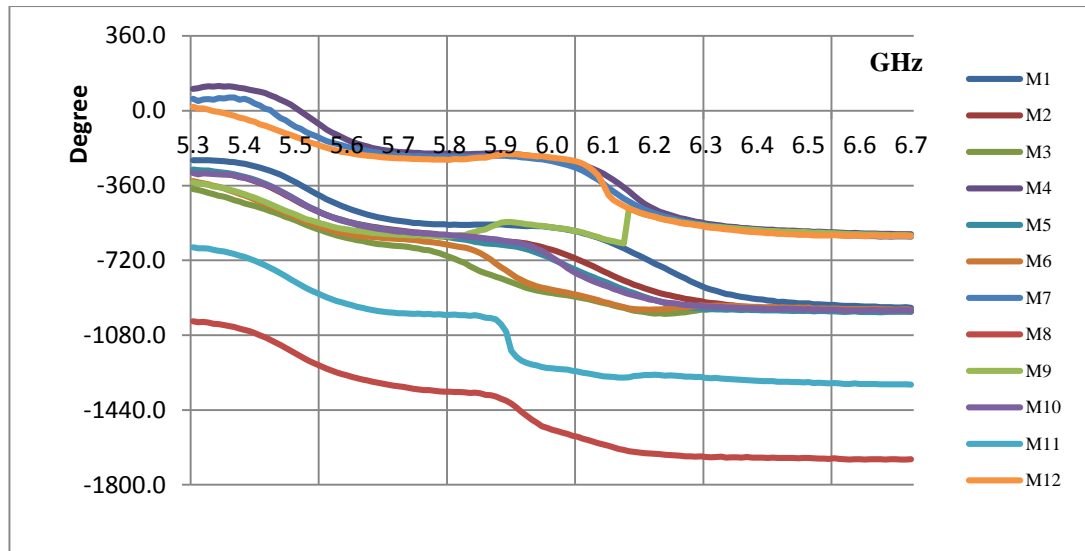
(h)

Figure 7-5 The phase angle of reflection back to the transmitter and receiver patch for Patch1-SMA antenna array (a) T1 (b) T3 (c) S31 (d) S13 (e) S24 (f) S42 (g) T2 (h) T4

From the Figure 7.5, distances from the reflected object cannot be distinguished based on the phase angle so compensation is applied on the phase angle in multiples of 360° to straighten up the phase angles. Figure 7.6 shows the compensated phase angle of S-parameter for Patch1-SMA antenna array.

(a)

(b)

(c)

(d)

96

(d)

(e)

(f)

97
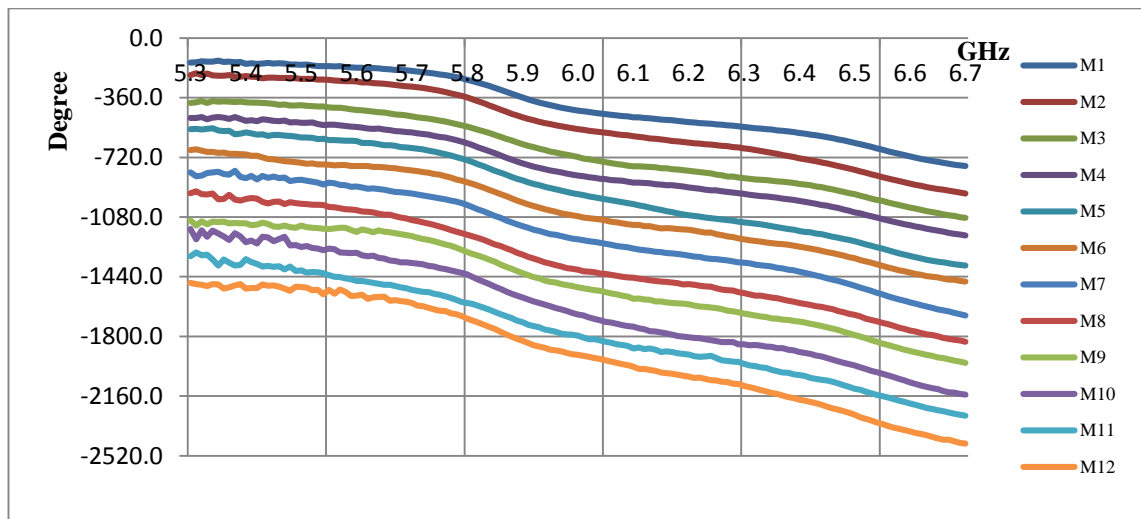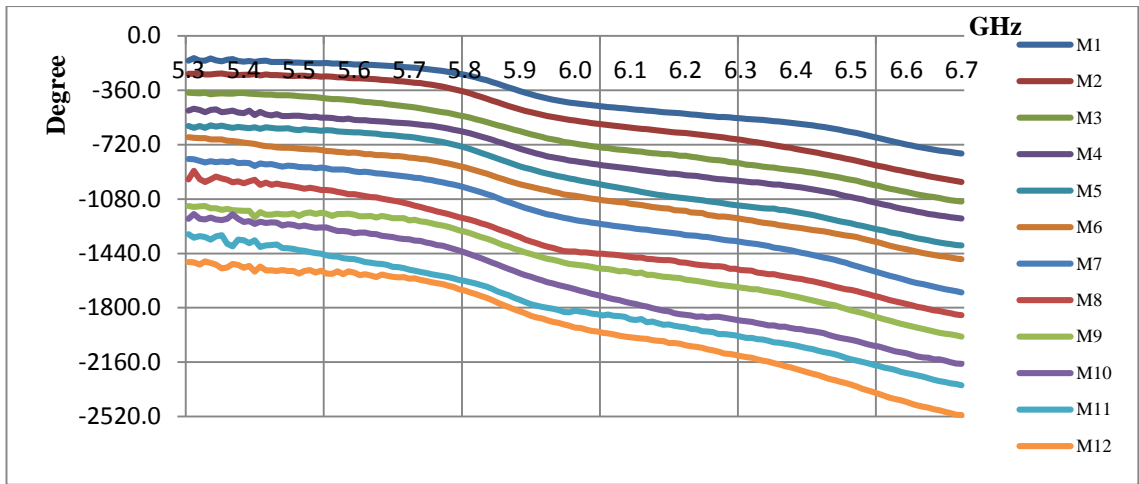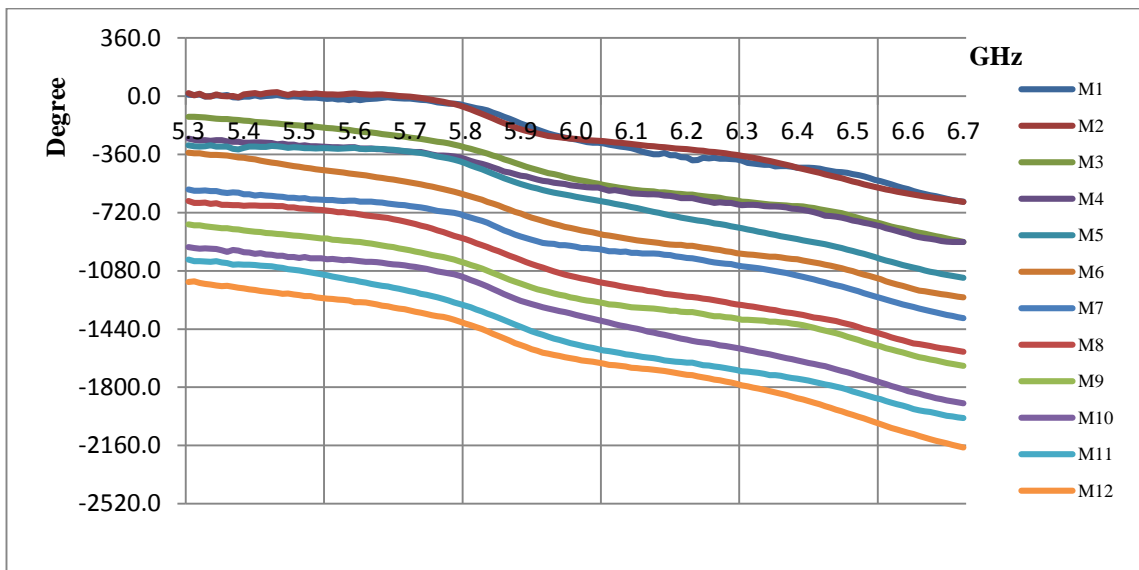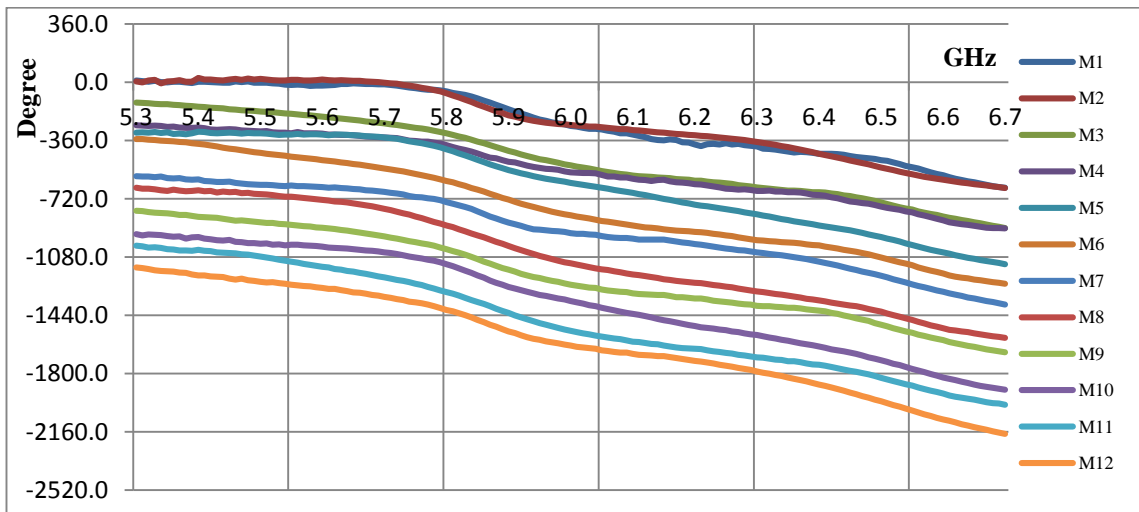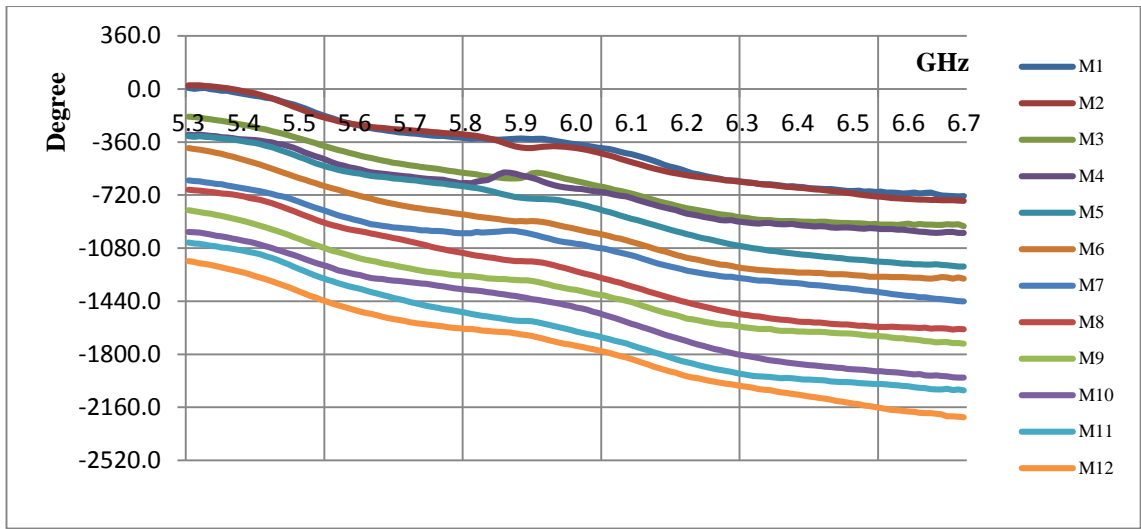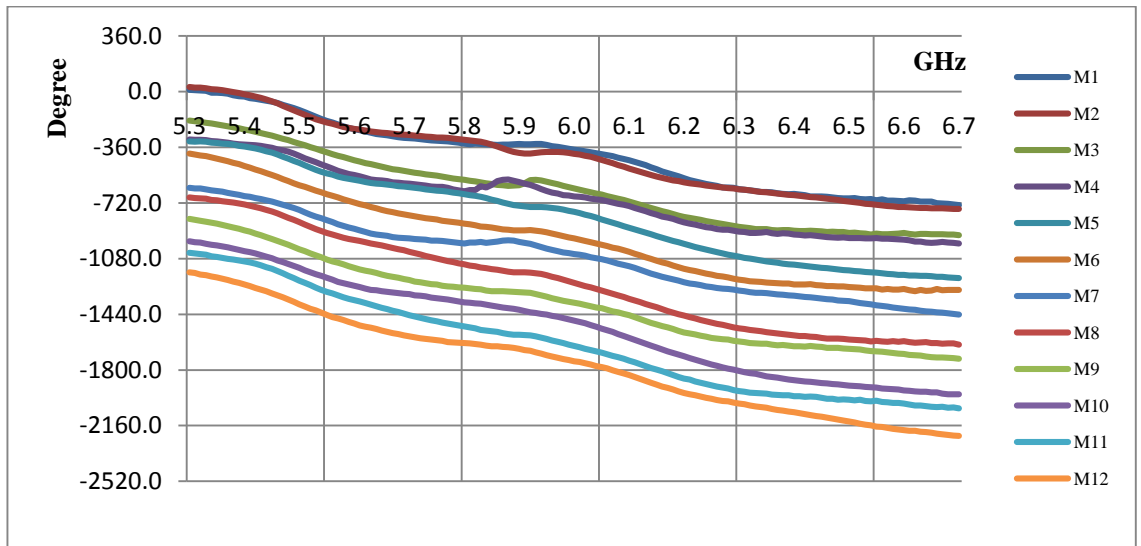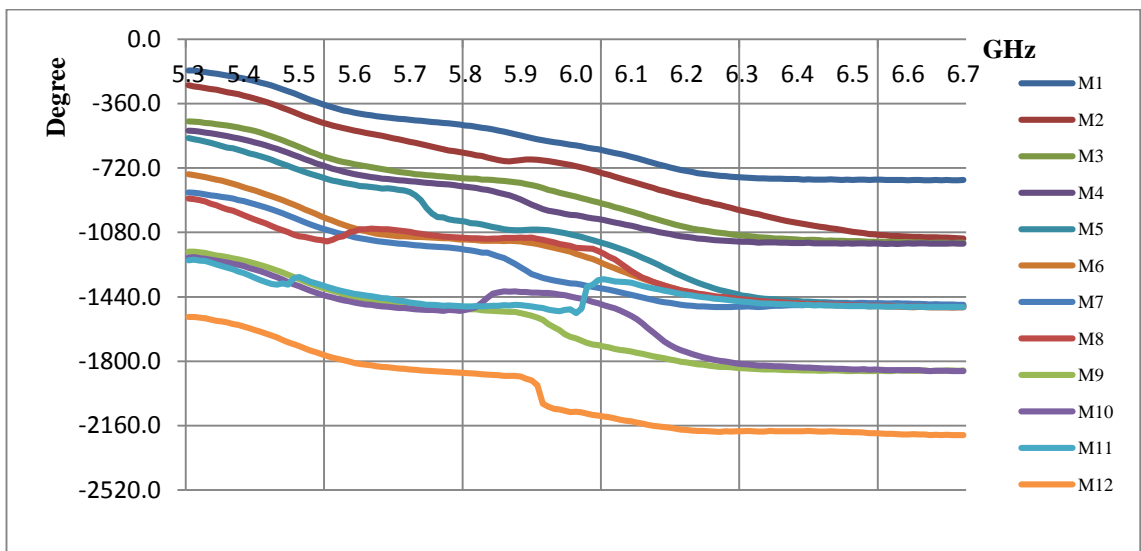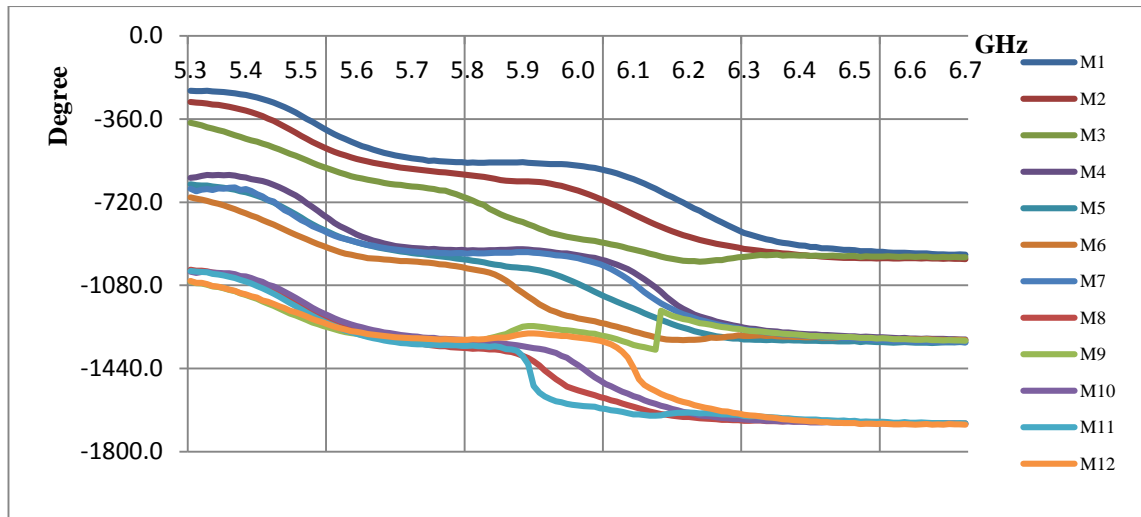
(h)

Figure 7-6 The compensated phase angle of reflection back to the transmitter and receiver patch for Patch1-SMA antenna array (a) T1 (b) T3 (c) S31 (d) S13 (e) S24 (f) S42 (g) T2 (h) T4

From Figure 7.6 it can be seen that the compensated phase angles of reflection coefficients as well as transmission coefficients has similar characteristics as explained before in Section 6.4. It can be noted that the phase angle pattern from reflection coefficient provides good separation of phase angle between the measurement distances. While for the transmission coefficient phase angles (measurements taken close to the reflector) have overlapping phase angles. For some measurements it can be observed that the phase angles have random jumps. These jumps are caused due to the curve traced by the phase angle (refer Figure 6.6) not completing a full 360° around the origin.

7.4 Summary

Chapter 7 describes a method to use the reflection measurements to calculate the phase angle due to the signal propagation distance. Also this chapter describe calibration procedure that was applied to correct the phase delay in the measurements. The next chapter, Chapter 8, describes a method which can be used to analyse reflection measurements from flat surfaces, based on signal propagation from the transmitter to the receiving antenna.

Chapter 8 Experimental Analysis Methodology

This chapter formulates the methodology that can be applied on experimental results to find an effective way to estimate the received signals at receiving antennas, which can then be used to find the reflection coefficient. Least Squares Method (LSM) was used for the data fitting. The theory is based on the references [19, 24, 84] which were covered in Sections 2.2, 2.3, 2.5.1 and 6.4.

8.1 Detailed Explanation on Methodology

The complex S_{11} from the experimental data (S-parameters) was used to calculate the input impedance of the antenna (Equation 5.1). The input impedance model (Z_{in}) assumes there are two modes in the patch antenna element, and is based on the general network model of a microstrip antenna described in Section 6.4.

$$Z_{in} = \frac{R_1}{1 + jQ_1\left(\frac{\omega}{\omega_1} - \frac{\omega_1}{\omega}\right)} + \frac{R_2}{1 + jQ_2\left(\frac{\omega}{\omega_2} - \frac{\omega_2}{\omega}\right)} \qquad 8.1$$

R_1 and R_2 are the resistance, Q_1 and Q_2 are quality factor and ω_1 and ω_2 are the angular frequencies for two modes in the network model shown in Figure 6.5.

In Equation 8.1 the first term models the *10* mode and the second term models the *01* mode. These modes correspond to sections 2 and 3 in Figure 6.5. The patch static capacitor is ignored because it has low impedance at the frequencies used in this experiment (6 GHz). The inductance due to higher order modes is also ignored because it also is low impedance at 6 GHz.

To allow for the time delay *t* due to cabling it is assumed that

$$S_{in} = \frac{Z_{in} - R_o}{Z_{in} + R_o} e^{-j\omega t} \qquad 8.2$$

The parameters t, $R_1, Q_1, \omega_1, R_2, Q_2, \omega_2$ are adjusted to get the best fit of this S_{11} to the experimental results. All parameters can be estimated fairly well from the raw data, so the starting point for this fit is close to the final value for example:

Parameter	Initial estimate from S11	Best fit
t	0.121 ns	0.117 ns
f_1	5.860 GHz	5.853 GHz
Q_1	60.0	57.1
R_1	1.00 R_o	1.11 R_o
f_2	6.540 GHz	6.551 GHz
Q_2	60.0	46.4
R_2	1.00 R_0	1.24 R_0

Table 8-1 Parameter values used for the data fit

where *t* is in nanoseconds (ns) and R_o is the characteristic impedance which is 50 Ω.

Once the data fit matches with the experimental S_{nn} the final time delay obtained from the fit can be used to remove the time delay from the experimental results using the Equation 7.1 and actual Z_{in} can be found from this. Figure 8.1 (a) shows S_{11} in polar plot for the measured S_{11}(red), fitted curve for S_{11}(black) and the actual S_{11} (blue) after removing the time delay. Figure 8.1 (b) shows the input impedance Z_{11} in polar plot, Figure 8.1 (c)-(d) are for S_{22} and Z_{22} respectively. The figure clearly shows that the experimental results and the data fit obtained are almost identical.

The actual Z_{in} can be used to find the electric field modes at the transmitting antenna. From [84] the input impedance can be written as:

$$Z_{in} = \frac{V_{in}}{I_o}$$ 8.3

where V_{in} is the voltage at the feed point and I_o is the current.
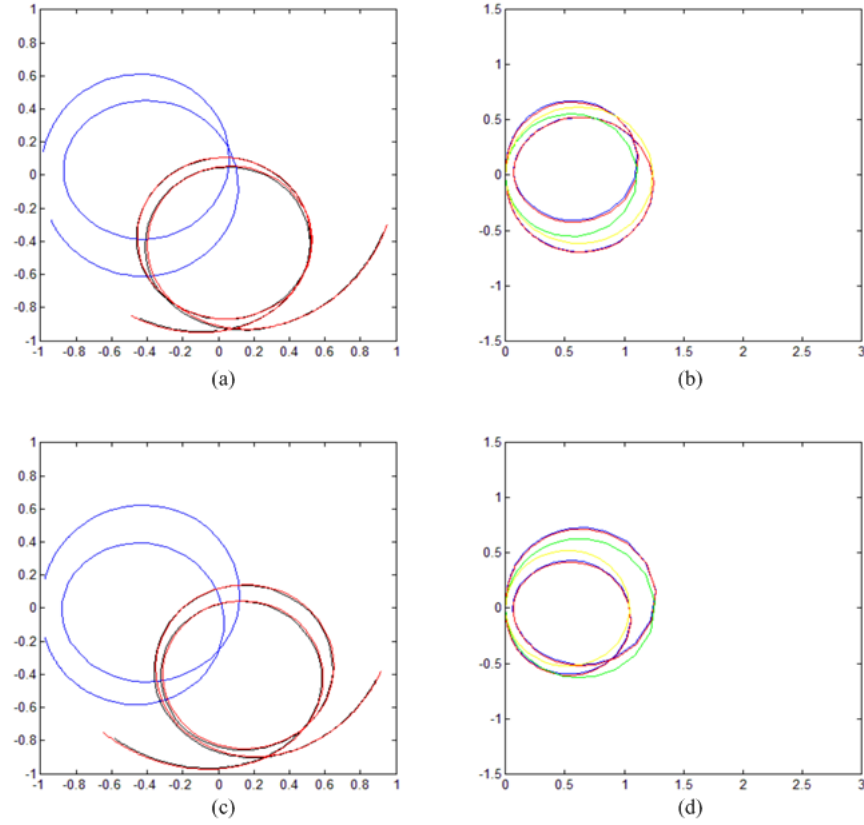
Figure 8-1 The polar plot for reflection coefficient and input impedance for actual fit, experiment and data fit for: (a) S11 (b) Z11 (c) S22 (d) Z22

The Equation 2.22 can be written as:

$$E_z(x,y) = \omega I_o Z_o k \sum_{m}^{\infty} \sum_{n}^{\infty} \frac{\psi_{mn}(x,y)\psi_{mn}(x_0,y_0)}{k^2 - k_{mn}^2} G_{mn} \qquad 8.4$$

where $Z_o = \sqrt{\mu/\epsilon}$ is the impedance of free space and $k = \omega\sqrt{\mu\epsilon}$ is the wave number.

Also the voltage at the feed point can be written as:

$$V_{in} = -hE_z(x_0,y_0) \qquad 8.5$$

where h is the height of the patch substrate.

Substituting equation (8.5) and (8.4) in Equation 8.3, electric field (E-field) for the two modes can be obtained from Z_{in}. Figure 8.2 shows the E-field modes for the two modes. Figure 8.2 (a) is for antenna element *T1* (refer Figure 5.1) and Figure 8.2 (b) is for antenna element *T2* (refer Figure 5.1).

101
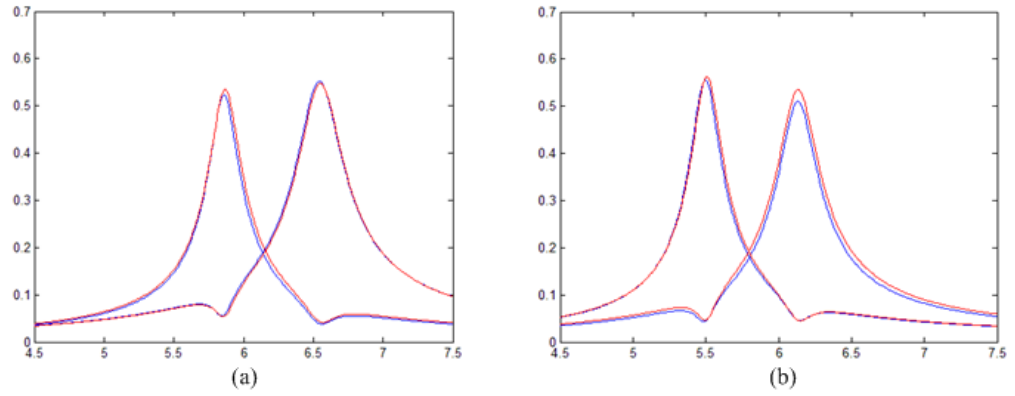
Figure 8-2 E-field for antenna elements at the transmitting antennas. X-axis shows magnitude and Y-axis shows frequency in GHz (a) Antenna element T1 (b) Antenna element T2

From the two E-field modes the fringing E-field at all four edges of a patch antenna element can be found. The radiation from a patch antenna element for two modes are found using the method in [24], the same equations are mentioned in Equation 2.5.1. The assumption of how the E-fields travel from the transmitter to the reflecting body (metal) to receiver is shown in Figure 8.3. It is assumed that the reflecting object and the antenna array are perfectly parallel to each other. It is also assumed that the reflection coefficient of the reflecting body as -1, being a metal. At the receiver the assumption was made that the received signals are received at the centre of each edge. Black arrows in the figure are for *mode 1* E-field and blue arrows are for *mode 2* E-fields.
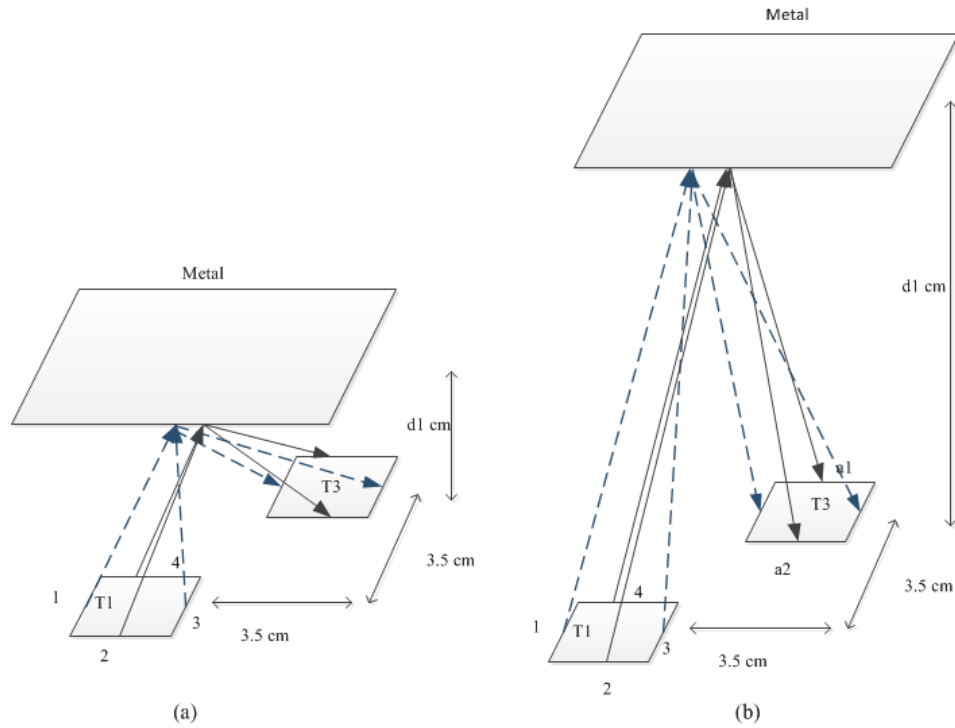
Figure 8-3 Transmission and reception of signals at antenna element T1 and T2 (a) Short distances for d1 (b) Long distances for d1

The methods used in this section can be worked backwards at the receiver to calculate the E-field received at the receiver terminal of network analyser. The received signals at the receiver antenna at all the edges can be used to find the signal inside the receiver substrate and the E-fields at all the four edges are combined at the feed point to obtain the E-field at the receiving terminal. From this E-field the S-parameter S_{31} can be calculated. Figure 8.4 shows the polar plots of the transmission coefficients from one patch to another, for reflection measurements by metal at distances of 1 cm – 12 cm, after having removed the coupling effect and the cable time delays. Figure 8.5 shows the polar plots for reflection back to the transmitter patch for the above conditions. The following figures below have a colour code of blue – red – green as the distance varies from 1 cm – 12 cm (In the plots below *theory* corresponds to values obtained by theoretical calculation and *experiment* corresponds to measured values evaluated from the experiment).
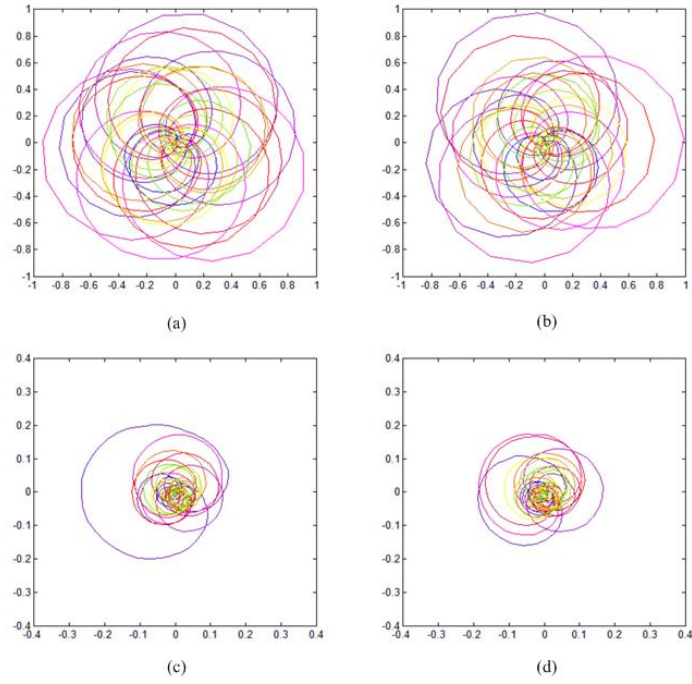
Figure 8-4 Polar plot of transmission coefficient (a) S13 theory (b) S24 theory (c) S13 experiment (d) S24 experiment
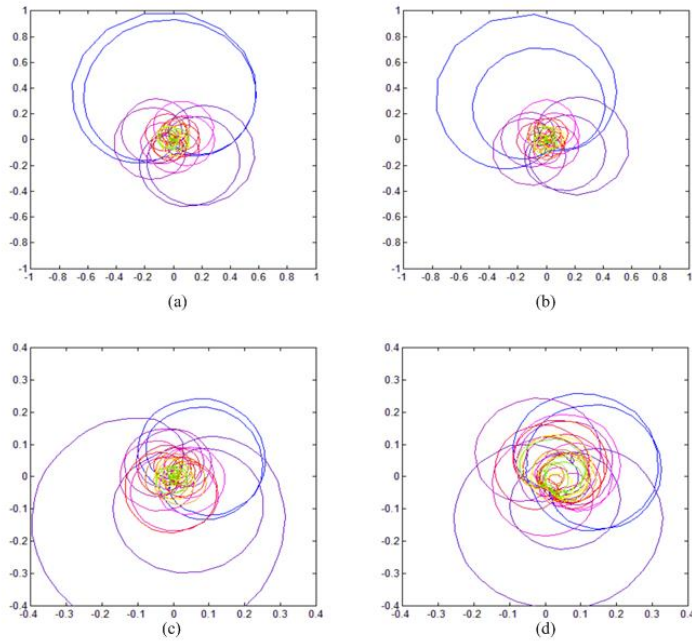
Figure 8-5 Polar plot of reflection back to the transmitter patch (a) Patch T1 theory (b) Patch T2 theory (c) Patch T1 experiment (d) Patch T2 experiment

[Note that the amplitudes of the theoretical plots have been normalised to a maximum value of 1.] The amplitude of S-parameters for metal reflection measurements are plotted for theoretical results (Figure 8.6) and actual measurements (Figure 8.7).
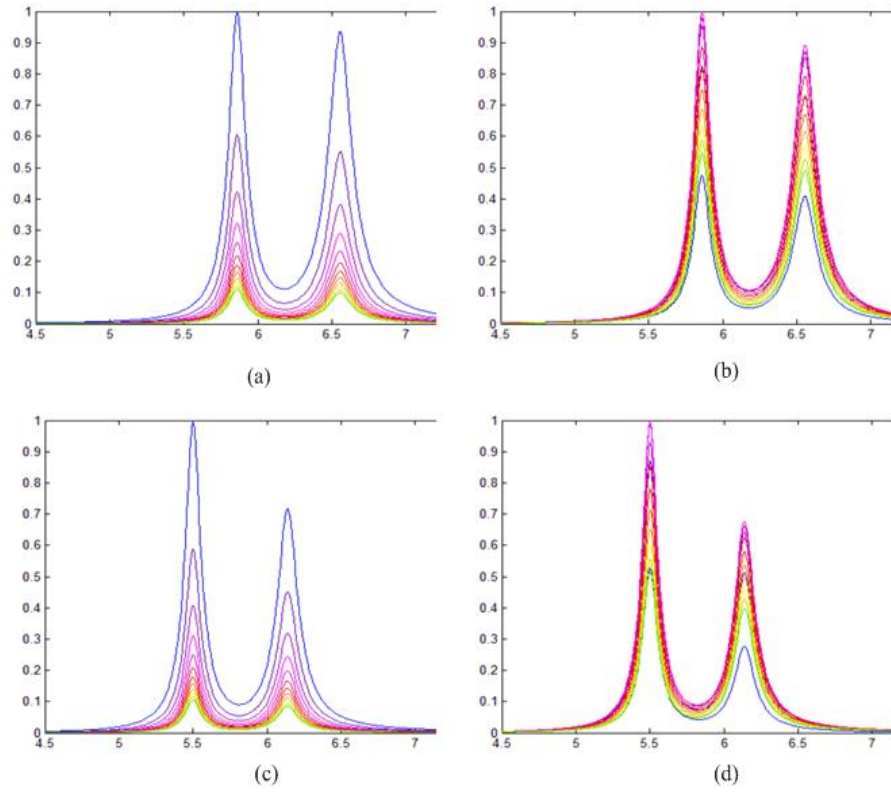
Figure 8-6 Amplitude of reflection back to the transmitter and receiver patch (Theory). X-axis corresponds to frequency in GHz and Y-axis corresponds to magnitude (a) Patch T1 (b) S13 (c) Patch T2 (d) S24
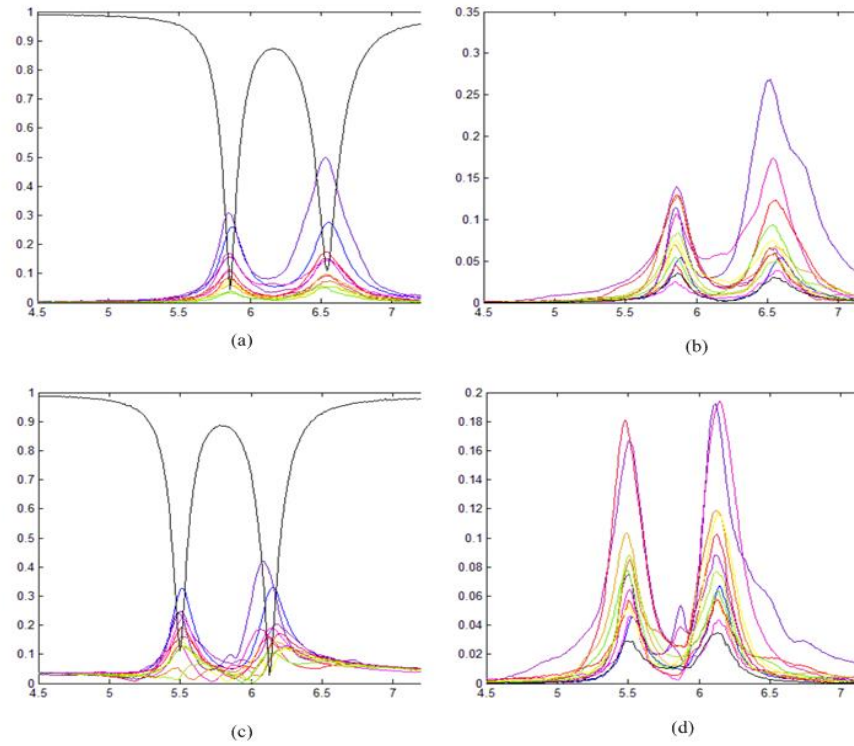
Figure 8-7 Amplitude of reflection back to the transmitter and receiver patch (Experiment). X-axis corresponds to frequency in GHz and Y-axis corresponds to magnitude (a) Patch T1 (b) S13 (c) Patch T2 (d) S24

Figure 8.7 (a) corresponds to amplitude of reflection back to antenna *T1* for reflection measurements by removing coupling (here black line in Figure 8.7 shows S_{11} and S_{22} with no metal reflection.) and Figure 8.7 (c) shows the same for antenna *T2*. Figure 8.7 (b) shows the reflection measurements after removing the coupling for transmission coefficients for *T1* to T3 and Figure 8.7 (d) corresponds to *T2* to *T4*.

Figure 8.8 shows the theoretical phase angle variation of reflection back to transmitter and receiver antennas for metal reflection measurements.
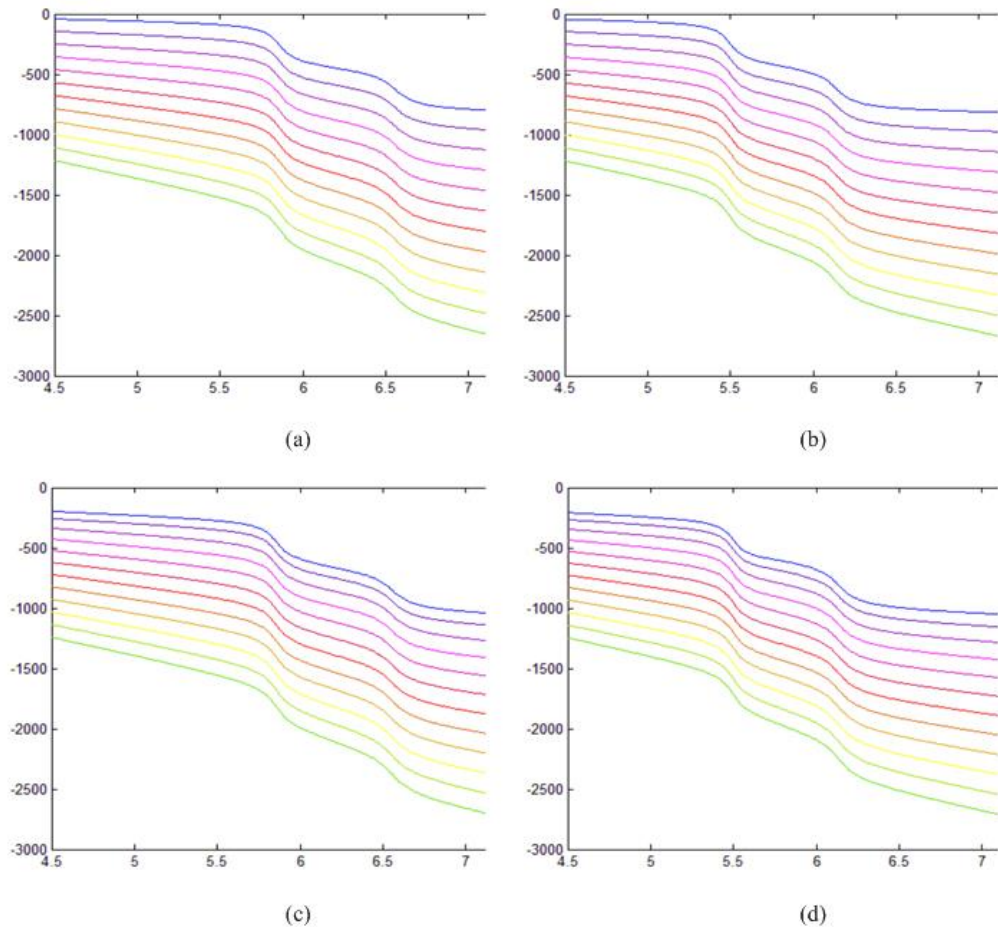
Figure 8-8 Phase angle variation for reflection measurements (Theory) 1 cm - 12 cm. X-axis shows frequency in GHz and Y-axis in degree (a) Patch T1 (b) Patch T2 (c) S13 (d) S24

The plots below are the phase plots for the experimental results which were obtained using the experimental methodology in this chapter. Figure 8.9 shows S-parameter phase angle variation for metal reflection measurements from experiments.
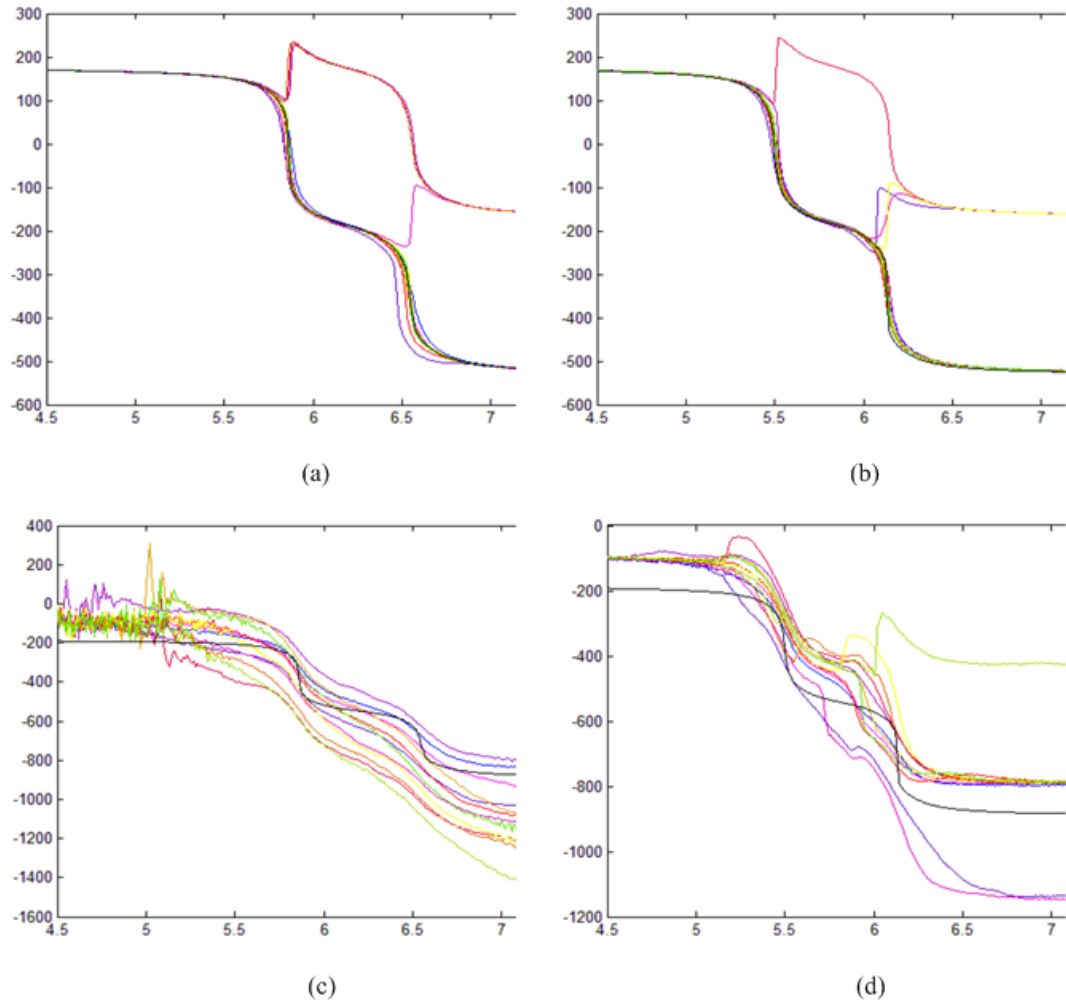
Figure 8-9 Phase angle plot for metal reflection measurements (Experiment). X-axis in GHz and Y-axis in degree (a) S11 (b) S22 (c) Patch T1 (coupling removed) (d) Patch T2 (coupling removed)

In Figure 8.10 the phase angle variations for transmission coefficient are shown.
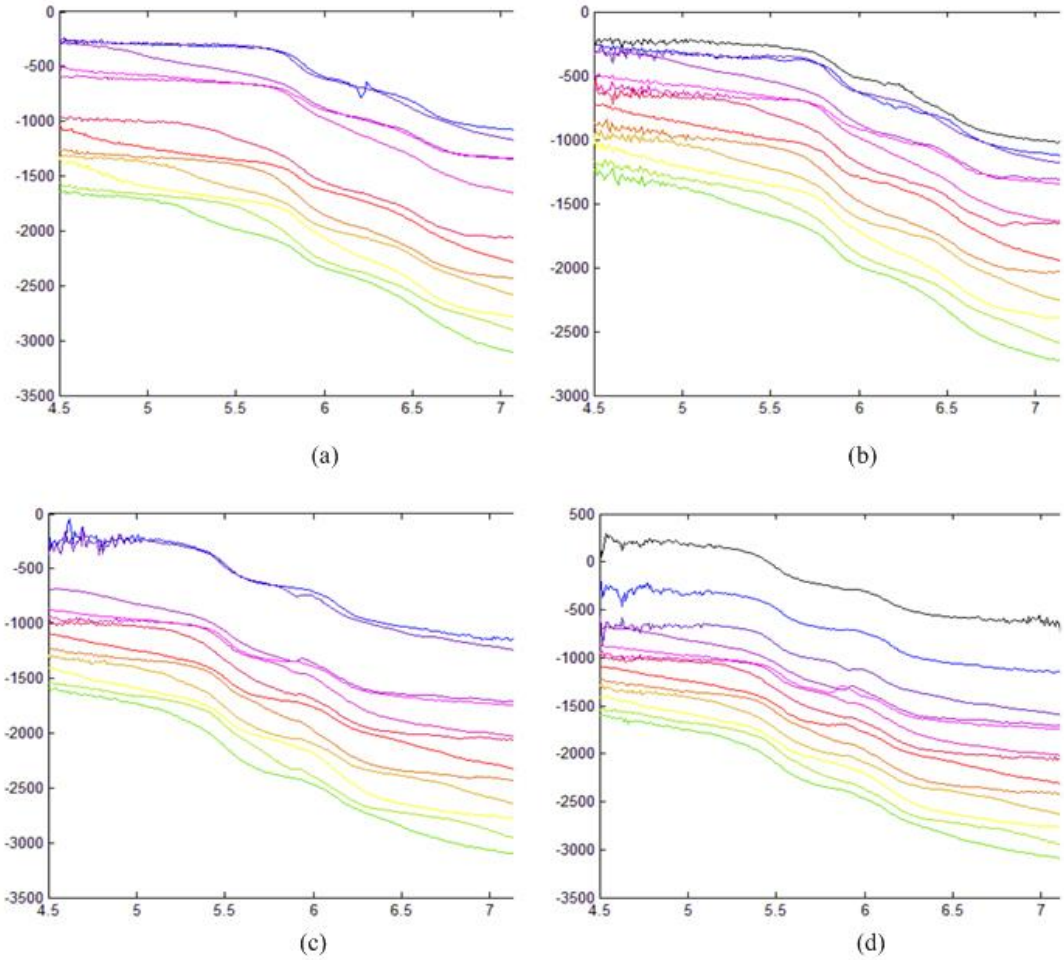
Figure 8-10 Phase plot of transmission coefficient (Experiment). X-axis in GHz and Y-axis in degree (a) S13 (b) S13 (coupling removed) (c) S24 (d) S24 (coupling removed)

Plots in Figure 8.9 and 8.10 show that the phase angle variation from the reflection measurements can be separated. Looking at the Figure 8.9 (c) phase information of reflections back to the transmitting antennas T1 in the region of interest (5.5 GHz – 6.5 GHz), the phase angle line differ with respect to distance more consistently than for *T2* in Figure 8.9 (d) whereas in Figure 8.10 (c-d) for distances close to the antenna the phase information can hardly be retrieved. For distances above 4 cm it can be separated well even though the plots differ from the ideal plots as shown in Figure 6.9 and Figure 6.10.

In Chapter 7 the plots for phase analysis of experiments were shown (Figure 7.6). The phase graph shown in Figure 7.6 was obtained by a very approximate method. The

assumption made was that the phase angle of the signal starts at -180° at 3 GHz and is a constant straight line till the resonance and at each resonance frequency the phase angle undergoes a 360° phase jump. Based on this assumption a time delay for the cable was estimated and subtracted from the measurements. The phase angle correction of 360° for reflection measurements was manually entered. But in this chapter a more accurate methodology has been developed to calculate the corrected parameters which can then be used to obtain true S-parameter measurements.

8.2 Summary

The theoretical model was successfully developed in this chapter. This chapter also describes how the experimental data was fitted, based on the resonance frequency model. The data fitting was almost identical with the experimental results and this chapter also shows how to compensate for time delays that may occur in measurements. The next chapter describes conclusions and future work that can be applied to improve this research.

Chapter 9 Conclusion and Future Work

The objective of the research was to find how effectively signals from the dual-band antenna array are capable of maintaining the phase relation in the measurements. This research helps to identify and improve the design and gives greater insight into phase analysis of reflection measurements. The antenna array designed using HFSS software was experimentally verified and the design fitted well with the experimental results for the antenna characteristics. Theory has been developed to analyse the experimental results and a data fit has been made to the experimental results. This led to the finding of actual S-parameter values which can then be used to find received signal at the receiver antenna. The phase information extracted from the receiver antenna could be used to estimate distance to the reflecting body.

One finding from the phase information is that the distance of the object with respect to antenna array is an important factor. For distances close to antenna, the phase information of the received signals were distorted and it was found that distances above 4cm had good phase angle characteristics, but as the distance increases (beyond 10 cm) the signal strength reduces. The ideal phase angle relation with respect to distance is expected to be a straight line but the results shows that these phase angles are not a straight line. In some cases the angles have sudden phase jumps which tend to overlap with the measurements at other distances. Another reason for not getting a proper phase angle is because of the measurement setup which can cause errors in the results.

This research needs further work to fully establish the reflection coefficient of the object based on the phase information. One way to increase the information from the body is to increase the number of antennas in an array.

One drawback associated with the measurement setup was that the antenna array and the reflecting body were not perfectly parallel to each other, the reason being too much

cable stress at the antenna element terminal made the array to bend along one edge. This may also contribute to the phase jump errors (the S-parameter curve not going around the origin in a polar plot).

The theory for analysis assumed that the signals were constant along each edge of the receiving antenna, equal to the value at the centre of the edge. Improvement in the theory may be achieved by increasing the number receiving points along each edge.

For this research the reflecting object used was metal, but objects with other reflection properties could also be tested.

This research developed a methodology which can use the raw experimental results to calculate the signals received at the receiver. This research has also identified areas that need careful consideration for future work.

References

[1]   J. Kim and Y. Rahmat-Samii, "Implanted Antennas Inside a Human Body: Simulations, Designs, and Characterizations," *IEEE TRANSACTIONS ON MICROWAVE THEORY AND TECHNIQUES,* vol. 52, pp. 1934-1943, AUGUST 2004.

[2]   A. C. Patel, M. P. Vaghela, H. Bajwa, and H. Seddik, "Conformable patch antenna design for remote health monitoring," presented at the 2010 Long Island Systems Applications and Technology Conference (LISAT), Farmingdale, NY, May 2010.

[3]   M. L. Scarpello, D. Kurup, H. Rogier, D. V. Ginste, F. Axisa, J. Vanfleteren, W. Joseph, and L. Martens, "Design of an Implantable Slot Dipole Conformal Flexible Antenna for Biomedical Applications," *IEEE TRANSACTIONS ON ANTENNAS AND PROPAGATION,* vol. 59, pp. 3556-3564, OCTOBER 2011.

[4]   H. n.-L. p. M. A, Q. n.-G. l. M, G. l. G. a. S, R. B. A, and G. m. M. n. R, "A rotating array of antennas for confocal microwave breast imaging," *Microwave and Optical Technology Letters,* vol. 39, pp. 307 - 311, 2003.

[5]   S. Kubota, X. Xiao, N. Sasaki, K. Kimoto, W. Moriyama, and T. Kikkawa, "Experimental confocal imaging for breast cancer detection using silicon on-chip UWB microantenna array," in *IEEE Antennas and Propagation Society International Symposium*, San Diego, CA July 2008 pp. 1 - 4

[6]   M. Klemm, I. J. Craddock, J. A. Leendertz, A. Preece, and R. Benjamin, " Radar-Based Breast Cancer Detection Using a Hemispherical Antenna Array—Experimental Results " *IEEE Transactions on Antennas and Propagation,* vol. 57, pp. 1692 - 1704 2009.

[7]   N.H.Farhat, "Microwave Holography and its Applications in Modern Aviation," in *Engineering Applications of Holography Symposium, Proceedings of SPIE*, 1962, pp. 295–314.

[8]   M. Elsdon, M. Leach, M. J. FDO, S. J. Foti, and D. Smith, "Early Stage Breast Cancer Detection using Indirect Microwave Holography " presented at the 36th European Microwave Conference, Manchester 2006.

[9]   D. Smith and S. Braun, " The detection of concealed objects using microwave indirect holographic imaging (MIHI) techniques " in *IEEE Antennas and Propagation Society International Symposium*, Columbus, OH, USA June 2003 pp. 167 - 170.

[10]   D. Smith, M. Elsdon, M. Leach, M. Fernando, and S. J. Foti, " 3D Microwave Imaging for Medical and Security Applications " presented at the RF and Microwave Conference, Putra Jaya Sept. 2006

[11]   D. Smith, M. Leach, M. Elsdon, and S. J. Foti. (Feb. 2007) Indirect Holographic Techniques for Determining Antenna Radiation Characteristics and Imaging Aperture Fields *IEEE Antennas and Propagation Magazine*. 54-67.

[12]   M. Klemm, J. A. Leendertz, D. Gibbins, I. J. Craddock, A. Preece, and R. Benjamin, "Microwave Radar-Based Differential Breast Cancer Imaging: Imaging in Homogeneous Breast Phantoms and Low Contrast Scenarios " *IEEE Transactions on Antennas and Propagation,* vol. 58, pp. 2337 - 2344 2010.

[13]   K. D. Paulsen, P. M. Meaney, and S. P. Poplack, "Imaging the Breast with Microwaves: The Dartmouth Experience," in *USRI proceedings*, 2008.

[14]   J. Q. Howell, "Microstrip antennas " *IEEE Transactions on Antennas and Propagation,* vol. 23 pp. 90-93, 1975.

[15]   M. R. E, "Conformal microstrip antennas and microstrip phased arrays " *IEEE Transactions on Antennas and Propagation,* vol. 22, pp. 74 - 78 1974.

[16]   J.-Y. Sze and K.-L. Wong, "Bandwidth enhancement of a microstrip-line-fed printed wide-slot antenna " *IEEE Transactions on Antennas and Propagation,* vol. 49, pp. 1020 - 1024, Jul 2001.

[17]   P. B. Katehi, N. Alexopoulos, and I. Y. Hsia, "A bandwidth enhancement method for microstrip antennas " *IEEE Transactions on Antennas and Propagation,* vol. 35, pp. 5 - 12 Jan 1987.

[18]   J.-Y. Sze and K.-L. Wong, "Slotted rectangular microstrip antenna for bandwidth enhancement " *IEEE Transactions on Antennas and Propagation,* vol. 48, pp. 1149 - 1152 Aug 2000

[19]   Y. T. Lo, D. Solomon, and W. Richards, "Theory and experiment on microstrip antennas," *IEEE Transactions on Antennas and Propagation,* vol. 27, pp. 137 - 145 Mar 1979

[20]   W. F. Richards, Y. T. Lo, and D. D. Harrison, "An improved theory for microstrip antennas and applications," *IEEE Transactions on Antennas and Propagation,* vol. 29, pp. 38 - 46 Jan 1981

[21]   Y. T. Lo and W. F. Richards, "Perturbation approach to design of circularly polarised microstrip antennas " *Electronics Letters,* vol. 17, pp. 383 - 385 May 1981

[22]   R. Garg, P. Bhartia, I. Bhal, and A. Ittipiboon, *Microstrip antenna design hand book* Boston: Arctech House 2001.

[23]   C. A. Balanis, *Antenna theory* Third ed. New Jersey: John Wiley & Sons, 2005.

[24]   S. J. Orfanidis. (2002). *Electromagnetic Waves and Antennas*. Available: http://eceweb1.rutgers.edu/~orfanidi/ewa/

[25]   R. F. Harrington, *Time-Harmonic Electromagnetic Fields*: Wiley-IEEE Press, August 2001.

[26]   D. Thouroude, M. Himdi, and J. P. Daniel, "CAD-oriented cavity model for rectangular patches " *Electronics Letters,* vol. 26, pp. 842-844, Jun 1990.

[27]   S. A. Long, L. C. Shen, M. D. Walton, and M. R. Allerding, "Impedance of a circular-disc printed-circuit antenna " *Electronics Letters,* vol. 14, pp. 684-686, 1978.

[28]   K.-F. Lee, K.-M. Luk, and J. S. Dahele, "Characteristics of the equilateral triangular patch antenna " *IEEE Transactions on Antennas and Propagation,* vol. 36, pp. 1510-1518, Nov 1988.

[29]   Z. N. Chen and K.-M. Luk, *Antennas for Base Stations in Wireless Communications*: The McGraw-Hill Companies, 2009.

[30]   D. G. Fang, *Antenna Theory and Microstrip Antennas*: CRC Press, 2010.

[31]   D. M. Pozar, *Microwave Engineering*, 3rd ed.: John Wiley & Sons, 2005.

[32]   J.-S. Chen and K.-L. Wong, "A single-layer dual-frequency rectangular microstrip patch antenna using a single probe feed," *Microwave and Optical Technology Letters,* vol. 11, Dec. 1998.

[33]   S. Maci and G. B. Gentili. (Dec 1997) Dual-frequency patch antennas *IEEEAntennas and Propagation Magazine*. 13 - 20

[34]   M. A. Al-Joumayly, S. M. Aguilar, N. Behdad, and S. C. Hagness, " Dual-Band Miniaturized Patch Antennas for Microwave Breast Imaging " *IEEE Antennas and Wireless Propagation Letters,* vol. 9, pp. 268 - 271 2010

[35]   M. N. Hasan, S. W. Shah, M. I. Babar, and Z. Sabir, " Design and simulation based studies of a dual band u-slot patch antenna for WLAN application " presented at the International Conference on Advanced Communication Technology (ICACT), PyeongChang Feb. 2012

[36]   H.-n. Wang and F.-C. Chen, "Dual-band patch antenna with electromagnetic bandgap structure " in *Asia-Pacific Microwave Conference Proceedings (APMC)*, Yokohama Dec. 2010 pp. 2009 - 2012

[37]   N. Misran, M. T. Islam, N. M. Yusob, and A. T. Mobashsher, " Design of a compact dual band microstrip antenna for Ku-band application " presented at the International Conference on Electrical Engineering and Informatics, Selangor Aug. 2009

[38]   E. O. Hammerstad, "Equations for Microstrip Circuit Design," in *5th European Microwave Conference* Hamburg, Germany, Sept. 1975, pp. 268 - 272.

[39]   K. F. Lee and W. Chen, *Advances in Microstrip and Printed Antennas*. New York: John Wiley & sons, June 1997.

[40] J. L. Volakis, *Antenna Engineering Handbook,*, Fourth ed.: McGraw-Hill Companies, 2007.

[41] P. T. Huynh, A. M. Jarolimek, and S. Daye, "The false-negative mammogram," *RadioGraphics,* vol. 18, pp. 1137-1154, 1998.

[42] J. G. Elmore, M. B. Barton, V. M. Moceri, S. Polk, P. J. Arena, and S. W. Fletcher, "Ten-Year Risk of False Positive Screening Mammograms and Clinical Breast Examinations," *The New England Journal of Medicine,* vol. 338, pp. 1089-1096, Apr 1998.

[43] E. C. Fear, S. C. Hagness, P. M. Meaney, M. Okoniewski, and M. A. Stuchly. (2001) Enhancing breast tumor detection with near-field imaging *IEEE Microwave Magazine*. 48 - 56

[44] P. M. Meaney, M. W. Fanning, D. Li, S. P. Poplack, and K. D. Paulsen, "A clinical prototype for active microwave imaging of the breast," *IEEE Transactions on Microwave Theory and Techniques,* vol. 48, pp. 1841 - 1853 2000.

[45] E. C. Fear, X. Li, S. C. Hagness, and M. A. Stuchly, " Confocal microwave imaging for breast cancer detection: localization of tumors in three dimensions " *IEEE Transactions on Biomedical Engineering,* vol. 49, pp. 812 - 822, 2002.

[46] E. C. Fear and M. Okoniewski, " Confocal microwave imaging for breast tumor detection: application to a hemispherical breast model " in *IEEE MTT-S International Microwave Symposium Digest*, Washington, 2002, pp. 1759 - 1762.

[47] S. C. Hagness, A. Taflove, and J. E. Bridges, "Three-dimensional FDTD analysis of a pulsed microwave confocal system for breast cancer detection: design of an antenna-array element " *IEEE Transactions on Antennas and Propagation,* vol. 47, pp. 783 - 791 May 1999

[48] E. Fear, A. Low, J. Sill, and M. A. Stuchly, " Microwave system for breast tumor detection: experimental concept evaluation " presented at the IEEE Antennas and Propagation Society International Symposium, 2002.

[49] E. C. Fear, J. Sill, and M. A. Stuchly, " Experimental feasibility study of confocal microwave imaging for breast tumor detection " *IEEE Transactions on Microwave Theory and Techniques,* vol. 51, pp. 887 - 892 2003.

[50] J. M. Sill and E. C. Fear, " Tissue sensing adaptive radar for breast cancer detection - experimental investigation of simple tumor models " *IEEE Transactions on Microwave Theory and Techniques,* vol. 53, pp. 3312 - 3319 2005.

[51] M. Miyakawa, N. Iwata, N. Ishii, and M. Bertero, " Low reflection sandwiched dipole array antenna used in high-loss liquids " in *European Microwave Conference*, Munich 2007, pp. 317 - 320

[52] S. Salvador and G. Vecchi, " On some experiments with UWB microwave imaging for breast cancer detection " in *IEEE Antennas and Propagation Society International Symposium*, Hawaii, 2007, pp. 253 - 256

[53] D. Gibbins, M. Klemm, I. J. Craddock, J. A. Leendertz, A. Preece, and R. Benjamin, "A Comparison of a Wide-Slot and a Stacked Patch Antenna for the Purpose of Breast Cancer Detection " *IEEE Transactions on Antennas and Propagation,* vol. 58, pp. 665 - 674 2010.

[54] D. GABOR, "A New Microscopic Principle," *Nature,* vol. 161, May 1948.

[55] E.N.Leith and J.Upatnieks, "Reconstructed wavefronts and communication theory," *Journal of the Optical Society of America,* vol. 52, pp. 1123-1128, Oct 1962.

[56] G. Tricoles and N. H. Farhat, "Microwave holography: Applications and techniques " in *IEEE Proceedings*, Jan. 1977 pp. 108 - 121.

[57] B. Hildebrand and K. Haines, "Holography by Scanning," *Journal of the Optical Society of America,* vol. 59, pp. 1-6, 1969.

[58] D. M. Sheen, D. L. McMakin, and T. E. Hall, " Three-dimensional millimeter-wave imaging for concealed weapon detection " *IEEE Transactions on Microwave Theory and Techniques,* vol. 49, pp. 1581 - 1592 Sep 2001

[59] R. K. Amineh, M. Ravan, A. Khalatpour, and N. K. Nikolova, "Three-Dimensional Near-Field Microwave Holography Using Reflected and Transmitted Signals " *IEEE Transactions on Antennas and Propagation,* vol. 50, pp. 4777 - 4789, Dec. 2011

[60] A. A. Eldek, A. Z. Elsherbeni, and C. E. Smith. (Dec. 2004) Microstrip-fed printed lotus antenna for wideband wireless communication systems *IEEE Antennas and Propagation Magazine*. 164 - 173.

[61] D. D. Krishna, M. Gopikrishna, C. K. Aanandan, P. Mohanan, and K. Vasudevan, " Compact dual-polarised square microstrip antenna with triangular slots for wireless communication " *Electronics Letters* vol. 42, pp. 894 – 895 Aug. 2006.

[62] S. K. Rajgopal and S. K. Sharma, " Investigations on Ultrawideband Pentagon Shape Microstrip Slot Antenna for Wireless Communications " *IEEE Transactions on Antennas and Propagation,* vol. 57, pp. 1353 - 1359 May 2009

[63] A. N. Kulkarni and S. K. Sharma, "Frequency Reconfigurable Microstrip Loop Antenna Covering LTE Bands With MIMO Implementation and Wideband Microstrip Slot Antenna all for Portable Wireless DTV Media Player " *IEEE Transactions on Antennas and Propagation,* vol. 61, pp. 964 - 968 Feb. 2013

[64] T. N. Thi, K. C. Hwang, and H. B. Kim, " Dual-band circularly-polarised Spidron fractal microstrip patch antenna for Ku-band satellite communication applications " *Electronics Letters* vol. 49, pp. 444-445, March 2013

[65] Y.-B. Jung, S.-Y. Eom, and S.-I. Jeon, "Experimental Design of Mobile Satellite Antenna System for Commercial Use " *IEEE Transactions on Consumer Electronics,,* vol. 56, pp. 429-435, May 2010

[66] A. J. Lozada and S. Donglin, " Microstrip antenna for satellite communications " presented at the International Symposium on Antennas Propagation and EM Theory, Kunming Nov. 2008

[67] R. K. Kanth, A. K. Singhal, P. Liljeberg, and H. Tenhunen, " Analysis, design and development of novel, low profile microstrip antenna for satellite navigation " presented at the NORCHIP, Trondheim Nov. 2009

[68] A. Dadgarpour, A. Abbosh, and F. Jolani, " Planar Multiband Antenna for Compact Mobile Transceivers " *IEEE Antennas and Wireless Propagation Letters,* vol. 10, 2011.

[69] M. Yang and Y. Chen, " A novel U-shaped planar microstrip antenna for dual-frequency mobile telephone communications " *IEEE Transactions on Antennas and Propagation,* vol. 49, pp. 1002 - 1004 Jun 2001

[70] F. Bilotti and C. Vegni, " Design of High-Performing Microstrip Receiving GPS Antennas With Multiple Feeds " *IEEE Antennas and Wireless Propagation Letters,* vol. 9, pp. 248 - 251 2010.

[71] S.-Y. Lin and K.-C. Huang, "A compact microstrip antenna for GPS and DCS application " *IEEE Transactions on Antennas and Propagation,* vol. 53, pp. 1227 - 1229 March 2005

[72] H.-M. Chen, Y.-K. Wang, Y.-F. Lin, C.-Y. Lin, and S.-C. Pan, " Microstrip-Fed Circularly Polarized Square-Ring Patch Antenna for GPS Applications " *IEEE Transactions on Antennas and Propagation,* vol. 57, pp. 1264 - 1267 April 2009

[73] M. Abbak and I. Tekin, "RFID Coverage Extension Using Microstrip-Patch Antenna Array [Wireless Corner] " *IEEE Antennas and Propagation Magazine,* vol. 51, pp. 185 - 191 Feb. 2009

[74] H.-W. Liu, C.-H. Weng, and C.-F. Yang, " Design of Near-Field Edge-Shorted Slot Microstrip Antenna for RFID Handheld Reader Applications " *IEEE Antennas and Wireless Propagation Letters,* vol. 10 pp. 1135 - 1138 2011

[75] Z.-J. Tang and Y.-G. He, " Broadband microstrip antenna with U and T slots for 2.45/2.41 GHz RFID tag " *Electronics Letters* vol. 45, pp. 926 - 928 Aug. 2009

[76] H.-W. Liu, C.-F. Yang, and C.-H. Ku, " Novel Miniature Monopole Tag Antenna for UHF RFID Applications " *IEEE Antennas and Wireless Propagation Letters,* vol. 9, pp. 363 - 366 2010.

[77] H.-D. Chen, C. Sim, and S.-H. Kuo, "Compact Broadband Dual Coupling-Feed Circularly Polarized RFID Microstrip Tag Antenna Mountable on Metallic Surface " *IEEE Transactions on Antennas and Propagation,* vol. 60, pp. 5571 - 5577 Dec. 2012

[78] RogersCorporation. *RO4000® Series*. Available: http://www.rogerscorp.com/documents/726/acm/RO4000-Laminates---Data-sheet.pdf

[79] MATLAB. *http://www.mathworks.com/products/matlab/*

[80] K. T. (Agilent). *N5230A PNA-L Network Analyzer, 4-ports, up to 13.5, 20 GHz*. Available: http://www.keysight.com/en/pd-415192/4-port-pna-l-series?&cc=NZ&lc=eng

[81] ANSYS. *ANSYS HFSS*. Available: http://www.ansys.com/Products/Simulation+Technology/Electronics/Signal+Integrity/ANSYS+HFSS

[82] R. Bancroft, *Microstrip and Printed Antenna Design*, Second ed.: SciTech Publishing, 2008.

[83] WellshowTechnology. *RG402(0.141") Semi-rigid Coaxial Cable*. Available: http://www.wellshow.com/coax-cables/semi-rigid-cable/rg40-semi-rigid-coaxial-cable-2/

[84] K. R. Carver and J. W. Mink, "Microstrip antenna technology " *IEEE Transactions on Antennas and Propagation* vol. 29, pp. 2-24, Jan 1981.